Exploration of Cosserat Elastic Structures with Novel Characteristics via Experimental Micromechanics

By

Zachariah D. Rueger

A dissertation submitted in partial fulfillment of
the requirements for the degree of

Doctor of Philosophy
(Materials Science)

at the
UNIVERSITY OF WISCONSIN - MADISON
2018

Date of final oral examination: 05/09/2018

The dissertation is approved by the following members of the Final Oral Committee:
Roderic S. Lakes, Professor, Materials Science and Engineering
Susan Babcock, Professor, Materials Science and Engineering
Donald Stone, Professor, Materials Science and Engineering
Xudong Wang, Professor, Materials Science and Engineering
Melih Eriten, Assistant Professor, Mechanical Engineering

Abstract

The currently accepted classical theory of elasticity is limited when describing many materials by its two elastic constants. Another theory of elasticity, the Cosserat theory, incorporates rotation of points and distributed moments (couple stresses) in addition to the translation of points and force stress present in classical elasticity. Consequently, the Cosserat theory has more freedom and offers a richer framework to describe materials than the classical theory - it contains six elastic constants. Understanding materials by the more descriptive capabilities of the Cosserat theory will facilitate a novel approach to material design - optimization of the six Cosserat elastic constants. Additionally, Cosserat elasticity predicts several key phenomena to differ from classical predictions. One such phenomenon is the Cosserat prediction of a size effect in the torsion and bending of circular cylinders of Cosserat elastic materials - specimens are more rigid than expected classically.

In this document, a variety of materials are systematically analyzed using the framework of Cosserat elasticity via experimentation. The size effects demonstrated by the following materials are explored, the Cosserat elastic constants extracted, and the mechanisms by which deformation is controlled are probed and related to Cosserat phenomena. First, open cell polyurethane foams of two cell sizes are explored as Cosserat continua. Next, specimens of the large cell foam, triaxially compressed under heat to achieve a negative Poisson's ratio, are studied. Unidirectional composites composed of corrugated nylon tubing segments and silicone rubber cement are engineered and demonstrate extremely large size effects in torsion. Approximate solutions for bending and torsion of Cosserat elastic materials with square cross sections are used to probe Cosserat behavior of designed negative Poisson's ratio tetragonal lattices. Conclusions drawn from studies up to this point are employed to engineer triangular prismatic unit cell lattices demonstrating Cosserat elastic effects including large magnitude size effects in torsion and bending. The lattices made of

triangular prismatic unit cells incorporating strain gradient sensitive rib elements are engineered and experimentally analyzed as Cosserat material. Finally, the systematic design and experimentation process leading to the development of triangular prismatic unit cell lattices demonstrating large size effects is covered in detail.

Contents

Abstract **i**

Contents **iii**

List of Figures **vi**

List of Abbreviations **x**

1 Introduction **1**
1.1 Background Information . . . 1
1.1.1 Theories of Elasticity . . . 1
1.1.2 Cosserat Elasticity . . . 2
1.2 Motivation . . . 5
1.3 Thesis Organization . . . 7

2 Experimental Cosserat elasticity in open cell polymer foam **9**
2.1 Introduction . . . 9
2.2 Methods . . . 13
2.2.1 Materials and experiment . . . 13
2.2.2 Analysis and interpretation . . . 17
2.3 Results and discussion . . . 19
2.3.1 Size effects and elastic constants . . . 19
2.3.2 Viscoelastic damping . . . 26
2.3.3 Comparison with homogenization . . . 28
2.3.4 Comparison with other experiment . . . 28
2.3.5 Asymmetry of the stress . . . 29
2.3.6 Generalized continuum theories . . . 30
2.4 Conclusions . . . 32
2.5 Acknowledgements . . . 32

3 Cosserat elasticity of negative Poisson's ratio foam: experiment **33**
3.1 Introduction . . . 33
3.2 Methods . . . 39
3.2.1 Materials and experiment . . . 39

3.2.2 Analysis and interpretation . . . 42
3.3 Results and discussion . . . 44
3.4 Conclusions . . . 48
3.5 Acknowledgements . . . 49

4 Strong Cosserat elastic effects in a unidirectional composite 50
4.1 Introduction . . . 50
4.2 Methods . . . 55
4.2.1 Materials and experiment . . . 55
4.2.2 Analysis and interpretation . . . 58
4.3 Results and discussion . . . 59
4.4 Conclusions . . . 63
4.5 Acknowledgements . . . 63

5 Observation of Cosserat Elastic Effects in a Tetragonal Negative Poisson's Ratio Lattice 64
5.1 Introduction . . . 65
5.2 Methods . . . 69
5.2.1 Materials and experiment . . . 69
5.2.2 Analysis and interpretation . . . 71
5.3 Results and discussion . . . 73
5.4 Conclusions . . . 78
5.5 Acknowledgements . . . 78

6 Strong Cosserat elasticity in a transversely isotropic polymer lattice 79

7 Cosserat Elastic Lattices 92
7.1 Introduction . . . 92
7.2 Methods . . . 96
7.2.1 Materials and Experiment . . . 96
7.2.2 Analysis and Interpretation . . . 98
7.3 Results and Discussion . . . 100
7.3.1 3D Strengthened Diagonal Unit Cell Lattice Structures . . . 100
Structures with <111> Cell Axes Parallel to Longitudinal Axis . . . 101
Structures with <100> Cell Axes Parallel to Longitudinal Axis . . . 105
7.3.2 Triangular Prismatic Unit Cell Structures . . . 110
Long Rib Triangular Unit Cell Structures . . . 111
Short Rib Triangular Prismatic Unit Cell Structures . . . 116
7.4 Conclusions . . . 120

8 Conclusions and Future Work 122
8.1 Conclusions . . . 122
8.2 Future Work . . . 124

A Summary of Additive Manufacturing Techniques Used for Lattice Research and Unit Cell Development History **125**
A.1 Fused Deposition Modeling (FDM) . . . 125
A.1.1 Student Shop FDM . . . 126
Printing History . . . 126
A.2 Material Jetting (Polyjet) . . . 133
A.2.1 Midwest Prototyping . . . 133
Printing History . . . 134
A.3 Selective Laser Sintering (SLS) . . . 135
A.3.1 Midwest Prototyping . . . 135
Printing History . . . 136
A.4 Summary of Adaptions . . . 146

Bibliography **147**

List of Figures

2.1 Foam ribs with increment of force dF and increment of moment dM upon ribs. . . . 10
2.2 Open cell polyurethane foam samples. 15
2.3 Specimens created from 0.4 mm cell foam. 17
2.4 Size effects for foam with 1.2 mm cells in torsion. Top scale, diameter normalized to cell size. Open circles represent experimental results. 20
2.5 Size effects for foam with 1.2 mm cells in bending. Top scale, diameter normalized to cell size. Open circles represent experimental results. 21
2.6 Size effects for foam with 0.4 mm cells in torsion. Top scale, diameter normalized to cell size. Open circles represent experimental results. 23
2.7 Size effects for foam with 0.4 mm cells in bending. Top scale, diameter normalized to cell size. Open circles represent experimental results. 24
2.8 Young's Modulus of foam in compression; circles, foam with 1.2 mm cells; triangles, foam with 0.4 mm cells. 25
2.9 Viscoelastic tan δ vs. specimen size for foam with 1.2 mm cells. Solid symbols and dash line fit: bending. Open symbols and solid line fit: torsion. 27
2.10 Viscoelastic tan δ vs. specimen size for foam with 0.4 mm cells. Solid symbols and dash line fit: bending. Open symbols and solid line fit: torsion. 27
2.11 Corner of rectangular section bars, with notch marked in black ink. Left, twisted rubber; scale bar, 5 mm. Center, foam, 0.4 mm cells, not twisted. Right, foam, 0.4 mm cells, twisted. 30

3.1 Ribs of foam or lattice with increment of force dF and increment of moment dM. . . 36
3.2 A specimen of foam with attached stalk and magnet. White scale bar: 5mm. 40
3.3 Structure of negative Poisson's ratio foam. Reflected light micrograph. Scale bar: 1 mm. 42
3.4 Size effects for negative Poisson's ratio foam in torsion. Points are experimental. Curve is theoretical for G = 16 kPa, ℓ_t = 2.3 mm N = 0.78 and Ψ = 1.5. Classical elasticity predicts constant Ω = 1 independent of diameter. 44
3.5 Size effects for negative Poisson's ratio foam in bending. Points are experimental. Curve is theoretical for E = 25 kPa N = 0.78, ℓ_b = 3.9 mm, and $\beta/\gamma = 0.88$. Classical elasticity predicts constant Ω = 1 independent of diameter. 47

3.6 Viscoelastic tan δ vs. specimen size for negative Poisson's ratio foam. Open circles: bending. Solid circles: torsion. 48

4.1 Composite containing unidirectional tubular inclusions with increment of force *dF* and increment of moment *dM*. 52
4.2 Views of aligned corrugated tubing and silicone rubber matrix composite. 56
4.3 Size effects for corrugated tubing specimens in torsion. Points are experimental. Curve is theoretical for G = 890 kPa, ℓ_t = 17.3 mm N = 0.996 and Ψ = 1.5. Classical elasticity ($\ell_t = 0$) predicts constant Ω = 1 independent of diameter. 60
4.4 Size effects for corrugated tubing specimens in bending. Points are experimental. Curve is theoretical for β/γ = 0.995, N = 0.999, E = 14.2 MPa, and ℓ_b = 7.91 mm. Classical elasticity predicts constant $\Omega = 1$ independent of diameter. 61

5.1 2x2 tetragonal lattice structure (left). Scale bar, 1 cm. End view (right). 69
5.2 Diagram (left) showing dimensions adapted from [89]. Slot (right) in present specimens. 69
5.3 Size effects for lattice specimens in torsion. Points are experimental. Curve is theoretical for G = 0.67 MPa, ℓ_t = 5.6 mm, ℓ_b = 5.4 mm, N = 1. Classical elasticity (ℓ_t = 0) predicts constant Ω = 1 independent of diameter which is indicated by the horizontal dashed line. 74
5.4 Size effects for lattice specimens in bending. Points are experimental. Curve is theoretical for ℓ_b = 5.4 mm, $\beta/\gamma + \nu$ = 0.002, N = 0.46, via Eq. 5.13. Classical elasticity predicts constant Ω = 1 independent of diameter which is illustrated by the horizontal dashed line. 75

6.1 3D printed rib structure vs. idealized drawing. Scale bar, 5 mm. 83
6.2 Cross section and side view of 3D printed lattice structure. Scale bar, 10 mm. 84
6.3 Size effects for lattice specimens in torsion. Points are experimental. The black curve is theoretical for best fit G = 1.1 MPa, ℓ_t = 9.4 mm, N = 1, Ψ = 1.0. Blue curves illustrate theoretical predictions for ℓ_t = 5.0 and 14 mm, respectively. Classical elasticity (ℓ_t = 0) predicts constant Ω = 1 independent of diameter which is indicated by the green horizontal dashed line. 87
6.4 Size effects for lattice specimens in bending. Points are experimental. The black curve is theoretical for best fit E = 3.14 MPa, ν = 0.05, ℓ_b = 8.8 mm, β/γ = 0.5, N = 0.99. Blue and cyan curves illustrate theoretical predictions for ℓ_b = 4.8 and 13 mm, respectively. Classical elasticity predicts constant Ω = 1 independent of diameter which is indicated by the green horizontal dashed line. 89

7.1 Four-sided Sarrus linkage created via SLS printing. 97
7.2 SLS printed lattices with SD cubic unit cells oriented with their <111> axes parallel to the longitudinal axes of the specimens. Scales are metric. 102

7.3 Size effects in torsion for specimens composed of SD unit cells with their <111> axes parallel to specimen axes. Points are experimental. Curve is theoretical for ℓ_t = 6.0 mm, G = 3.9 MPa, N = 1.0, and Ψ = 1.5. Fit is insensitive to Ψ because no roll off occurs at small sizes. Classical elasticity predicts Ω independent of diameter as illustrated by the red dashed line. 103
7.4 Size effects in bending for specimens composed of SD unit cells with their <111> axes parallel to specimen axes. Points are experimental. Curve is theoretical for ℓ_b = 8.2 mm, E = 6.0 MPa, N = 1.0, and β/γ = 0. Classical elasticity predicts Ω independent of diameter as illustrated by the red dashed line. 104
7.5 SLS printed lattices with SD cubic unit cells oriented with their <100> axes parallel to the longitudinal axes of the specimens. Dimensions in subcaptions are number of unit cells in cross section by number of unit cells in height. 106
7.6 Size effects in bending for specimens composed of SD unit cells with their <100> axes parallel to specimen axes. Points are experimental. Curve is theoretical for ℓ_b = 7.4 mm, E = 9.64 MPa, N = 0.23, and β/γ = 0.28. The red dashed line illustrates the relationship of rigidity to specimen diameter of classical elasticity; the two are independent. 107
7.7 Size effects in torsion for specimens composed of SD unit cells with their <100> axes parallel to specimen axes. Points are experimental. Curve is theoretical for N = 1, ℓ_t = 3.8mm, ℓ_b = 3.3 mm, and G = 4.3 MPa. Classical elasticity predicts Ω independent of diameter as illustrated by the solid red line. 109
7.8 A close-up view of the 3-D printed triangular prismatic unit cell configuration. This is the long rib (14 mm) configuration. Scale is metric. 111
7.9 Lattices composed of long triangular prismatic unit cells. 112
7.10 Torsion size effect for long triangular unit cell structures. Points are experimental and black line is theoretical best fit for G = 0.34 MPa, Ψ = 1.5, ℓ_t = 8.9 mm and N = 1.0. R^2 = 0.9988. The dashed red line illustrates the classical predicted relationship between rigidity and specimen size. 113
7.11 Bending size effects for long triangular unit cell structures. Points are experimental and black line is theoretical best fit for E = 2.3 MPa, ν = 0.05, ℓ_b = 13.2 mm, β/γ = 0, and N = 0.99. Correlation coefficient, R^2 = 0.9719. The red dashed line illustrates the classical independence of rigidity to specimen diameter. 114
7.12 A close-up view of the short rib 3-D printed triangular prismatic unit cell configuration [111]. 116
7.13 Size effects for short rib triangular prismatic unit cells in torsion. Black line is theoretical best fit for G = 1.1 MPa, ℓ_t = 9.4 mm, N = 1, and Ψ = 1.0. Blue and cyan curves are the theoretical models for ℓ_t = 5.0 and 14 mm, respectively. The green dashed line is the classically predicted relationship between rigidity and specimen size. The inset figure is the smallest specimen of this series. [111] 118

7.14 Size effects for short rib triangular prismatic unit cells in bending. Black line is theoretical best fit for E = 3.14 MPa, ν = 0.05, ℓ_b = 8.8 mm, β/γ = 0.5, and N = 0.99. Blue and cyan curves are the theoretical models for ℓ_b = 4.8 and 13 mm, respectively. The green dashed line is the classically predicted relationship between rigidity and specimen size. The inset figure is the largest specimen of this series. [111] 119

A.1 Cylindrical corrugated unit cell created via FDM from April 20, 2016. 127
A.2 FDM printed unit cell with three fold plate element corrugations and ribs at random rotational positions. April 20, 2016. 128
A.3 FDM printed unit cell with three fold plate element corrugations. April 20, 2016. . . 129
A.4 FDM printed unit cell with cylindrical corrugations and ribs. Rib length of 16mm. May 10, 2016. 130
A.5 FDM printed unit cell with three fold plate element corrugations. Rib length of 16 mm. May 10, 2016. 131
A.6 Large FDM printed unit cell with fourfold rib elements and corrugations. July 22, 2016. 133
A.7 Triangular rib unit celled printed via material jetting. July 20, 2016. 135
A.8 Cylindrical corrugated unit cell printed via SLS on July 20, 2016. 137
A.9 Triangular ribbed unit cell printed via SLS on July 20, 2016. 138
A.10 Unit cell with 8mm long ribs characterized by fourfold plate element corrugations. Note incomplete plate elements in the corrugations parallel to top and bottom surfaces. Printed via SLS on August 29, 2016. 139
A.11 Unit cell with 14mm long ribs characterized by fourfold plate element corrugations. Again, note printing defects on plate elements. Printed via SLS on August 29, 2016. . 140
A.12 Unit cell with fourfold symmetric ribs rotated 45 degrees from previous specimens. Complete plate elements. Printed via SLS on September 6, 2016. 141
A.13 Assembly of the same type of unit cells shown in Figure A.12. Printing defects can be observed in some of the plate elements in the corrugations. Printed October 14, 2016. 143
A.14 Close up image of printing defects found in the assembly shown in Figure A.13. . . 144
A.15 Assembly of unit cells of the same type shown in Figure A.11. No printing defects present. Printed October 26, 2016. 145

List of Abbreviations

BVS	**B**roadband **V**iscoelastic **S**pectroscopy
LVDT	**L**inear **V**ariable **D**isplacement **T**ransducer

To my family who supported me on every step I've taken to get here, especially my mom and dad who I will never be able to thank enough for everything they have done for me. Also to you, Becca, for supporting me through the hardest parts of grad school. I love you guys.

Chapter 1

Introduction

1.1 Background Information

1.1.1 Theories of Elasticity

Generalized continuum theories of elasticity, used to describe the mechanical behavior of materials, with varying degrees of freedom have been developed over the centuries. The following theories are pertinent only for small strain when deformation is linear. One of the first theories of elasticity, developed by Navier [1], incorporated only one elastic constant, shear modulus, and a Poisson's ratio of $1/4$ for all materials. This theory was based on the assumption that forces act along lines joining pairs of atoms and are proportional to changes in distance between them. This theory was rendered obsolete by experiments proving a range of Poisson's ratios.

The classical theory of elasticity is the next step up in generality by incorporating two elastic constants: a Lamé constant in addition to the shear modulus. The Poisson's ratio in the Classical theory can range from -1 to 0.5. An important limitation of the Classical theory is the absence of a length scale despite the presence of a length scale in the definition of fracture toughness (MPa$\sqrt{m}$)and the demonstrated relationship between toughness and length scale in foams [2].

Several more general theories of elasticity exist which explain the effects of length scales in materials. One of the first such theories is the Cosserat theory of elasticity. In 1909 E. and F. Cosserat introduced a theory of elasticity [3] involving six degrees of freedom. These additional

degrees of freedom include local rotations of points and a couple stress (torque per unit area) in addition to the translation and force stress (force per unit area) of Classical elasticity. The idea of incorporating couple stress into theories of elasticity was first presented by Voigt [4] in 1887.

During the 1960s, much work was done incorporating couples stress into theories of elasticity via modern continuum mechanics. In 1962, Mindlin and Tiersten [5] introduced a couple-stress theory in which the rotation of a point in a material is the same as the local rotation of the surrounding material. This theory represents a constrained Cosserat continuum with three degrees of freedom. Additionally, this theory contained a characteristic length parameter (couple stress constant) which is a material property. When the characteristic length parameter goes to zero, the solutions of the constitutive equations reduce to those of Classical elasticity.

In 1964, Eringen and Suhubi [6] developed a nonlinear theory of elasticity with 42 constitutive equations. In the same year, Mindlin [7], who derived a linear theory via variational principles, determined that the 42 functions reduce to 18 material constants for the linear isotropic case. This micromorphic elasticity theory has more freedom than Classical or Cosserat elasticity; it allows points to translate, rotate, and deform within the material. As a special case, if the micro-rotation tensor and the stress moment tensor are antisymmetric, the micro-rotation becomes kinematically independent of the linear displacements. Thus, the six degrees of freedom of the generalized Cosserat continuum theory are preserved. Since the stress and couple stress tensors are fully determined the number of elastic constants reduces to six. Because of the great generality of this couple-stress theory, Eringen [8] renamed it micropolar elasticity in 1966. An important aspect of micropolar elasticity is that at sufficiently low frequencies such that local resonances are not approached, it can be used interchangeably with the Cosserat theory.

1.1.2 Cosserat Elasticity

Cosserat Elasticity is the result of the Cosserat brothers working to incorporate extra degrees of freedom found in some materials, such as materials with micro- to milliscale length scales, into

continuum theories of elasticity. The constitutive equations for an isotropic Cosserat solid are [9]:

$$\sigma_{kl} = 2G\epsilon_{kl} + \lambda\epsilon_{rr}\delta_{kl} + \kappa e_{klm}(r_m - \phi_m) \tag{1.1}$$

$$m_{kl} = \alpha\phi_{r,r}\delta_{kl} + \beta\phi_{k,l} + \gamma\phi_{l,k} \tag{1.2}$$

Equations 1.1 and 1.2 use the usual Einstein summation convention and the comma represents differentiation with respect to spatial variables. The Lamé constant, λ, and $(2\mu + \kappa) = 2G$ are the same as in classical elasticity. σ_{kl} is the usual force stress tensor (asymmetric), e_{kl} is the small strain tensor defined in terms of the displacement u_k: $e_{kl} = \frac{1}{2}(u_{k,l} + u_{l,k})$, r is the macrorotation $r_m = \frac{1}{2}e_{mln}u_{n,l}$ where e_{mln} is the permutation symbol, m_{kl} is the couple stress tensor, ϕ is the microrotation vector which is kinematically independent of the macrorotation, and $\alpha, \beta, \gamma, \kappa, \mu, \lambda$ are the six elastic constants. The following technical constants, which are beneficial for physical insight, are obtained from the six aforementioned elastic constants:

$$Young's\ modulus \quad E = (2\mu + \kappa)\frac{3\lambda + 2\mu + \kappa}{2\lambda + 2\mu + \kappa} \tag{1.3}$$

$$Shear\ modulus \quad G = \frac{2\mu + \kappa}{2} \tag{1.4}$$

$$Poisson's\ ratio \quad \nu = \frac{\lambda}{2\lambda + 2\mu + \kappa} \tag{1.5}$$

$$Characteristic\ length,\ torsion \quad l_t = \sqrt{\frac{\beta + \gamma}{2\mu + \kappa}} \tag{1.6}$$

$$Characteritic\ length,\ bending \quad l_b = \sqrt{\frac{\gamma}{2(\mu + \kappa)}} \tag{1.7}$$

$$Coupling\ number \quad N = \sqrt{\frac{\kappa}{2(\mu + \kappa)}} \tag{1.8}$$

$$Polar\ ratio \quad \Psi = \frac{\beta + \gamma}{\alpha + \beta + \gamma} \tag{1.9}$$

In the case when $\alpha, \beta, \gamma, \kappa$ tend to zero, the solution for a classical solid is obtained. When N reaches its upper bound of 1, the analysis can be interpreted as couple stress theory [5] [10]

[11] also known as the Koiter variant [12]. This case corresponds to κ approaching infinity in the Cosserat theory and implies a situation permitted by energetic considerations such as incompressibility in classical elasticity. In contrast, when κ tends to 0, or equivalently, $N = 0$, the rotational and translational degrees of freedom are decoupled.

Cosserat elasticity has several key consequences in isotropic materials that differ from Classical elasticity:

1. A size effect, which is the non-classical dependence of the rigidty of an object on one or more of its dimensions, is predicted in the torsion[13] and bending[14] of circular cylinders of Cosserat elastic materials. Slender cylinders appear stiffer than predicted Classically. Similarly, a size effect is expected in the bending of plates[13]. No size effects are predicted in Classical elasticity.

2. The stress concentration around a circular hole is smaller than expected classically and the smaller holes demonstrate less stress concentration than larger holes [15]. Stress concentration near cracks and elliptic holes is reduced from Classcial predictions [16].

3. The speed of shear waves in a Cosserat solid is dependent on frequency [9]. Additionally, a new kind of wave associated with micro-rotations is predicted for Cosserat solids [17].

The ordinary (force) stress represents a spatial average of force per unit area. Similarly, the couple stresses in the Cosserat theory represent spatial averages of distributed moments per unit area. As Kröner [18] demonstrated, these moments can occur because interatomic forces propagate further than one atomic spacing. This effect occurs in all solids, but the corresponding characteristic lengths are typically too small for mechanical experimentation - on the atomic or nanoscale.

However, research has been accomplished developing new experimental methods for measuring characteristic lengths in the micro- to nanoscale. Stolken and Evans [19] developed a microbend test method to measure material length scales as small as 3 micrometers. More Recently, Zhao et. al [20] used a method of nanoindentation to measure the characteristic length of strain-gradient plasticity in single crystals of Al, Ag, Ni, and polycrystalline Cu. This experimentation

measured characteristic lengths ranging from 2762 nm down to 49 nm. Experimental techniques for measuring length scales smaller than these do not currently exist.

Moments can also be transmitted along the fibers in fiber-reinforced composites [21] or along the cell walls or ribs in cellular solids [22] [23]. These situations provide sufficiently large length scales - in the microscale or milliscale - for mechanical testing and measurement of the characteristic lengths.

The size effects of Cosserat elasticity are most apparent in materials with microstructure in the microscale to milliscale at a minimum. For example, Chong and Lam [24] encountered size effects in the bending of thermosetting epoxy microcantilevers - the normalized bending rigidity of the microcantilevers increased as the beam thickness decreased. Additionally, size effects have been observed in torsion and bending of dense (340 kg/m^3) polyurethane closed cell foam[22] with cell sizes ranging from 0.5 to 0.15 mm and dense (380 kg/m^3) polymethacrylamide closed-cell foam[23] with an average cell size of 0.65 mm. However, large microstructure does not guarantee that size effects will occur. Gauthier and Jahsman [13] designed a composite of aluminum beads in an epoxy matrix and found that it behaved according to Classical elasticity.

1.2 Motivation

Classical elasticity is entirely adequate for describing macroscopic specimens of metal in which the structure size is many order of magnitude smaller than the experimental size scale; macroscopic scales tests for Cosserat effect in aluminum revealed classic behavior [25]. However, classical elasticity breaks down as the structural size scale approaches that of the experimental size scale. Wave dispersion was used to infer Cosserat behavior in diamond crystals [26]; the inferred characteristic length was about 0.2 nm. More recently, classical elasticity [27] was predicted to break down in crystalline materials in the length scale range of 1-10 nm. Compounding on the key differences between Cosserat and Classical elasticity listed above, M. Rahaeifard et al. [28] demonstrated the limitation of Classical elasticity in their analysis of static pull-in of microcantilevers. The Classical

theory of elasticity failed to predict the pull-in instability which occurs in these microcantilevers when they were gradually deflected. Similarly, Kahrobaiyan et al. [29] proved the inability of Classical elasticity to interpret size effects in the resonant frequency and sensitivity of atomic force microscope (AFM) microcantilevers. A more descriptive theory of elasticity is necessary to adequately model and predict the mechanical behavior of materials than the current classical theory.

As outlined above, Cosserat elasticity is a good option to provide a richer framework for describing and understanding a wide range of materials. Therefore, characterizing a range of materials and structures via Cosserat elasticity will facilitate a novel approach to the creation of new metamaterials. This approach entails engineering microstructures that have and enhance specific Cosserat moduli characteristics of other tested materials. Additionally, the amount of experimental work done on characterizing materials via generalized continuum theories is shockingly small compared to the amount of theoretical work done on the same topic. Experimental work needs to be performed to provide balance in this field.

Stated previously, toughness by definition has a length scale - MPa$\sqrt{m}$. Yet, toughness is often characterized in the context of molecular or nanoscale physics which do not take into account the role of the length scale of the largest structural elements in the material. Understanding materials by Cosserat elasticity remedies this issue. Also, because of the difference in stress concentrations predicted by Cosserat elasticity, describing materials by this theory has the potential to better predict the failure of materials by certain stress concentrators such as holes and cracks. This reinforces the potential ability to design novel ultratough materials by Cosserat theory.

In summary, the currently accepted Classical theory of elasticity has many limitations when it comes to describing the mechanical behavior of materials. Cosserat elasticity provides a richer framework to understand and describe materials by means of its additional degrees of freedom when compared to the Classical theory - a local rotation of points and a couple stress. By using this more descriptive framework, my research aims to provide a new way to characterize materials and increase understanding of what produces specific characteristics. Eventually, these findings aim to aid in the creation of new ultratough materials via optimzation and enhancement of the

Cosserat characteristics of the toughest tested materials.

1.3 Thesis Organization

This RRE docment is organized as follows. Chapter 2 demonstrates the applicability and descriptive power of the Cosserat theory to reticulated open cell polymer foam while simultaneously revealing the limitations of the Classical theory of elasticity. Size effects are observed in torsion and bending of circular cylindrical specimens of the foams. The characteristic lengths in torsion and bending and the coupling number, N, are extracted and discussed. The experimental results are compared with other results from literature to determine the mechanism governing deformation and Young's modulus of the materials. Lastly, asymmetry of stress was inferred via notch displacement testing to clearly demonstrate deviation from classical predictions and predictive power of the Cosserat theory.

In Chapter 3, a similar analysis as Chapter 2 is performed on a negative Poisson's ratio foam derived from the large open cell reticulated polymer foam from Chapter 2. Size effects are experimentally measured and the characteristic lengths and coupling number are extracted and compared to the results from Chapter 2. Experimental results are compared with the literature and those from Chapter 2 to determine the deformation mechanism.

Chapter 4 explores engineered unidirectional composites of corrugated nylon tubing and silicone rubber cement. The segments of corrugated nylon tubing are predicted to be sensitive to strain gradients in torsion and bending. Size effects in torsion and bending are measured and analyzed. The Cosserat elastic constants are extracted, compared to prior results and literature, and used to understand the deformation mechanics.

Tetragonal lattices with a negative Poisson's ratio, designed by visiting scholar Dr. Dong Li, are analyzed in Chapter 5. These lattices have square cross sections so approximate solutions for the bending and torsion of Cosserat elastic materials with square cross sections are used for

analysis. Experimentally measured size effects are interpreted using these solutions. Cosserat elastic constants are extracted and deformation mechanics determined.

Chapter 6 details the results from analysis of an engineered transversely isotropic polymer lattice as Cosserat material. These lattices were developed as a culmination of concepts learned from prior studies. The same experimental method and analysis is carried out as in previous chapters.

A detailed explanation of the path that led to the lattices in Chapter 6 is presented in Chapter 7. Experimental results and analysis are presented for several different 3D printed lattices. Structures with strengthened diagonal (SD) unit cells incorporating Sarrus linkages in two different orientations are explored in addition to another set of lattices built using triangular prismatic unit cells.

Lastly, a summary of results and important concepts is presented in Chapter 8. Also, projects still in progress and ideas for future work are covered here.

Chapter 2

Experimental Cosserat elasticity in open cell polymer foam

The following chapter has been published:
Z Rueger and R.S. Lakes, "Experimental Cosserat elasticity in open cell polymer foam", Philosophical Magazine, **96** (2), 93-111 (2016).

Abstract Reticulated open cell polymer foams exhibit substantial size effects in torsion and bending: slender specimens are more rigid than anticipated via classical elasticity. Such size effects are predicted by Cosserat (micropolar) elasticity, which allows points to rotate as well as translate and incorporates distributed moments (couple stresses). The Cosserat characteristic length is larger than the cell size. The Cosserat coupling coefficient is larger than in dense closed cell foams and approaches 1 for foam with 0.4 mm cells.

2.1 Introduction

Materials that are deformed at sufficiently small strain typically exhibit linear behavior. If the response is also independent of the path of deformation and its time history, the material is considered to be elastic. Classical elasticity is routinely used to model such behavior. There is no length scale in classical elasticity. Length scales do occur in the definition of fracture toughness.

Also, toughness of foams is related to the size scale of the cells in the foam [2]. Effects of material length scales may be understood in the context of more general theories of elasticity.

Classical elasticity however is not the only theory of elasticity. Theories that incorporate less freedom or more freedom are available. The Cosserat theory of elasticity [3] [30] incorporates a local rotation of points as well as the translation of classical elasticity, and a couple stress (a torque per unit area) as well as the force stress (force per unit area; just stress in classical elasticity). Eringen [9] incorporated micro-inertia and renamed Cosserat elasticity micropolar elasticity. At frequencies sufficiently low that local resonances are not approached, Cosserat and micropolar are used interchangeably.

The physical origin of the Cosserat couple stress is the summation of bending and twisting moments transmitted by ribs in a foam or by structural elements in other materials (Figure 2.1). The Cosserat local rotation corresponds to the rotation of ribs. Forces and moments are also considered in the classic analyses of foam by Gibson and Ashby [2] in which classical elastic moduli were determined; effects of rotation gradients were not considered.

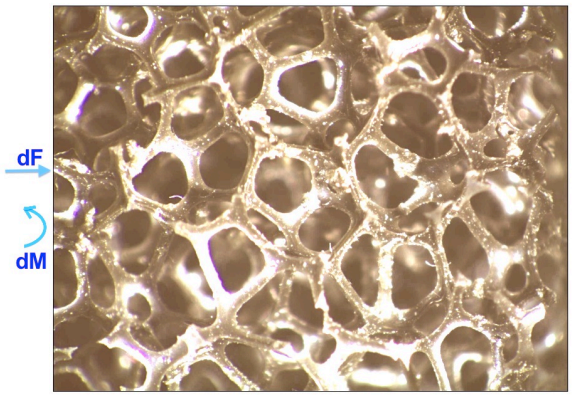

FIGURE 2.1: Foam ribs with increment of force dF and increment of moment dM upon ribs.

The Cosserat theory of elasticity is a *continuum* theory that entails a type of nonlocal [31] interaction. The stress σ_{jk} (force per unit area) can be asymmetric. The distributed moment from this

asymmetry is balanced by a couple stress m_{jk} (a torque per unit area). The antisymmetric part of the stress is related to rotations. $\sigma_{jk}^{antisym} = \kappa e_{jkm}(r_m - \phi_m)$ in which κ is an elastic constant, ϕ_m is the rotation of points, called micro-rotation, e_{jkm} is the permutation symbol, and $r_k = \frac{1}{2} e_{klm} u_{m,l}$ is "macro" rotation based on the antisymmetric part of gradient of displacement u_i. The constitutive equations [9] for linear isotropic Cosserat elasticity are as follows.

$$\sigma_{ij} = 2G\epsilon_{ij} + \lambda\epsilon_{kk}\delta_{ij} + \kappa e_{ijk}(r_k - \phi_k) \tag{2.1}$$

$$m_{ij} = \alpha\phi_{k,k}\delta_{ij} + \beta\phi_{i,j} + \gamma\phi_{j,i} \tag{2.2}$$

Cosserat elasticity incorporates sensitivity to gradients of rotation by virtue of the coupling between rotations and stresses. It is also possible to supplement classical elasticity with sensitivity to gradients of dilatation [32].

The six isotropic Cosserat elastic constants are as follows in which λ is a Lamé constant from elasticity theory.

$$Young's\ modulus \qquad E = \frac{G(3\lambda + 2G)}{\lambda + G} \tag{2.3}$$

$$Shear\ modulus \qquad G \tag{2.4}$$

$$Poisson's\ ratio \qquad \nu = \frac{\lambda}{2(\lambda + G)} \tag{2.5}$$

$$Characteristic\ length,\ torsion \qquad \ell_t = \sqrt{\frac{\beta + \gamma}{2G}} \tag{2.6}$$

$$Characteristic\ length,\ bending \qquad \ell_b = \sqrt{\frac{\gamma}{4G}} \tag{2.7}$$

$$Coupling\ number \qquad N = \sqrt{\frac{\kappa}{2G + \kappa}} \tag{2.8}$$

$$Polar\ ratio \qquad \Psi = \frac{\beta + \gamma}{\alpha + \beta + \gamma}. \tag{2.9}$$

Cosserat elasticity has the following consequences. A size effect is predicted in the torsion [13] and bending [14] of circular cylinders of Cosserat elastic materials. Slender cylinders appear more stiff than expected classically. A similar size effect is also predicted in the bending of plates. No size effect is predicted in tension or compression. The stress concentration factor for a circular hole is smaller than the classical value, and small holes exhibit less stress concentration than larger ones [15]. By contrast, in classical elastic solids, there is no size effect in torsion or bending; structural rigidity goes as the fourth power of the radius; too, stress concentration is independent of hole size.

As for freedom of theories, the early uniconstant elasticity theory of Navier [1] has less freedom than classical elasticity; it has only one elastic constant and Poisson's ratio must be $\frac{1}{4}$ for all materials. This theory is based upon the assumption that forces act along the lines joining pairs of atoms and are proportional to changes in distance between them. This theory was abandoned based on *experiments* that disclosed a range of Poisson's ratio. Classical elasticity has two independent elastic constants for isotropic materials; the Poisson's ratio can have values between -1 and 0.5. Cosserat elasticity has more freedom than classical, that of local rotations and couple stress; there are 6 independent isotropic elastic constants. A simpler variant presented by Koiter [12] assumes that the macrorotation and microrotation vectors are equal. This corresponds to $N = 1$, or equivalently $\kappa \to \infty$ in Cosserat elasticity. The Koiter variant is called couple stress elasticity; there are two characteristic lengths in addition to the classical constants: 4 isotropic elastic constants. The microstructure elasticity theory of Mindlin [7], also called micromorphic elasticity, has more freedom than classical or Cosserat elasticity; it allows points in the continuum to translate, rotate, and deform. This adds considerable complexity; for an isotropic solid, there are 18 micromorphic elastic constants compared with 6 for Cosserat elasticity and 2 for classical elasticity.

Cosserat elastic effects have been observed experimentally. Size effects observed to occur in torsion and bending of closed cell foams [22], [23] and of compact bone [21] are consistent with Cosserat elasticity. The apparent modulus increases substantially as the specimen diameter becomes smaller, in contrast to the predictions of classical elasticity. Cosserat elasticity can account

for these observations. For dense (340 kg/m^3) closed cell polyurethane foam [22], E = 300 MPa, G = 104 MPa, ν = 0.4, ℓ_t = 0.62 mm, ℓ_b = 0.33 mm, N^2 = 0.04, Ψ = 1.5. The cell size ranges from 0.05 mm to 0.15 mm. For dense (380 kg/m^3) polymethacrylamide closed cell foam (Rohacell WF300) [23], E = 637 MPa, G = 285 MPa, ℓ_t = 0.8 mm, ℓ_b = 0.77 mm, $N^2 \approx 0.04$, Ψ = 1.5. The cell size is about 0.65 mm. For this material, it was difficult to determine N accurately due to difficulty in cutting sufficiently slender specimens.

The Cosserat characteristic length was determined in a (two dimensional) polymer honeycomb [33]. Full field measurements of deformation reveal non-classical elastic effects that are consistent with Cosserat elasticity. Warp of a bar of rectangular cross section in torsion is predicted to be reduced in a Cosserat elastic solid [34]. The corresponding non-classical strain field was observed in compact bone [35]. Deformation spills over into the corner region where it would be zero in classical elasticity [36] as revealed by holography. This ameliorates concentration of strain. Strain at the corner entails asymmetry of the stress as predicted by Cosserat elasticity. The reduction of warp deformation has been observed via holography [37]. As for plastic deformation, rotational plastic deformation mechanisms were interpreted via gradients in a micropolar continuum theory [38].

The present research deals with experimental study of size effects and Cosserat elasticity in low density open cell polymer foams.

2.2 Methods

2.2.1 Materials and experiment

Reticulated polyurethane foam (Scott Industrial foam [39]) was used. One foam had average cell size 1.2 mm or 20 pores per inch (Figure 2.2); the other foam had average cell size 0.4 mm. For both foams, the density was 30 kg/m^3 so the volume fraction of solid material in the foam was about 0.03.. Separate compression tests on foam cubes were conducted with a servo-hydraulic frame to probe anisotropy.

Cylinders were cut from polymer foam with a hot wire cutter such that the cylinder diameter and length were equal. The wire was Nichrome heater wire of thickness 0.015 inches and resistance 2.5 Ω. The electric current was 3 Amps. The initial cylinder cut from the bulk foam was 45 mm in both diameter and length. The foam cylinder was weighed with an analytical balance, then circular end pieces of the same diameter as the foam specimen were cut from heavy card stock and cemented with cyanoacrylate (Loctite 401) over the full surface. Slight pressure was applied to the end pieces to ensure good adhesion. A catalyst was applied to the surfaces to minimize the amount of cement in order to reduce ingression of the cement into the pores of the smaller cell foam.

These specimens were tested for torsional and bending rigidity using a Broadband Viscoelastic Spectrometer (BVS) [40] [41]. This instrument makes use of a Helmholtz coil acting upon a magnet attached to the specimen to generate torque. The coil spacing is smaller than the larger specimens so a short stalk with a magnet and mirror on the end was fixed to one of the end pieces. A thin aluminum end layer was also cemented to provide a sufficiently rigid attachment for the stalk. First, a small mirror was glued to one face of a cubic magnet. The magnet was then calibrated using the BVS and a lock-in amplifier. The magnetic calibration constants of this particular magnet were obtained by testing a 6061 aluminum alloy rod of known elastic properties; the calibration constants were 8.00 $\times 10^{-6}$ Nm/A in torsion and 1.84 $\times 10^{-5}$ Nm/A in bending. The free end piece of the polymer foam cylinder was cemented to a steel adapter which was screwed in to a 25 mm thick steel rod for holding the specimen inside the BVS. Prior to testing, viscoelastic strain was allowed to recover overnight to enable stable measurements. The specimen (Figure 2.3a) was lowered into the BVS such that the magnet was centered in the Helmholtz coils of the BVS. The lower limit on specimen size was imposed by obtrusive presence of incomplete cells, particularly in the larger cell foam; also by difficulty in handling. The smallest specimen of 0.4 mm cell foam is shown in Figure 2.3b.

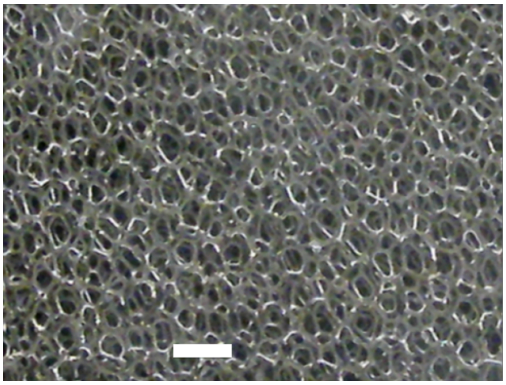

(A) Larger cells, scale bar 5 mm.

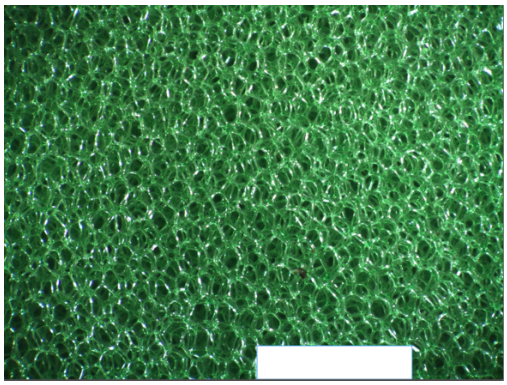

(B) Smaller cells, scale bar 5 mm.

FIGURE 2.2: Open cell polyurethane foam samples.

Deformation was measured via a beam from a semiconductor laser reflected from a mirror attached to the magnet that applies torque to the specimen free end. The laser beam was reflected onto a silicon light detector. Prior to torsion tests, the laser based displacement sensor was calibrated. This was done by aligning the laser beam so that the position of the beam on the light detector was centered. The light detector was moved a known amount via a calibrated stage; a calibration curve was obtained via micrometer adjustment. This change in output voltage per change in position was used as the beam position calibration constant (in V/μm).

To test the specimen a sinusoidal signal with a frequency of 1 Hz from a function generator (SRS Model DS345) was input to the torsion Helmholtz coil. Because the same frequency was used for all specimen diameters, viscoelastic effects are decoupled from the size effects to be probed. The torque signal was obtained as the voltage across a 1 ohm resistor in series with the coil to eliminate effects of inductive reactance from the coil. The frequency of 1 Hz was well below any resonant frequencies. The torque signal vs. angular displacement signal was displayed on a digital oscilloscope (Tektronix TDS3014B) using DC coupling. The torque and angle signals were displayed as a Lissajous figure, and used to calculate the modulus and viscoelastic damping of the material. The maximum strain during testing was less than 0.3%. This is well within the linear

range of 5-10% for this sort of flexible foam. Linearity was also checked by conducting tests at different amplitude; moduli were independent of amplitude. Linear viscoelasticity was verified by observing the shape of the elliptic torque-angle curve, an elliptic Lissajous figure. The light detector was sufficiently sensitive that quality of the signals was good and the ratio of signal to noise was high, 40 to 400.

For bending, the light detector mode was switched to vertical detection and the beam calibration constant was determined accordingly; the driving signal was input to the orthogonal bending Helmholtz coil. A correction was applied to account for the additional bending moment imposed by the weight of the magnet and stalk; this correction was 3% or less. A correction was also applied to the effective specimen length to incorporate the effect of glue in the pores at the ends. The glue ingression was 0.3 mm or less per end. The correction was at most 10% for the smallest specimen of small cell foam and considerably less otherwise.

Compression tests were done to ascertain the behavior in the absence of macroscopic gradients of strain or rotation. This was done by applying force via dead weights on one end piece cemented to the specimen. The other end piece was cemented to a base upon an optical table. Deformation was measured using an LVDT; its stem was cemented to the upper end piece. The LVDT was calibrated using a micrometer driven translation stage. The maximum strain achieved was 1.1%, well within the linear range for a flexible foam. A lower limit on specimen size was imposed by the tendency of small specimens to buckle.

Square section specimens of rubber and of foam with 0.4 mm cells were subjected to torsion with the aim of illustrating the effect of asymmetric stress in Cosserat elasticity. A small notch, about 1/15 the specimen width, was observed. In classical elasticity the notch will not displace because the symmetry of the stress implies zero stress, hence zero strain at the corner. In a Cosserat solid, the stress is asymmetric, so the notch can displace [34]; such displacement was observed in bone and dense foams [36].

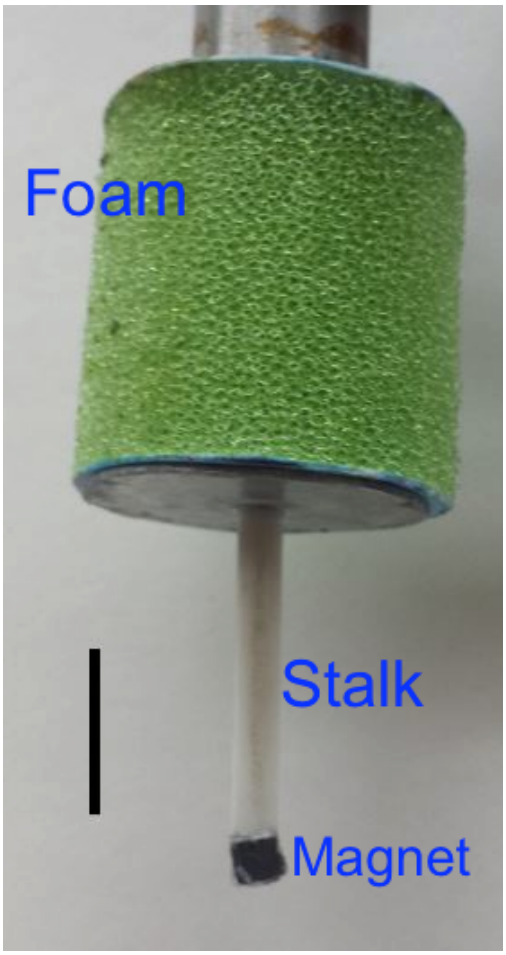

(A) Larger specimen, scale bar 10 mm.

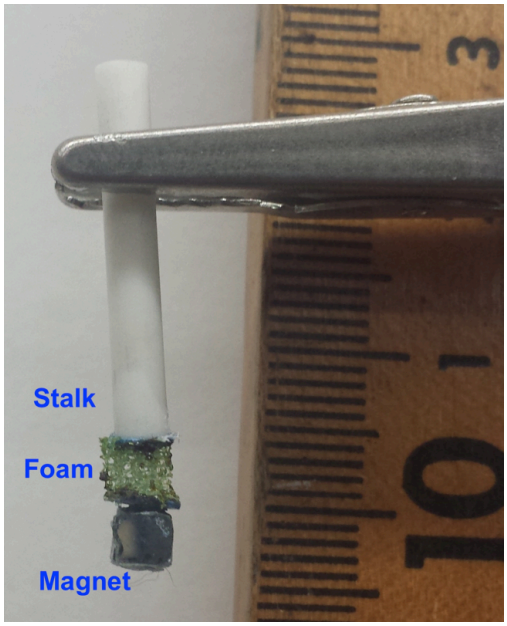

(B) Smallest specimen, scale marks 1 mm.

FIGURE 2.3: Specimens created from 0.4 mm cell foam.

2.2.2 Analysis and interpretation

Size effect results were interpreted as follows. For torsion, the shear modulus G was found from the asymptote of rigidity vs. diameter curve for large size. The torsion characteristic length ℓ_t was found from fitting the points for the larger specimens to the following approximate solution. For torsion of a Cosserat elastic circular rod of radius r, ratio of structural rigidity to its classical

counterpart (in the absence of gradient, for large diameter) is

$$\Omega = 1 + 6(\ell_t/r)^2. \tag{2.10}$$

This shows size effects to occur in torsion: slender specimens appear to have a higher effective modulus than thick ones. The classical torsional rigidity is $\frac{M}{\theta} = G[\frac{\pi}{2}r^4]$ so for Cosserat elasticity in this regime, $\frac{M}{\theta} = G[\frac{\pi}{2}r^4](1 + 6(\ell_t/r)^2)$. G is the true shear modulus in the absence of gradients; M is applied moment and θ is angular displacement. This expression is exact for N = 1; for other N the exact solution is more complicated and involves Bessel functions [13]:

$$\Omega = (1 + 6(\ell_t/r)^2)[\frac{(1 - 4\Psi\chi/3)}{1 - \Psi\chi}], \tag{2.11}$$

in which $\chi = I_1(pr)/prI_0(pr)$, $p^2 = 2\kappa/(\alpha + \beta + \gamma)$ and I_0 and I_1 are modified Bessel functions of the first kind.

The shear modulus G and characteristic length ℓ_t were determined by fitting experimental data for the three largest specimens to Eq. 2.10. The value of N was found by fitting Eq. 2.11 to the full data set using MATLAB. The curve is rather insensitive to Ψ except near the origin.

For bending, the classical bending rigidity is $\frac{M}{\theta} = E[\frac{\pi}{4}r^4]$. For bending of a Cosserat elastic circular rod and radius r, the rigidity ratio is approximately

$$\Omega = 1 + 8(\ell_b/r)^2\frac{(1 - (\beta/\gamma)^2)}{(1 + \nu)}. \tag{2.12}$$

The expression is approximate for small characteristic length $\ell_b << r$. The exact form [14], which also involves Bessel functions, is

$$\Omega = 1 + 8(\ell_b/r)^2\frac{(1 - (\beta/\gamma)^2)}{(1 + \nu)} + \frac{8N^2}{(1 + \nu)}[\frac{(\beta/\gamma + \nu)^2}{\zeta(\delta a) + 8N^2(1 - \nu)}] \tag{2.13}$$

with $\delta = N/\ell_b$ and $\zeta(\delta r) = (\delta r)^2[((\delta r)I_0((\delta r)) - I_1((\delta r)))/((\delta r)I_0(\delta r) - 2I_1(\delta r))]$.

The Young's modulus E and an initial value for the characteristic length ℓ_b were determined by fitting data for the three largest specimens to Eq. 2.12, with N input from the torsion analysis, β/γ = 0.8 based on prior dense foam and also from lattice analysis (see below), and ν from prior experimental results. Finally the values of ℓ_b and β/γ were found by fitting Eq. 2.13 to the full data set using MATLAB.

To obtain all six Cosserat constants, both torsion and bending experiments are required. The bend test provides some verification in that the shape of the size effect curve depends not only on E and ℓ_b but also on N and ℓ_t.

2.3 Results and discussion

2.3.1 Size effects and elastic constants

Density of foam specimens was independent of size to within a few percent. As for tests of anisotropy, the foam with 1.2 mm cells was anisotropic, with a ratio of compressive moduli in different directions of 1.6; the foam with 0.4 mm cells was isotropic to within 10%. Anisotropy was not obvious in images of foam observed from different directions.

Results of torsion size effect studies on the foam with 1.2 mm cells are shown in Figure 2.4. Also shown for comparison are theoretical curves for various N. Classical elasticity corresponds to a horizontal line with Ω = 1.

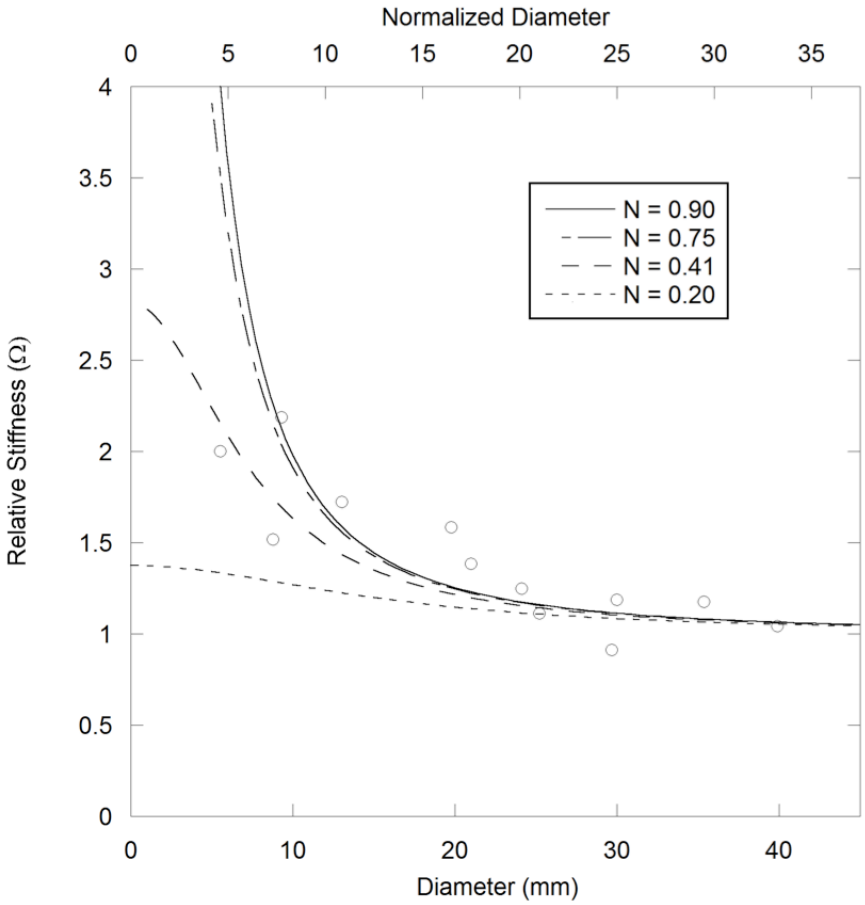

FIGURE 2.4: Size effects for foam with 1.2 mm cells in torsion. Top scale, diameter normalized to cell size. Open circles represent experimental results.

The torsion size effect curve for foam with 1.2 mm cells is consistent with G = 45 kPa, The characteristic length for torsion was ℓ_t = 2.1 mm, N = 0.41, and Ψ = 1.5. The curve is rather insensitive to Ψ except near the origin.

The Poisson's ratio was determined [42] to be approximately 0.3. This value was also given by [2] as the mean of many measurements by various authors.

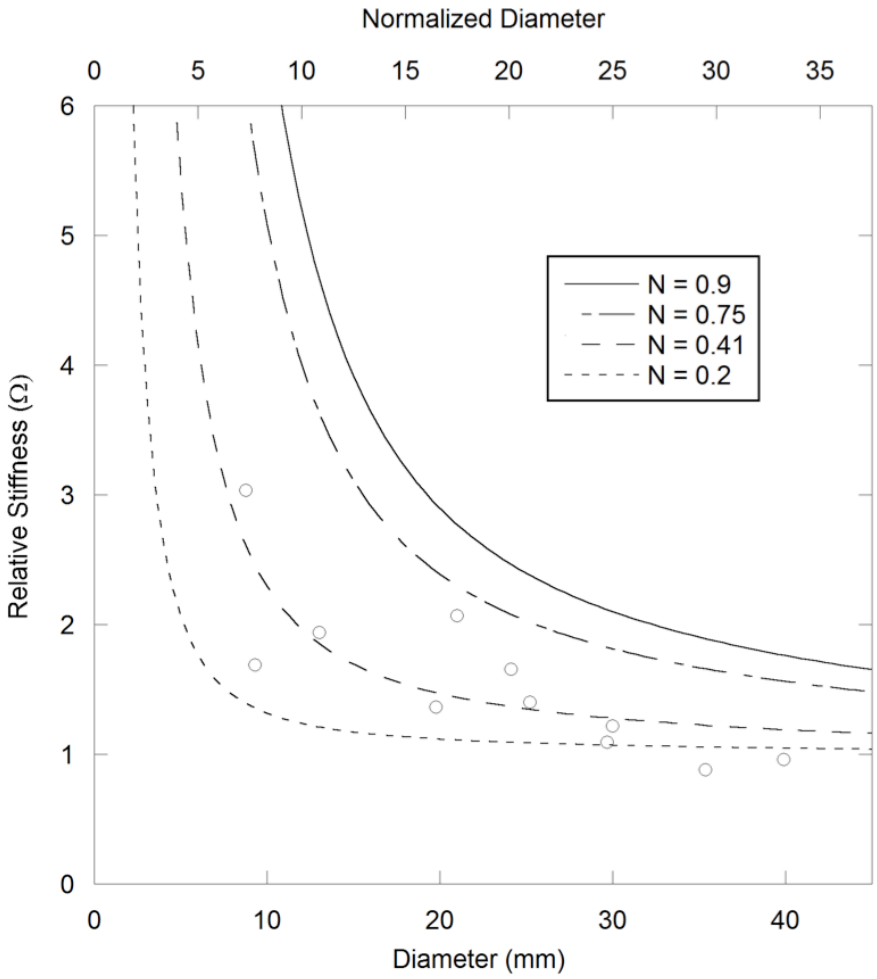

FIGURE 2.5: Size effects for foam with 1.2 mm cells in bending. Top scale, diameter normalized to cell size. Open circles represent experimental results.

Results of bending size effect studies on the foam with 1.2 mm cells are shown in Figure 2.5. As above, theoretical curves for various N are shown for comparison. The elastic constants obtained from the fit were E = 91 kPa, ℓ_b = 9 mm, $\beta/\gamma = 0.83$. N = 0.41 was used based on torsion. This foam is anisotropic, so the characteristic length for bending is independent of the characteristic length for torsion and is independent of β/γ inferred from bending.

Results of torsion size effect studies on the foam with 0.4 mm cells are shown in Figure 2.6; results for bending are shown in Figure 2.7. Classical elasticity corresponds to a horizontal line

with Ω = 1. Inferred elastic constants are shear modulus G = 28 kPa, characteristic length for torsion ℓ_t = 1.6 mm, N = 0.99, and Ψ = 1.5; Young's modulus E = 81 kPa, ℓ_b = 2.2 mm, $\beta/\gamma = 0.8$. As a test of sensitivity, the point for the smallest specimen was omitted and another curve fit done; this resulted in N = 0.82; the mean square deviation between data and theoretical fit changed minimally by 5%.

Characteristic length values were larger for the larger cell foam as expected. The difference was, however, not directly proportional to the cell size. That is not surprising because the foams do not have identical structure; the foam with larger cells exhibited anisotropy. Too, surface tension during foam formation influences the details of the microstructure.

The inferred N was larger for the 0.4 mm cell foam: 0.99 vs. 0.41. The R^2 value as a measure of goodness of fit was compared for several values of N. For the 0.4 mm cell foam, $R^2 = 0.98$ for N = 0.99; 0.6 for N = 0.6. For the 1.2 mm cell foam, R^2 = 0.65 for N = 0.41; R^2 = 0.4 for N = 0.3 or 0.55. The difference in N is attributed to differences in the structure of the foams, especially the presence of incomplete cells in the 1.2 mm cell foam as discussed below.

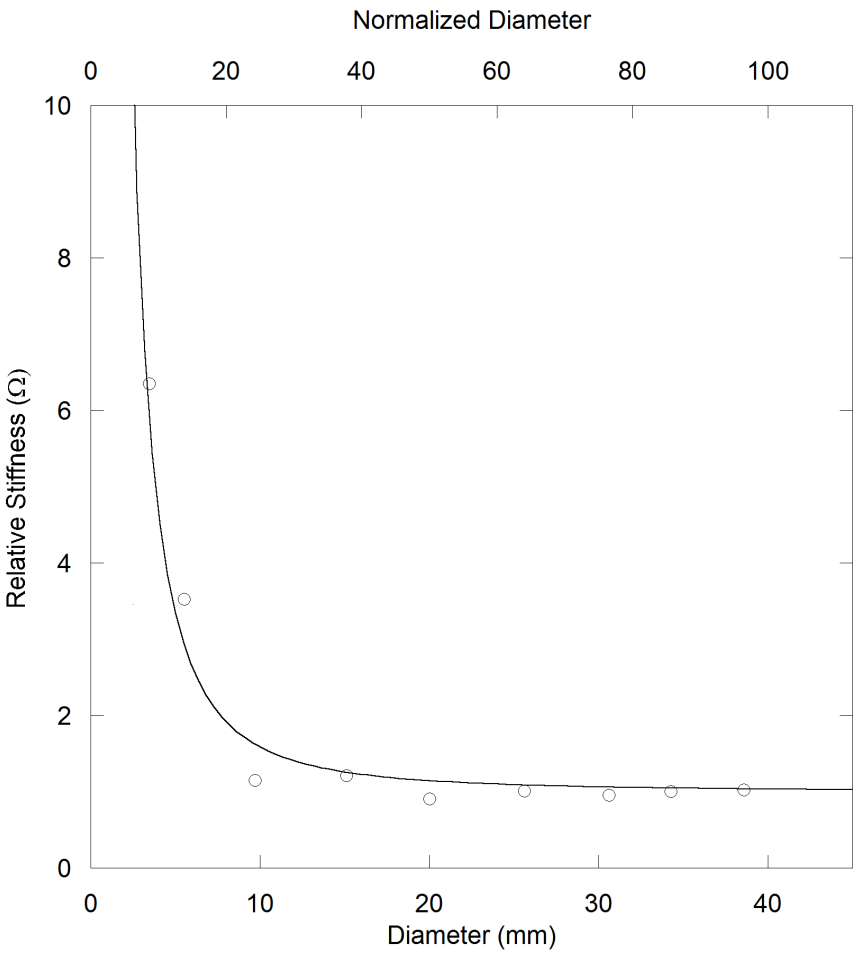

FIGURE 2.6: Size effects for foam with 0.4 mm cells in torsion. Top scale, diameter normalized to cell size. Open circles represent experimental results.

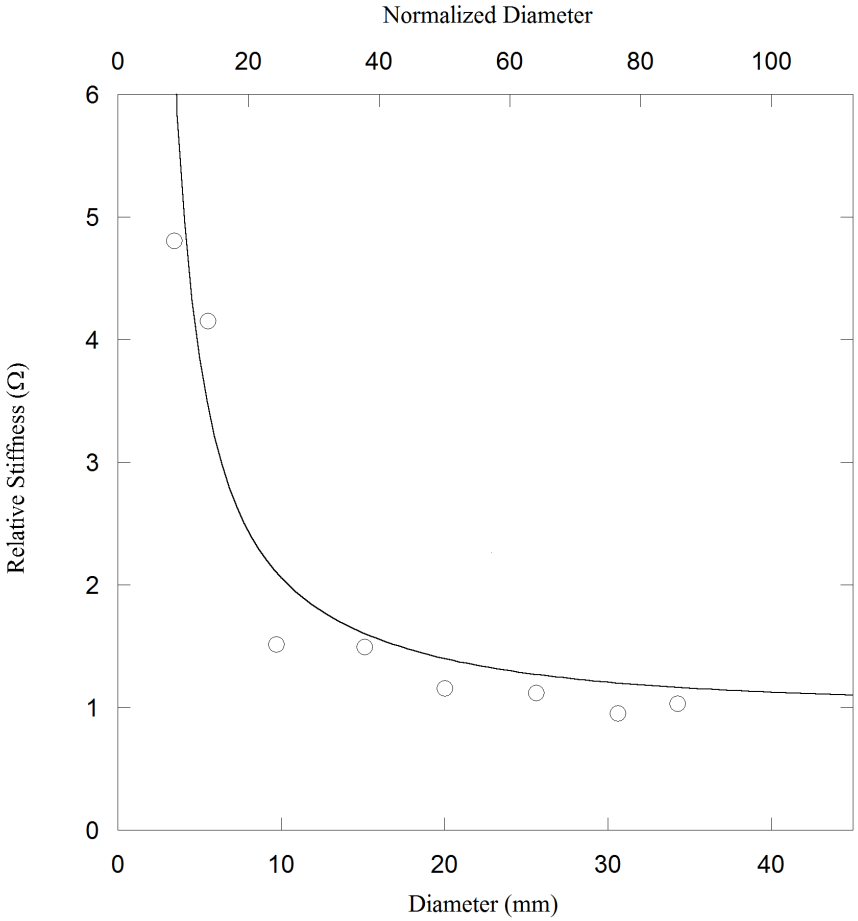

FIGURE 2.7: Size effects for foam with 0.4 mm cells in bending. Top scale, diameter normalized to cell size. Open circles represent experimental results.

Compression studies disclosed a modest softening size effect in which slender specimens have a smaller effective Young's modulus than thicker ones, Figure 2.8. Straight lines are least squares fits. This effect is opposite to the torsion and bending size effects observed and is opposite to the predictions of Cosserat elasticity. It is consistent with the notion of a surface layer of incomplete cells which do not fully contribute to the structural stiffness of the specimen.

A softening size effect is known to occur in foams as a result of damaged or incomplete cells at the surface [43] [23]. Softening size effects have also been observed in metal foams in compression

and bending; these have been analyzed and attributed to strain localization [44]. Such localization can occur in foam at sufficiently high strain levels. Incomplete cells can also contribute to the fluctuation in effective stiffness with specimen size. Such fluctuation or scatter was observed to be considerably greater in the present low density open cell foams than it was for closed cell foams. Scatter was a result of material heterogeneity, not signal quality (which was good). Too, the low density foams may have heterogeneity on a scale larger than the cells. The effect of incomplete cells is for the effective modulus to becomes smaller as specimen size is reduced. This effect was observed in the compression studies in which average stress is constant and there is no contribution from Cosserat or other gradient related effect. The effect of incomplete cells in the bending and torsion studies is to reduce the inferred Cosserat constants, so the intrinsic Cosserat elastic constants will be even larger than those reported.

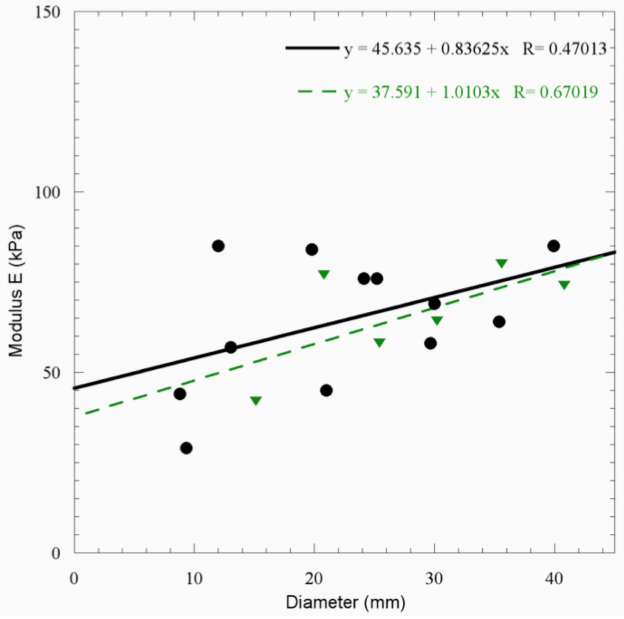

FIGURE 2.8: Young's Modulus of foam in compression; circles, foam with 1.2 mm cells; triangles, foam with 0.4 mm cells.

2.3.2 Viscoelastic damping

Viscoelastic response, was determined as mechanical damping tan δ at 1 Hz. Because the same frequency was used for all experiments, viscoelastic dispersion (frequency dependence of modulus) cannot obtrude in the results or their interpretation. Damping of 1.2 mm cell foam was essentially independent of specimen size, as shown in Figure 2.9. Straight lines are least squares fits. The foam with smaller cells (Figure 2.10) also exhibited damping independent of size. So the Cosserat effects entail viscoelasticity but there is no size dependence of the damping. This is in contrast with the behavior of bone [45] which behaves as a Cosserat solid [21]. Size effects of large magnitude were observed in the torsional effective shear modulus and damping of bovine plexiform bone. Damping increased and stiffness decreased with bone specimen size. Bone in contrast to foam has heterogeneity with spatially varying viscoelastic response, specifically there are highly viscoelastic boundaries called cement lines between large fibers (osteons) in the bone [46]. As for the present foams, the difference in the overall damping of the two foams suggests a difference in chemical composition or density of cross links. From the foam density and modulus, The Young's modulus E_s of the solid material of which the foam is made is calculated from the classic Gibson-Ashby [2] relation $\frac{E}{E_s} = C_f[\frac{\rho}{\rho_s}]^2$ between rib modulus E_s and foam modulus E in which ρ_s is the density, C_f is a constant of value near one. For both foams, the rib Young's modulus is about 90 MPa, well into the transition or leathery regime for a polymer. The relatively large tan δ is understandable in that context.

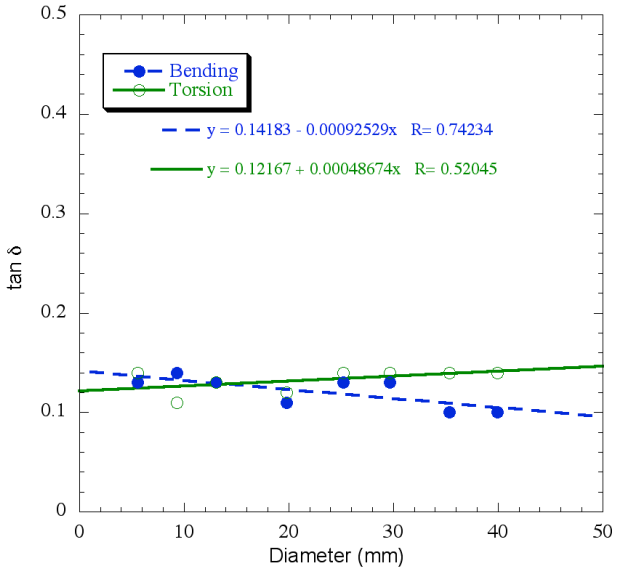

FIGURE 2.9: Viscoelastic tan δ vs. specimen size for foam with 1.2 mm cells. Solid symbols and dash line fit: bending. Open symbols and solid line fit: torsion.

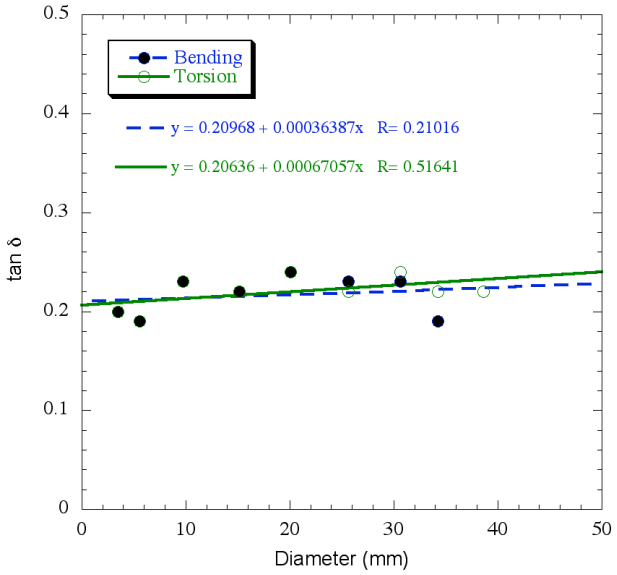

FIGURE 2.10: Viscoelastic tan δ vs. specimen size for foam with 0.4 mm cells. Solid symbols and dash line fit: bending. Open symbols and solid line fit: torsion.

2.3.3 Comparison with homogenization

Results show large characteristic lengths considerably larger than the cell size and large values of N. Comparison with homogenization analyses and with other experiment is of interest.

Lattices with straight ribs have analyzed as Cosserat continua [47] [48] [49]; homogenization such as long wave approximation reveals similarity to the Cosserat equations [47]. For cubical closed cells with thin walls [49], $\ell = h/2\sqrt{3}$ is considerably smaller than the cell size h. These lattices are stretch dominated: the effective Young's modulus of the lattice is governed by stretching or compression of the ribs or plates comprising the lattice. Cosserat effects depend on bending or twisting of the ribs. If the ribs are slender, bending or twisting moments in them decrease more rapidly than axial forces, so Cosserat effects are weak. Analysis of two dimensional chiral honeycomb lattice structures as Cosserat continua reveals bend dominated behavior in which Young's modulus is governed by rib bending. These honeycombs have large N approaching its upper bound 1, and characteristic length ℓ comparable to the cell size [50]. The ribs of this lattice are bend dominated is in contrast to prior stretch dominated lattices that have been analyzed thus far [51] [52] [53], in which slender ribs correspond to small N and small ℓ. In summary, the large N and ℓ values in these materials is understandable in the context of the role of bending and torsion of the cell ribs.

2.3.4 Comparison with other experiment

As for comparison with other experiment, prior dense closed cell foams [22], [23] studied experimentally had a relatively small $N = 0.2$, hence comparatively weak size effects. The maximum size effect ratio Ω was 1.3 for dense polyurethane foam and 1.44 for Rohacell foam, much smaller than in the present foams. Foam [23] with comparatively uniform closed cell size had ℓ comparable to the cell size. Foam [22] with substantial heterogeneity of closed cell size had ℓ larger than the cell size. The structures differ considerably from that of the low density open cell foams examined here, which are about one tenth the density of the prior foams. Recently it was shown that classical

continuum theories, such as Bernoulli-Euler beam theory, are inadequate for describing the elastic bending behavior of metal foams [54]. Some cell models were developed for analysis. While such models show the physical origin of the local moments that we interpret via Cosserat elasticity, they have not been couched in such a way to anticipate effects in torsion or changes in strain distribution as is possible with a generalized continuum approach such as Cosserat elasticity. Large characteristic lengths, larger than the cell size are consistent with observations of sigmoid curvature of the lateral surfaces of bent square cross section bars and analysis via Cosserat elasticity [55]. Experimental observation of this sigmoid curvature is consistent too with a large positive value of β/γ. A value β/γ between 0.5 and 1 is sensible based on post-processing of the results of [48], who performed homogenization analysis of a 3-D cubic lattice of straight ribs. No known Cosserat models are available to predict elastic constants for foam.

2.3.5 Asymmetry of the stress

Asymmetry of the stress was inferred from displacement of a notch at the corner of a square cross section bar in torsion. Displacement was observed in foam with 0.4 mm cells but not in rubber which is classical on a macroscopic scale (Figure 2.11). Displacement of the corner notch cannot occur in classically elastic solids because the symmetry of the stress implies stress, hence strain, are zero at the corner. Generalized continuum theories that entail symmetry of the stress also predict zero motion of the notch. The foam exhibits such a displacement in contrast with rubber. So the foam has Cosserat degrees of freedom independent of other freedom associated with generalized continuum theories.

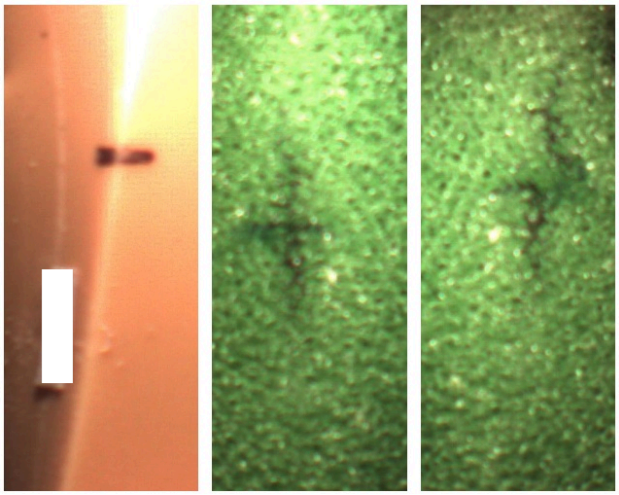

FIGURE 2.11: Corner of rectangular section bars, with notch marked in black ink. Left, twisted rubber; scale bar, 5 mm. Center, foam, 0.4 mm cells, not twisted. Right, foam, 0.4 mm cells, twisted.

2.3.6 Generalized continuum theories

A variety of continuum theories can be used to interpret experiments. We consider it to be sensible to use the simplest one that incorporates known physics of the material and that is consistent with experiment. A substantial material size scale does not guarantee the material exhibits generalized continuum properties. For example a composite containing beads of aluminum in a polymer matrix behaved classically in size effect studies [13]; a syntactic foam containing hollow glass spheres was also essentially classical [22] in contrast to dense polyurethane foam which was Cosserat. The present experimental results show size effects that do not occur in classically elastic materials. They are interpreted in the context of Cosserat elasticity which has more freedom than classical elasticity and allows for size effects. Also, Cosserat elasticity incorporates local rotation and distributed moments. These variables are incorporated in classical analyses [2] of foams in compression to determine moduli; there are no gradients of rotation in that case. As for variants of the Cosserat continuum, the smaller cell foam has a large value of $N = 0.99$. This may be regarded

as consistent with $N = 1$, corresponding the the special case of Cosserat elasticity called couple stress elasticity [12]. The larger cell foam has a smaller N, not consistent with $N = 1$.

As for the possibility of additional freedom, observe that the definitions of characteristic lengths, Eq. 2.6, 2.7 entail a relation between ℓ_t, ℓ_b, and β/γ for isotropic materials. Based on this relation, ℓ_b is larger than expected by a factor of about 2.5. Results do not necessarily exclude the presence of additional freedom such as that incorporated in micromorphic / Mindlin microstructure [7] theory. Micromorphic elasticity includes the freedom of Cosserat elasticity as well as the freedom of the microstructure to deform as well as translate and rotate; it requires 18 elastic constants for an isotropic material. Microstretch elasticity [56] is a subset of microstructure elasticity that incorporates the freedom of Cosserat elasticity as well as sensitivity to gradient of local dilatation. Sensitivity to dilatation gradient of voids [32] when considered alone, gives rise to size effects in bending but not in torsion. Such a theory cannot account for the observed size effects in any of the foams studied, including the present ones. Microstretch elasticity, which includes sensitivity to gradients of rotation and of dilatation could account for bending effects larger than those of Cosserat elasticity. In bending or compression, the dilatational component of deformation can be expected to cause dilation of individual cells, otherwise the bulk modulus would diverge. Indeed, local dilation [57] was observed in cells of metal foam in compression. Theoretical framework is not, however, available to determine dilatation sensitivity independently of rotation sensitivity. A highly simplified plasticity model based on micromorphic theory was used to study stress concentration effects in metal foam [58]. A characteristic length for plasticity was determined. This is in contrast to the present experiments which deal with small strain elasticity and viscoelasticity, and with inference of all the Cosserat elastic constants. As for elasticity, there is no known analytical solution by which to interpret size effects via micromorphic elasticity theory.

Generalized continuum freedom can also be explored via waves. Indeed, dispersion of longitudinal waves and cut-off frequencies were observed in foams of the type studied here [59]. In a micro-structural view, the wave effects were attributed to micro-vibrations of the cell ribs in a structural view. In a generalized continuum view, the effects were associated with microstructure

/ micromorphic elasticity; Cosserat elasticity predicts dispersion of shear waves but not longitudinal waves.

In summary, substantial Cosserat effects do occur in these foams. Effects of dilatation gradient cannot contribute to observed size effects in torsion; they may contribute to size effects in bending. As for the determination of all the 9 elastic constants of a microstretch model or all the 18 constants of a micromorphic model, the requisite exact analytical solutions for interpretation of experiments are not yet available.

2.4 Conclusions

Large size effects are observed in the torsion and bending of reticulated open cell polymer foams. These effects are inconsistent with classical elasticity but can be modeled with Cosserat elasticity.

2.5 Acknowledgements

We gratefully acknowledge support of this research by the National Science Foundation via Grant CMMI-1361832.

Chapter 3

Cosserat elasticity of negative Poisson's ratio foam: experiment

The following chapter has been published:
Z Rueger and R.S. Lakes, "Cosserat elasticity of negative Poisson's ratio foam: experiment", Smart Materials and Structures, **25** (5), (2016).

Abstract Negative Poisson's ratio polymer foams derived from reticulated open cell foams exhibit large size effects in torsion and bending. Effective moduli increase as diameter decreases in contrast to the prediction of classical elasticity. Size effects of this sort are predicted by Cosserat (micropolar) elasticity in which points can rotate as well as translate and distributed moments are incorporated. The Cosserat coupling number N was about twice as large as that of as-received foam, leading to strong effects. The torsion characteristic length ℓ_t was similar. Cosserat effects are known to enhance toughness and immunity from stress concentration.

3.1 Introduction

All physical materials have microstructure, but for many practical purposes it is helpful to represent them as continuous media. Continuum theories with different amounts of freedom are

available. An early theory of Navier [1] was called uniconstant elasticity and was based on a theory that assumed atomic interactions entailed central forces and affine motion of atoms. It allows only one isotropic elastic constant, a modulus. It was abandoned since it predicted a Poisson's ratio of $1/4$ for all isotropic materials; early experiments showed many common materials to have Poisson's ratio between 0.3 and 0.4. The elasticity theory currently accepted as classical allows Poisson's ratios in isotropic materials in the range -1 to $1/2$; there are two independent isotropic elastic constants. The accepted range for Poisson's ratio in isotropic solids was commonly taken as 0 to $1/2$ based on experience with common materials, though some anisotropic single crystals with negative Poisson's ratio were known as well as negative Poisson's ratio in a model of rods, hinges and springs [60]. In 1987 a 3D negative Poisson's ratio material based on transformed open cell polyurethane foam was reported [61]; it had a Poisson's ratio of -0.7. The manufacturing process described in this Science article stimulated much continuing research in the field of designed materials. The negative Poisson's ratio in foams depends on cell structure rather than chemistry; indeed, metallic and thermoset polymer foams have been prepared with negative Poisson's ratio [62]. Negative Poisson's ratio was also designed in 2D systems with rotating hexamers [63] [64]; thermodynamic stability was analyzed. Void space is not required to achieve a negative Poisson's ratio; a hierarchical two phase composite [65] can approach the lower limit -1 provided there is sufficient contrast between constituent properties. Negative Poisson's ratio, also called auxetic in a 1991 article proposing molecular scale design, was analyzed in foams [66]. Negative Poisson's ratio can be achieved in other 2D structures containing rotating rigid units such as squares [67]. In all these examples, the material has been considered to be classically elastic. Initial evidence of non-classical characteristics was revealed by holography in non-affine heterogeneous deformation of conventional and negative Poisson's ratio copper foams [68] and in size effects in negative Poisson's ratio polymer foam [69].

Classical elasticity has no length scale. By contrast, Cosserat elasticity [3] [30], also called micropolar elasticity [9], allows rotations of points and has a length scale, so it is pertinent to the deformation of heterogeneous materials in which the heterogeneity size scale cannot be neglected

in comparison to dimensions of a structural component or of structural heterogeneities such as holes or cracks. Soon after the initial article on negative Poisson's ratio foam, it was suggested that the effect was due to the coarse cell structure and Cosserat effects in the associated continuum view. However Poisson's ratio is a classical concept; moreover the range of Poisson's ratio for Cosserat solids is the same as the range for classical ones: -1 to $1/2$. Too, the simple tension experiment used to reveal Poisson's ratio has no associated length scale and does not excite the rotational degrees of freedom required to produce non-classical effects in a Cosserat elastic material [61]. Foams and honeycombs, though they can have substantial cell sizes, are commonly treated as classical continua [70]. Only toughness of foams is related to the size scale of the cells [70]; the treatment is nonetheless classical. Cosserat elastic solids, if isotropic, have six elastic constants. Deviations from classical elasticity have long been known. For example, Brillouin [71] studied wave propagation in crystal lattices; a spring mass model discloses dispersion of waves, in harmony with experimental observations of high frequency ultrasonic waves in crystals. Dispersion and cut off frequency effects can be modeled from a continuum perspective. For example, the microstructure elasticity theory of Mindlin [7], allows points in the continuum to translate, rotate, and deform. Such a theory, also called micromorphic, is more complex than classical or Cosserat elasticity; for an isotropic solid, there are 18 micromorphic elastic constants compared with 6 for Cosserat elasticity and 2 for classical elasticity. The allowable range of Poisson's ratio in microstructure elasticity is not stated directly. However, energy based limits for tensorial constants in microstructure elasticity imply a range of Poisson's ratio equivalent to that in classical elasticity. Microstretch elasticity is also a subset of microstructure / micromorphic elasticity, one that incorporates the Cosserat type freedom as well as sensitivity to dilatation gradient [56]. There are 9 isotropic elastic constants. As with microstructure elasticity, allowable range of Poisson's ratio in is not stated directly. However, energy based limits for tensorial constants suggest a range of Poisson's ratio equivalent to that in classical elasticity.

The physical origin [72] of the Cosserat couple stress in cellular solids is the summation of bending and twisting moments transmitted by ribs in a foam or by structural elements in other

materials (Figure 3.1). The local rotation in the Cosserat continuum corresponds to the rotation of ribs. Forces and moments are also considered in the classic analyses of foam by Gibson and Ashby [70] in which classical elastic moduli were determined; effects of rotation gradients were not considered.

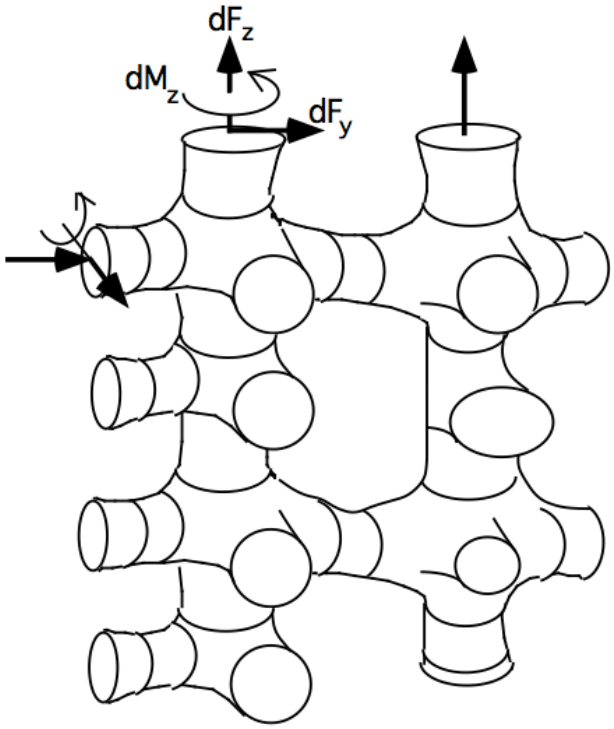

FIGURE 3.1: Ribs of foam or lattice with increment of force dF and increment of moment dM.

The Cosserat theory of elasticity is a continuum theory that incorporates a specific kind of nonlocal [31] interaction. The stress σ_{jk} (force per unit area) can be asymmetric. The moment arising from this asymmetry is balanced by a couple stress m_{jk} (a torque per unit area). The antisymmetric part of the stress is related to local rotations. $\sigma_{jk}^{antisym} = \kappa e_{jkm}(r_m - \phi_m)$ in which κ is an elastic constant, ϕ_m is the rotation of points, called micro-rotation, e_{jkm} is the permutation symbol, and $r_k = \frac{1}{2}e_{klm}u_{m,l}$ is the “macro" rotation based on the antisymmetric part of gradient of displacement u_i. The constitutive equations [9] for linear isotropic Cosserat elasticity are as

follows.

$$\sigma_{ij} = 2G\epsilon_{ij} + \lambda\epsilon_{kk}\delta_{ij} + \kappa e_{ijk}(r_k - \phi_k) \tag{3.1}$$

$$m_{ij} = \alpha\phi_{k,k}\delta_{ij} + \beta\phi_{i,j} + \gamma\phi_{j,i} \tag{3.2}$$

Cosserat elasticity allows sensitivity to gradients of rotation because rotations and stresses are coupled. One may also formulate a generalized continuum theory with sensitivity to gradients of dilatation [32] rather than rotation.

There are six independent isotropic Cosserat elastic constants λ, G, α, β, γ, κ. The following technical constants, beneficial for physical insight, are obtained from them. As in classical elasticity, several are interrelated; specifically of the seven below, the classical relation between E, G and ν applies. Here λ is a Lamé constant from elasticity theory.

$$Young's\ modulus \qquad E = \frac{G(3\lambda + 2G)}{\lambda + G} \tag{3.3}$$

$$Shear\ modulus \qquad G \tag{3.4}$$

$$Poisson's\ ratio \qquad \nu = \frac{\lambda}{2(\lambda + G)} \tag{3.5}$$

$$Characteristic\ length,\ torsion \qquad \ell_t = \sqrt{\frac{\beta + \gamma}{2G}} \tag{3.6}$$

$$Characteristic\ length,\ bending \qquad \ell_b = \sqrt{\frac{\gamma}{4G}} \tag{3.7}$$

$$Coupling\ number \qquad N = \sqrt{\frac{\kappa}{2G + \kappa}} \tag{3.8}$$

$$Polar\ ratio \qquad \Psi = \frac{\beta + \gamma}{\alpha + \beta + \gamma} \tag{3.9}$$

Predictions of Cosserat elasticity differ from those of classical elasticity. A size effect is predicted in the torsion [13] and bending [14] of circular cylinders of Cosserat elastic materials. Thin

cylinders appear more stiff than expected classically. A size effect is also predicted in the bending of plates [13] . In tension or compression there is no size effect. The stress concentration factor for a circular hole is smaller than the classical value; small holes exhibit less stress concentration than larger ones [15].In classical elastic solids, by contrast, there is no size effect in torsion or bending; structural rigidity goes as the fourth power of the radius; stress concentration is independent of hole size.

Cosserat elastic effects have been observed experimentally in several materials with microstructure. Size effects which occur in torsion and bending of closed cell foams [22], [23] and of compact bone [21] are consistent with Cosserat elasticity. The apparent modulus increases substantially as the specimen diameter becomes smaller. This observation is in contrast to the predictions of classical elasticity. Cosserat elasticity can account for these observations. Dense (340 $\mathrm{kg/m^3}$) closed cell polyurethane foam [22] has elastic constants E = 300 MPa, G = 104 MPa, ν = 0.4, ℓ_t = 0.62 mm, ℓ_b = 0.33 mm, N^2 = 0.04, Ψ = 1.5. The cell size is from 0.05 mm to 0.15 mm. For dense (380 $\mathrm{kg/m^3}$) polymethacrylamide closed cell foam (Rohacell WF300) [23], E = 637 MPa, G = 285 MPa, ℓ_t = 0.8 mm, ℓ_b = 0.77 mm, $N^2 \approx 0.04$, Ψ = 1.5. The cell size is about 0.65 mm.

The Cosserat characteristic length was determined for a two dimensional polymer honeycomb [33]. Warp of a bar of rectangular cross section in torsion is predicted to be reduced in a Cosserat elastic solid [34]. Such non-classical warp was observed in compact bone [35]. Deformation spills over into the corner region where it would be zero in classical elasticity [36] as revealed by holography. This ameliorates concentration of strain. Strain at the corner entails asymmetry of the stress as predicted by Cosserat elasticity. The reduction of warp deformation has been observed via holography [37]. Cosserat effects were also observed in open cell polymer foam [73].

The present research deals with experimental study of size effects and Cosserat elasticity in negative Poisson's ratio foams derived from low density open cell polymer foams.

3.2 Methods

3.2.1 Materials and experiment

Negative Poisson's ratio foam (Figure 3.3) based on reticulated polyurethane foam (Scott Industrial foam [39]) was used. The as-received foam had average cell size 1.2 mm or 20 pores per inch. The initial density was 30 kg/m^3. The foam was converted to negative Poisson's ratio foam via triaxial compression and heat treatment [61]. The density calculated for the foam was 96 kg/m^3 corresponding to a volumetric compression ratio of 3.2.

Cylinders were cut from polymer foam with a hot wire cutter such that the cylinder diameter and length were equal. The wire was Nichrome heater wire of thickness 0.015 inches and resistance 2.5 Ω. The electric current was 3 Amps. The initial cylinder cut from the foam was approximately 22 mm in both diameter and length. The foam cylinder was weighed with an analytical balance. Circular end pieces the same diameter as the foam sample were cut from heavy card stock and cemented to both bases of the cylindrical specimen using cyanoacrylate (Loctite 401) over the entire surface. A catalyst was applied to the surfaces being cemented to minimize the amount of cement used and prevent ingression of the cement into the pores of the foam. Slight pressure was applied to the end pieces to ensure good adhesion.

These specimens were tested for torsional and bending rigidity using a Broadband Viscoelastic Spectrometer (BVS) [40] [41]. This instrument uses a Helmholtz coil which acts upon a magnet attached to the specimen to generate torque. The coil spacing is smaller than the larger specimens so a short stalk with a magnet and mirror on the end was fixed to one of the end pieces. A thin aluminum end layer was also cemented to provide a sufficiently rigid attachment for the stalk. A small mirror was first glued to one face of a cubic magnet. The magnet was then calibrated using the BVS and a lock-in amplifier. The magnetic calibration constants of this magnet were obtained by testing a 6061 aluminum alloy rod of known elastic properties. The calibration constants were 8.00 $\times 10^{-6}$ Nm/A in torsion and 1.84 $\times 10^{-5}$ Nm/A in bending. The free end piece of the polymer foam cylinder was cemented to a steel adapter which was screwed in to a 25 mm thick steel rod to

support the specimen inside the BVS. Viscoelastic strain was allowed to recover overnight prior to testing to enable stable measurements. The specimen was lowered into the BVS such that the magnet was centered in the Helmholtz coils of the BVS. The lower limit on specimen size was imposed by obtrusive presence of incomplete cells; also by difficulty in handling. A typical specimen of this foam is shown in Figure 3.2.

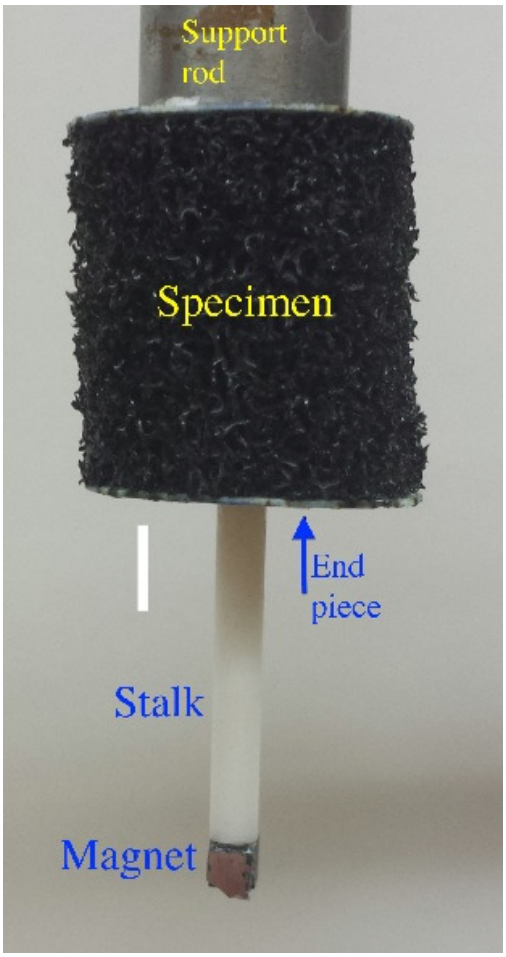

FIGURE 3.2: A specimen of foam with attached stalk and magnet. White scale bar: 5mm.

Deformation was measured via a beam from a semiconductor laser reflected from a mirror attached to the magnet on the specimen free end. The laser beam was reflected onto a silicon

light detector.The laser based displacement sensor was calibrated prior to testing. This was done by first centering the beam upon the detector. The light detector was moved a known amount via a calibrated stage. A calibration curve was obtained via micrometer adjustment. The change in output voltage per change in position was used as the beam position calibration constant (in $V/\mu m$).

A sinusoidal signal with a frequency of 1 Hz from a function generator (SRS Model DS345) was input to the torsion Helmholtz coil to test the sample. Because the same frequency was used for all specimen diameters, viscoelastic effects are decoupled from the size effects to be studied. The torque signal was obtained as the voltage across a resistor in series with the coil to eliminate effects of inductive reactance from the coil. The 1 Hz frequency was well below any resonant frequencies. The torque signal vs. angular displacement signal was displayed on a digital oscilloscope (Tektronix TDS3014B) using DC coupling as a Lissajous figure, and used to calculate the modulus and viscoelastic damping of the material.

For bending, the light detector mode was switched to vertical detection and the beam calibration constant was determined accordingly. The driving signal to generate torque was input to the orthogonal bending Helmholtz coil. A correction was applied to account for the additional bending moment imposed by the weight of the magnet and stalk; this correction was 4% or less.

Compression tests were done to ascertain the behavior of the foam in the absence of macroscopic gradients of strain and rotation. This was done by gluing one end piece to a base anchored to an optical table. Force was applied via dead weights placed on the top end piece. Deformation was measured using a linear variable differential transformer (LVDT); its stem was cemented to the top end piece. The LVDT was calibrated using a micrometer driven translation stage. The maximum strain achieved was 4.4%, well within the linear range for a flexible foam. A lower limit on specimen size was imposed by the tendency of small specimens to buckle.

After all testing was completed on a sample it was cut to a smaller length and diameter and the same series of tests were conducted. This process was repeated for a total of ten sample sizes down to a diameter of 3.4 mm. The lower limit on specimen size was imposed by incomplete cells

and difficulty in handling.

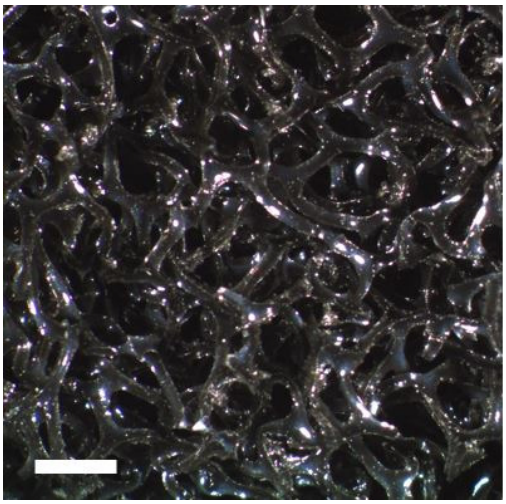

FIGURE 3.3: Structure of negative Poisson's ratio foam. Reflected light micrograph. Scale bar: 1 mm.

3.2.2 Analysis and interpretation

Size effect results were interpreted using available exact analytical solutions for torsion and bending of a Cosserat elastic solid. The shear modulus G was found from the asymptote of torsion rigidity vs. diameter curve for large size. The torsion characteristic length ℓ_t was found from fitting the points for the larger specimens to an approximate solution that is asymptotically valid for large size. A Cosserat elastic circular rod of radius r exhibits the following ratio of structural rigidity to its classical counterpart (in the absence of gradient, for large diameter).

$$\Omega \approx 1 + 6(\ell_t/r)^2. \tag{3.10}$$

Size effects occur in torsion: slender specimens appear to have a higher effective modulus than thick ones. The classical torsional rigidity is $\frac{M}{\theta} = G[\frac{\pi}{2}r^4]$. For Cosserat elasticity in this regime, $\frac{M}{\theta} = G[\frac{\pi}{2}r^4](1 + 6(\ell_t/r)^2)$. G is the true shear modulus in the absence of gradients; M is applied moment and θ is angular displacement. This expression is exact for N = 1; for other N the exact

solution involves Bessel functions [13]:

$$\Omega = (1 + 6(\ell_t/r)^2)[\frac{(1 - 4\Psi\chi/3)}{1 - \Psi\chi}], \tag{3.11}$$

in which $\chi = I_1(pr)/prI_0(pr)$, $p^2 = 2\kappa/(\alpha + \beta + \gamma)$ and I_0 and I_1 are modified Bessel functions of the first kind.

The shear modulus G and characteristic length ℓ_t were determined by fitting experimental data for the three largest specimens to Eq. 3.10. The value of N was found by fitting Eq. 7.10 to the full data set using MATLAB. The constant Ψ only has an appreciable influence for very small radius specimens.

For bending, the classical bending rigidity is $\frac{M}{\theta} = E[\frac{\pi}{4}r^4]$. For bending of a Cosserat elastic circular rod and radius r, the rigidity ratio for small characteristic length $\ell_b << r$ is

$$\Omega \approx 1 + 8(\ell_b/r)^2 \frac{(1 - (\beta/\gamma)^2)}{(1 + \nu)}. \tag{3.12}$$

This expression is exact if $\beta/\gamma = -\nu$. The Young's modulus E and an initial value for the characteristic length ℓ_b were determined by fitting data for the three largest specimens to Eq. 3.12, with N input from the torsion analysis, and an initial value β/γ = 0.8 based on prior experimental results on other foams and ν from prior experimental results on negative Poisson's ratio foams.

Finally the values of ℓ_b and β/γ were found by fitting the bending exact solution [14] Eq. 7.11 to the full data set using MATLAB.

$$\Omega = 1 + 8(\ell_b/r)^2 \frac{(1 - (\beta/\gamma)^2)}{(1 + \nu)} + \frac{8N^2}{(1 + \nu)}[\frac{(\beta/\gamma + \nu)^2}{\zeta(\delta a) + 8N^2(1 - \nu)}] \tag{3.13}$$

with $\delta = N/\ell_b$ and $\zeta(\delta r) = (\delta r)^2[((\delta r)I_0((\delta r)) - I_1((\delta r)))/((\delta r)I_0(\delta r) - 2I_1(\delta r))]$.

3.3 Results and discussion

Density of foam specimens was 96 kg/m^3 and was independent of specimen diameter to within a few percent. As for tests of anisotropy, the as-received foam was anisotropic [73], with a ratio of compressive moduli in different directions of 1.6.

Results of torsion size effect studies are shown in Figure 3.4.

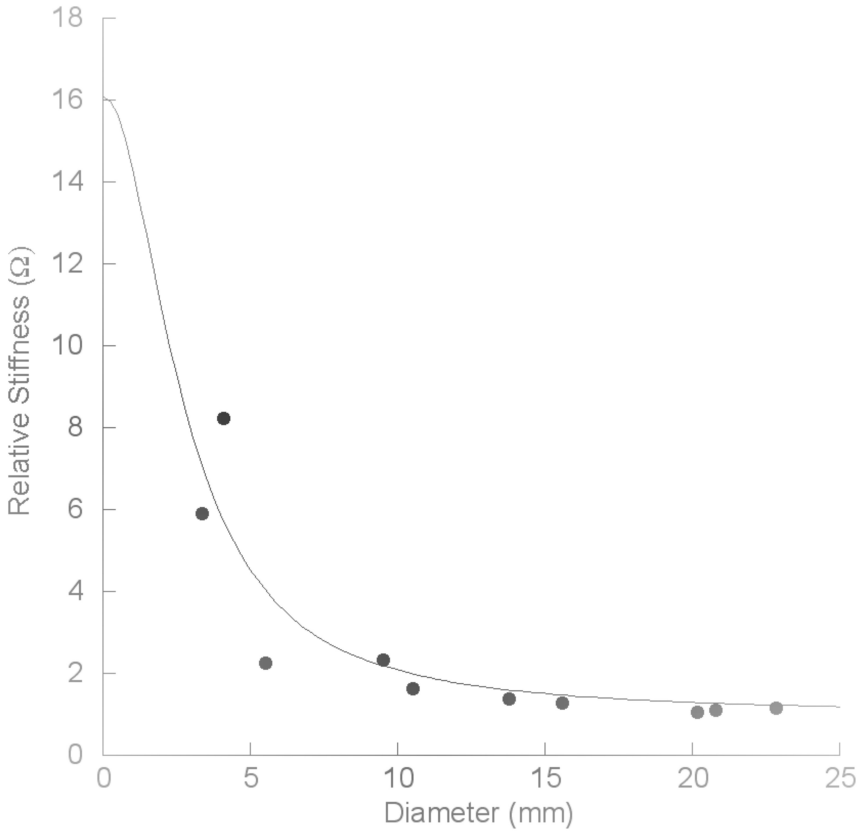

FIGURE 3.4: Size effects for negative Poisson's ratio foam in torsion. Points are experimental. Curve is theoretical for G = 16 kPa, ℓ_t = 2.3 mm N = 0.78 and Ψ = 1.5. Classical elasticity predicts constant Ω = 1 independent of diameter.

For negative Poisson's ratio foam, G = 16 kPa, ℓ_t = 2.3 mm N = 0.78 and Ψ = 1.5.

By contrast, the as-received foam [73] had G = 45 kPa and the characteristic length for torsion was ℓ_t = 2.1 mm. Moreover N = 0.41, and Ψ = 1.5. So the negative Poisson's ratio foam had N

about twice as large as that of as-received foam and ℓ_t was similar. The goodness of fit was R^2 = 0.79. The maximum size effect in torsion for as-received foam was Ω = 2.2. The larger maximum size effect, about 8 in negative Poisson's ratio foam, is associated with the larger coupling number N.

The compression tests disclosed E = 25 kPa with no consistent dependence on diameter. Results of bending size effect studies are shown in Figure 3.5. Assuming E = 25 kPa based on compression and N = 0.78 based on torsion, the best fit for the remaining constants for negative Poisson's ratio foam was ℓ_b = 3.9 mm, $\beta/\gamma = 0.8$, with goodness of fit R^2 = 0.81. If however one ignores the compression result and conducts a fit, the result is E = 38 kPa, ℓ_b = 3.0 mm, $\beta/\gamma = 0.87$, with goodness of fit R^2 = 0.81. Also, the asymptote for large size in the bending studies would be better delineated if larger specimens were available, however the processing used to obtain negative Poisson's ratio foam resulted in rectangular bars about 25 mm in square cross section. The bars as received foam were about twice as wide, and were cut to appropriate width to obtain the correct volumetric compression. For this material, bending of the largest specimens resulted in a better value of E. The range of values that are tolerable to the fitting process is attributed to the scatter in the data points and to the accessible range in specimen diameter. As for the range in ℓ_b for bending, values between about 3 mm to 4.7 mm gave $R^2 > 0.6$ in contrast to R^2 = 0.81 for the best fit ℓ_b = 3.9 mm. As for the range of N, values between 0.62 and 9 gave $R^2 > 0.6$ in contrast to R^2 = 0.81 for the best fit N = 0.78.

By contrast, the as-received foam [73] had E = 91 kPa, ℓ_b = 9 mm, $\beta/\gamma = 0.83$; N = 0.41. The maximum size effect for as-received foam in bending was Ω = 3. As with torsion, the negative Poisson's ratio foam exhibited a much larger size effect ratio Ω = 18, attributed to the larger N.

The Poisson's ratio of the as-received foam was determined [42] to be approximately 0.3. This value was also given by [70] as the mean of measurements by various authors on different foams of conventional structure. The Poisson's ratio of the negative Poisson's ratio foam was inferred to be -0.63 based on the initial and final density [74]. Specimens were sufficiently short that direct measurement of Poisson's ratio was not practical. Nevertheless, stretching of thin slices revealed

the Poisson's ratio to be negative. The relationship between moduli and Poisson's ratio implies anisotropy. That is not surprising in view of the modest anisotropy of the as received foam. It is possible to make fully isotropic negative Poisson's ratio foam [75] via further effort in processing.

It is of interest to compare the inferred characteristic lengths with the foam cell size. The as-received foam had an average cell size of 1.2 mm. Volumetric compression by a factor of 3.2 to produce the negative Poisson's ratio foam reduces the cell size and also causes the folded-in re-entrant structure that gives rise to the negative Poisson's ratio. The effective cell size may be taken as 1.2 mm / $3.2^{1/3}$ = 0.81 mm. Both characteristic lengths are considerably larger than this, a fact attributed to the bend dominated role of the foam ribs.

As for other foams as Cosserat solids, experiments on dense closed cell foams [22], [23] revealed a relatively small N = 0.2, so size effects were comparatively weak. The maximum size effect ratio was Ω = 1.3 for dense polyurethane foam and 1.44 for closed cell Rohacell foam, much smaller than in the present foams. Foam [23] with relatively uniform cell size had ℓ comparable to the cell size. Foam [22] heterogeneous in its cell size had ℓ larger than the cell size. The structures, as well as the structure of the as received foam, differ considerably from that of the negative Poisson's ratio re-entrant foams examined here.

Damping tan δ of the foam was essentially independent of specimen size, as shown in Figure 3.6 but the two smallest sizes showed a somewhat higher damping. tan δ was similar to that of as-received foam suggesting no obvious change in cross link density or other molecular aspects as a result of the processing used to obtain negative Poisson's ratio foam. By contrast, a dependence of modulus and damping on processing [76] was observed in which damping increased statistically with permanent compression hence with the reduction in Poisson's ratio. Both these polyurethane foams were prepared via triaxial compression followed by heat treatment [61]. One can also prepare auxetic foam and revert it to a positive Poisson's ratio via a solvent treatment [77]. The influence of processing procedure on structure and properties has been analyzed [78].

Scatter in the data points is attributed to incomplete cells at the specimen surface, also to larger scale heterogeneity in the foam. Similar scatter was observed in the as-received foam.

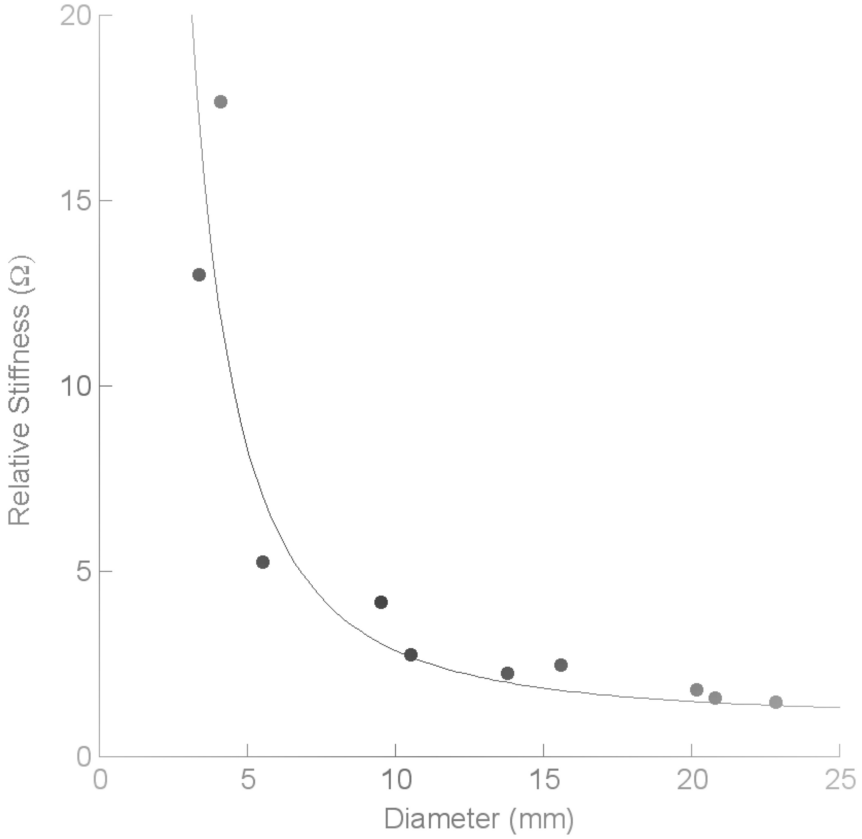

FIGURE 3.5: Size effects for negative Poisson's ratio foam in bending. Points are experimental. Curve is theoretical for E = 25 kPa N = 0.78, ℓ_b = 3.9 mm, and $\beta/\gamma = 0.88$. Classical elasticity predicts constant Ω = 1 independent of diameter.

As for comparison with theory, no known analysis is available for the structure of the present foam. Cosserat elastic constants have been calculated from theoretical homogenization of several lattices with straight ribs [47] [48] [49]. These are stretch dominated so the effects of rib bending and torsion are much smaller than the effects of rib extension. The characteristic lengths of such lattices are much smaller than the cell size. Two dimensional chiral honeycomb lattice structures analyzed as Cosserat continua disclosed bend dominated behavior in which Young's modulus is governed by rib bending. These honeycombs have large N approaching its upper bound 1, and characteristic length ℓ comparable to the cell size [50]. Sigmoid curvature of the lateral surfaces of

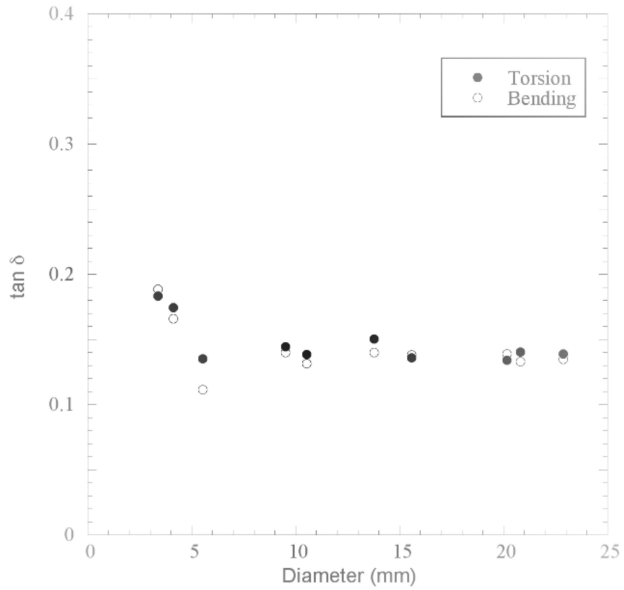

FIGURE 3.6: Viscoelastic tan δ vs. specimen size for negative Poisson's ratio foam. Open circles: bending. Solid circles: torsion.

bent square cross section bars was analyzed via Cosserat elasticity [55]. Such curvature requires $\beta/\gamma \neq -\nu$ and indeed it was observed in conventional as-received open cell foam. Although no formal measurements were made with the negative Poisson's ratio foam (for which $\beta/\gamma \approx -\nu$), visual observation of such bending of a square cross section bar suggested any sigmoid curvature must be small.

In summary, large size effects are observed in the torsion of negative Poisson's ratio open cell foam. The effects are consistent with Cosserat elasticity. Results do not necessarily exclude the presence of additional freedom such as that incorporated in micromorphic / Mindlin microstructure [7] theory or in microstretch elasticity [56].

3.4 Conclusions

Large size effects were observed in the torsion and bending of negative Poisson's ratio open cell polymer foams. These effects are inconsistent with classical elasticity but can be modeled with

Cosserat elasticity. The negative Poisson's ratio foam had Cosserat coupling number N about twice as large as that of as-received foam; torsion characteristic length ℓ_t was similar, and bending characteristic length ℓ_b was smaller. Maximum size effects were larger than those in as-received foam. This is attributed to the larger N. Cosserat solids are known to exhibit enhancement in toughness and immunity from stress concentrations, a beneficial characteristic.

3.5 Acknowledgements

We gratefully acknowledge support of this research by the National Science Foundation via Grant CMMI-1361832.

Chapter 4

Strong Cosserat elastic effects in a unidirectional composite

The following chapter has been published:
Z Rueger and R.S. Lakes, "Strong Cosserat elastic effects in a unidirectional composite", Z. Angew. Math. Phys., **68** (54), (2017).

Abstract Strong Cosserat elastic effects are observed in a designed composite consisting of unidirectional corrugated tubes in a hexagonal array. The torsional characteristic length is much larger than the tube diameter. The effective coupling number N approaches its upper bound of 1. Extremely large size effects are observed, about a factor of 128 in torsion.

4.1 Introduction

All physical materials have microstructure, but for many practical purposes it is useful to represent them as continuous media. Continuum theories with different degrees of freedom are available. An early theory of Navier [1], known as uniconstant elasticity, was based on a a theory assuming that forces act along the lines joining pairs of atoms and are proportional to changes in distance between them. It only allowed one elastic constant, a modulus. The theory was abandoned since it predicted a Poisson's ratio of $1/4$ for all isotropic materials and experiments disclosed a range of

Poisson's ratios. The currently accepted classical theory of elasticity has two independent isotropic elastic constants and allows for Poisson's ratios in isotropic materials to range from -1 to 1/2. Cosserat elasticity has more freedom than classical elasticity. The Cosserat theory [3], (with inertia terms called micropolar [9]) incorporates local rotations of points and a couple stress (a torque per unit area) as well as the translation and force stress (force per unit area) of classical elasticity; there are six independent isotropic elastic constants. A simpler variant presented by Koiter assumed that all the macrorotation and microrotation vectors are equal. This corresponds to $N = 1$, or equivalently κ approaching infinity in Cosserat elasticity. The Koiter [12] variant is called couple stress elasticity in which there are two characteristic lengths in addition to the classical constants: four isotropic elastic constants. The microstructure elasticity theory of Mindlin [7], also called micromorphic elasticity, has more freedom than classical or Cosserat elasticity; it allows points to translate, rotate, and deform within the media. This adds a high degree of complexity; for an isotropic solid, there are 18 micromorphic elastic constants compared with 6 for Cosserat elasticity and only 2 for classical elasticity.

The physical origin of the Cosserat couple stress is the summation of bending and twisting moments transmitted by the structural elements or ribs in materials. The local rotation in the Cosserat continuum corresponds to the rotation of the structural elements. Forces and moments are also considered in the classic analyses of foam by Gibson and Ashby [2] in which classical elastic moduli were determined; effects of rotation gradients were not considered.

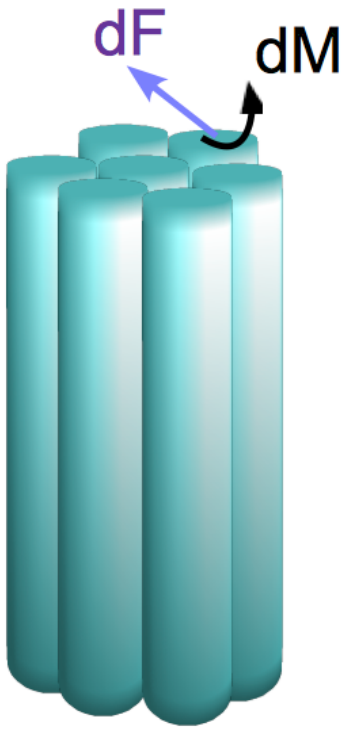

FIGURE 4.1: Composite containing unidirectional tubular inclusions with increment of force *dF* and increment of moment *dM*.

The constitutive equations for an anisotropic [9] Cosserat elastic solid are as follows.

$$\sigma_{ij} = C_{ijkl}\epsilon_{kl} + P_{ijkl}\phi_{k,l}, \tag{4.1}$$

$$m_{ij} = Q_{ijkl}\phi_{k,l} + P_{ijkl}\epsilon_{kl}, \tag{4.2}$$

in which C_{ijkl} is the elastic modulus tensor, ϵ_{kl} is strain, σ_{ij} is stress (symmetric in classical elasticity but asymmetric here), and the usual Einstein summation convention assumed in which repeated indices are summed over. m_{ij} is the couple stress tensor, moment per unit area, asymmetric in general. P_{ijkl} and Q_{ijkl} are Cosserat elastic constants that provide sensitivity to local (micro)

rotation gradient. The Cosserat microrotation vector ϕ_i is kinematically distinct from the macro-rotation vector $r_i = (e_{ijk}u_{k,j})/2$ associated with the motion of neighboring points.

The isotropic form [9] of the constitutive equations is as follows.

$$\sigma_{ij} = 2G\epsilon_{ij} + \lambda\epsilon_{kk}\delta_{ij} + \kappa e_{ijk}(r_k - \phi_k) \tag{4.3}$$

$$m_{ij} = \alpha\phi_{k,k}\delta_{ij} + \beta\phi_{i,j} + \gamma\phi_{j,i} \tag{4.4}$$

There are six independent isotropic Cosserat elastic constants λ, G, α, β, γ, κ. Physically, λ, a Lamé constant from elasticity theory, is an elastic modulus component which couples a strain in one direction with stress in a perpendicular direction with all other strains held constant. The physical meaning of G, shear modulus, is the resistance to shear deformation. α, β, and γ provide sensitivity to rotation gradients while κ is a modulus which quantifies the coupling between macro and micro rotation fields [79]. The following technical constants, beneficial for physical insight, are obtained from them. As in classical elasticity, several are interrelated; specifically of the seven below, the classical relation between E, G and ν applies.

$$Young's\ modulus \qquad E = \frac{G(3\lambda + 2G)}{\lambda + G} \tag{4.5}$$

$$Shear\ modulus \qquad G \tag{4.6}$$

$$Poisson's\ ratio \qquad \nu = \frac{\lambda}{2(\lambda + G)} \tag{4.7}$$

$$Characteristic\ length,\ torsion \qquad \ell_t = \sqrt{\frac{\beta + \gamma}{2G}} \tag{4.8}$$

$$Characteristic\ length,\ bending \qquad \ell_b = \sqrt{\frac{\gamma}{4G}} \tag{4.9}$$

$$Coupling\ number \qquad N = \sqrt{\frac{\kappa}{2G + \kappa}} \tag{4.10}$$

$$Polar\ ratio \qquad \Psi = \frac{\beta + \gamma}{\alpha + \beta + \gamma}. \tag{4.11}$$

Cosserat elasticity has the following consequences. A size effect is predicted in the torsion [13] and bending [14] of circular cylinders of Cosserat elastic materials. Slender cylinders appear to be stiffer than expected classically. A similar size effect is also predicted in the bending of plates. No size effect is predicted in tension or compression. The stress concentration factor for a circular hole is smaller than the classical value, and the small holes exhibit less stress concentration than larger ones [15]. However, classical elastic solids do not exhibit size effects in torsion or bending; structural rigidity goes as the fourth power of the radius. Also, in classical elasticity, stress concentration is independent of hole size.

Cosserat elastic effects have been observed experimentally. Size effects observed to occur in torsion and bending of closed cell foams [22, 23], open cell foam [73], negative Poisson's ratio foam [80], and compact bone [21] are consistent with Cosserat elasticity. The apparent modulus increases substantially as the specimen diameter becomes smaller, in contrast to the prediction of classical elasticity. Large material microstructure size does not guarantee Cosserat elasticity: a composite containing aluminum beads in an epoxy matrix was tested for such effects and found to behave according to classical elasticity [13]. Although Cosserat effects are not guaranteed in materials with large microstructure, the work presented here will demonstrate that these materials can demonstrate the aforementioned effects.

The Cosserat characteristic length was determined in a two dimensional polymer honeycomb [33]. Full field measurements of deformation reveal non-classical elastic effects that are consistent with Cosserat elasticity. Warp of a bar of rectangular cross section in torsion is predicted to be reduced in a Cosserat elastic solid [34]. The corresponding non-classical strain field was observed in a compact bone [35]. Deformation spills over into the corner region where it would be zero in classical elasticity [36] as revealed by holography. This improves strain concentration. Strain at the corner entails asymmetry of the stress as predicted by Cosserat elasticity. The reduction of warp deformation has been observed via holography [37]. As for plastic deformation, rotational plastic deformation mechanisms were interpreted via gradients in a micropolar continuum theory [38].

The present research deals with experimental study of size effects and Cosserat elasticity in a designed composite consisting of unidirectional corrugated tubes and silicone rubber matrix in hexagonal arrays. Each tube is intended to carry a force and a moment as shown in Figure 4.1.

4.2 Methods

4.2.1 Materials and experiment

Corrugated nylon tubing, manufactured by Waytek [81], with inner diameter of 3.18 mm (0.125 in), outer diameter of 6.7 mm, and density of approximately 0.26 $\mathrm{g/cm^3}$ was used. Lengths of tubing were cut with a hot wire cutter such that the length of the array of tubes was three times longer than the average diameter of the sample. The corrugated tubing came coiled and was straightened by running a brass tube with an outer diameter of approximately 3 mm through 20 cm lengths of the tubing and heating it in a convection oven at 105°C for two hours. After two hours the straightening apparatus was removed and allowed to cool for 15 minutes before removing the straightened section of corrugated tubing. Four samples were created and tested beginning with a single tube, followed by an array of three tubes arranged in a triangular formation, then seven tubes arranged in a hexagonal pattern, and finally 19 tubes again arranged in a hexagonal formation. The largest of these specimens is shown in Figure 4.2a as well as its hexagonal array cross-section, Figure 4.2b. Because the broadband viscoelastic spectrometer (BVS) used for testing could not accommodate larger specimens than the one in Figure 4.2a, the number of specimens was limited to four. The lengths of tubing were glued together with approximately 1 mm spacing between each tube using Loctite clear silicone sealant. The entire sample was allowed to cure for two days per product directions prior to testing. The resulting specimens had an average density of $0.46 \pm 0.07 \mathrm{g/cm^3}$. After curing, the ends of the samples were sanded flat using metallography sanding wheels. Circular end pieces larger than the diameter of the sample were cut from 0.6 mm thick aluminum plate and cemented to both bases of the sample using cyanoacrylate (Loctite 401)

over the entire surface. Pressure was applied to the end pieces to ensure good adhesion. A catalyst was applied to the surfaces to reduce the amount of cement used and to improve the bond.

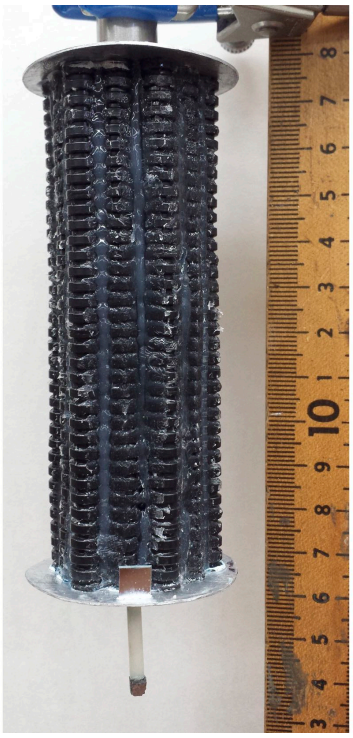

(A) Largest specimen.

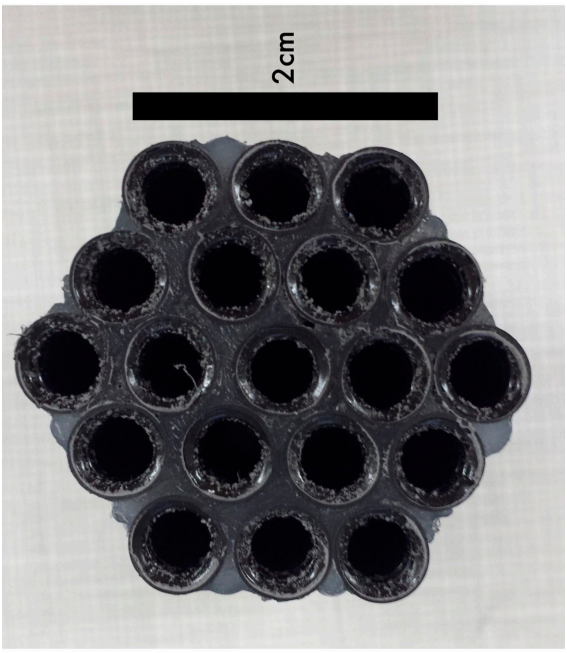

(B) Cross section of largest sample.

FIGURE 4.2: Views of aligned corrugated tubing and silicone rubber matrix composite.

These specimens were tested for torsional and bending rigidity using a broadband viscoelastic spectrometer (BVS). This instrument makes use of a dual Helmholtz coil acting upon a magnet attached to the specimen to generate torque. The coil spacing is smaller than the larger specimens so a short alumina stalk with a magnet on the end was fixed to one of the aluminum end plates. Because the rigidity of the specimens was not sufficiently different from the rigidities of the alumina stalk or cement bond between stalk and end plate, a mirror was fixed to the edge of the face opposite of the alumina stalk on the same end plate. This placement eliminated any measured loss of motion from the magnet to the specimen. The magnet was calibrated using the BVS and

a lock-in amplifier. The magnetic calibration constants of this particular magnet were obtained by testing a 6061 aluminum alloy rod of known elastic properties; the calibration constants were $8.18 * 10^{-6}$ Nm/A in torsion and $1.33 * 10^{-5}$ Nm/A in bending. The free end plate of specimens was cemented to a steel adapter which was screwed into a 25 mm thick steel rod for holding the specimen inside the BVS. Prior to testing, viscoelastic strain was allowed to recover overnight to enable stable measurements. The specimen was lowered into the BVS such that the magnet was centered in the Helmholtz coils of the BVS. The lower limit on specimen size was limited to the diameter of an individual corrugated tube.

Deformation was measured using the BVS via a semiconductor laser beam reflected from the mirror attached to the lower aluminum end plate onto a four quadrant silicon light detector. Prior to each test the silicon light detector was calibrated by aligning the laser beam so that its position could be measured. The light detector was moved a known amount in either the horizontal or vertical direction, for torsion and bending respectively, using a calibrated stage. The resulting measurement of output voltage per change in position, measured in μm, was used as the beam position calibration constant (V/μm).

To test the specimens a sinusoidal signal with a frequency of 1 Hz, well below any resonant frequencies, from a function generator (SRS Model DS345) was input to the torsion Helmholtz coil. Because the same frequency was used for all specimens, viscoelastic effects are decoupled from the size effects to be probed. The torque signal was obtained as the voltage across a 1Ω resistor in series with the coil to eliminate effects of inductive reactance from the coil. The torque signal vs. angular displacement signal was displayed on a digital oscilloscope (Tektronix TDS3014B) using DC coupling. The torque and angle signals were displayed as a Lissajous figure and used to calculate the modulus of the specimen. The maximum strain during testing was less than $1.1 * 10^{-7}$. This is will within the range of linearity for this material. For bending, the light detector mode was switched to vertical detection and the beam position calibration constant was adjusted accordingly; the driving signal was input to the orthogonal bending Helmholtz coil.

Compression tests were conducted to ascertain the behavior of the largest specimen in the

absence of macroscopic gradients of strain and rotation. This was done using a servo-hydraulic load frame driven at a sinusoidal frequency of 1 Hz. The output stress and strain signals were displayed on a digital oscilloscope as a Lissajous figure so that the modulus of the specimen could be calculated. Poisson's ratio was also determined using compression testing by measuring the transverse strain with a micrometer.

4.2.2 Analysis and interpretation

Size effect results were interpreted using available exact analytical solutions involving Bessel functions for torsion and bending of a Cosserat elastic solid and approximating the cross-section of each specimen as circular. Isotropic solutions are used because no anisotropic solutions are available. Elastic constants obtained are technical constants. This is in the same vein as classical constants obtained from quasistatic tests rather than ultrasonic tests on anisotropic solids. Size effects manifest as higher effective moduli in slender specimens than thick ones. The classical torsional rigidity is $\frac{M}{\theta} = G[\frac{\pi}{2}r^4]$. For Cosserat elasticity in this regime, $\frac{M}{\theta} = G[\frac{\pi}{2}r^4](1 + 6(\ell_t/r)^2)$. G is the true shear modulus in the absence of gradients; M is applied moment and θ is angular displacement. This expression is exact for N = 1; for other N the exact solution involves Bessel functions [13]:

$$\Omega = (1 + 6(\ell_t/r)^2)[\frac{(1 - 4\Psi\chi/3)}{1 - \Psi\chi}], \tag{4.12}$$

in which $\chi = I_1(pr)/prI_0(pr)$, $p^2 = 2\kappa/(\alpha + \beta + \gamma)$ and I_0 and I_1 are modified Bessel functions of the first kind. The constant Ψ only has an appreciable influence for very small radius specimens.

Because of the limitations of testing large samples imposed by the size of the BVS an asymptote of torsional rigidity vs. diameter could not be determined directly from this method. The asymptotic value of G was calculated from durometer measurements upon a separate cured block of silicone and from the Reuss relation in which tubes and silicone rubber were considered as constituents. ℓ_t and the value N were determined by fitting the entire set of experimental data to Eq.

4.12 using MATLAB. In order to fit Eq. 4.12 to the data, the thermodynamic lower bound of zero was applied to ℓ_t, and an upper bound of 1 was set for N. To accelerate convergence, an upper limit of 100 mm was chosen for ℓ_t.

For bending, the classical bending rigidity is $\frac{M}{\theta} = E[\frac{\pi}{4}r^4]$. For bending of a Cosserat elastic circular rod and radius r, the rigidity ratio is approximately

$$\Omega \approx 1 + 8(\ell_b/r)^2 \frac{(1-(\beta/\gamma)^2)}{(1+\nu)}. \tag{4.13}$$

The expression is approximate for small bending characteristic length $\ell_b << r$. The exact form, involving Bessel functions, is

$$\Omega = 1 + 8(\ell_b/r)^2 \frac{(1-(\beta/\gamma)^2)}{(1+\nu)} + \frac{8N^2}{(1+\nu)}[\frac{(\beta/\gamma+\nu)^2}{\zeta(\delta a) + 8N^2(1-\nu)}] \tag{4.14}$$

with $\delta = N/\ell_b$ and $\zeta(\delta r) = (\delta r)^2[((\delta r)I_0((\delta r)) - I_1((\delta r)))/((\delta r)I_0(\delta r) - 2I_1(\delta r))]$.

Similarly for bending, the asymptotic value of E was impossible to determine via BVS experimentation because of size limitations. Consequently, compression testing was performed to determine the value. Longitudinal compression testing was conducted to calculate Poisson's ratio for bending calculations. The remaining parameters, N, β/γ, and ℓ_b, were determined by fitting the entire set of experimental data for bending to Eq. 4.14 using MATLAB. To allow fitment, the thermodynamic lower bound of zero was used for ℓ_b; similarly, the allowed range for N is from zero to one and β/γ from -1 to 1.

4.3 Results and discussion

Density of corrugated tubing specimens composed of more than one tube was independent of size to within ten percent. The single tube specimen was about half of the density of the larger specimens on average. The discrepancy in density was cause by the silicone rubber matrix in samples composed of more than one segment of tubing.

Results of torsion size effect studies are shown in Figure 4.3.

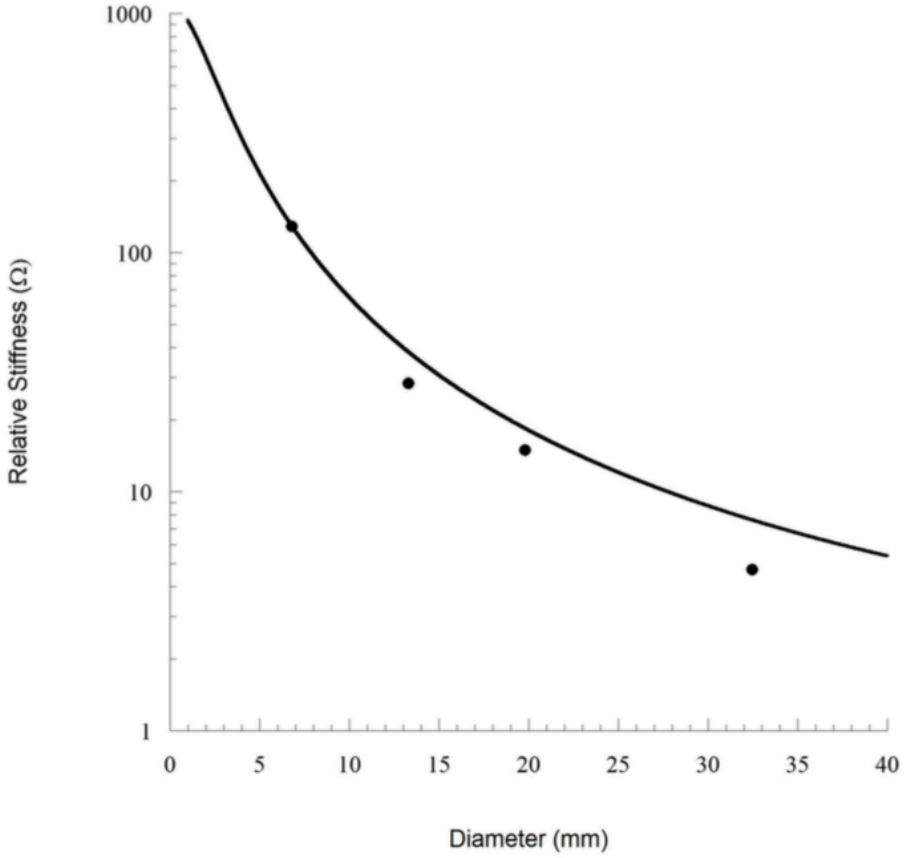

FIGURE 4.3: Size effects for corrugated tubing specimens in torsion. Points are experimental. Curve is theoretical for G = 890 kPa, ℓ_t = 17.3 mm N = 0.996 and Ψ = 1.5. Classical elasticity ($\ell_t = 0$) predicts constant Ω = 1 independent of diameter.

For corrugated tubing specimens in torsion, G = 890 kPa, ℓ_t = 17.3 mm N = 0.996 and Ψ = 1.5 when Poisson's ratio is 0.3. The goodness of fit was $R^2 = 0.99$. The maximum size effect in torsion was Ω = 128.8. The asymptotic value of G was located by using a durometer to determine the modulus of the silicone matrix materials used in the composite. The inferred Young's modulus of the silicone was approximately 1 MPa so the shear modulus is 0.33 MPa. By measuring the volume fraction of the silicone rubber matrix and using the Reuss relation, the asymptotic shear modulus for the composite was calculated to be 0.89 MPa.

Results of bending size effect studies are shown in Figure 4.4.

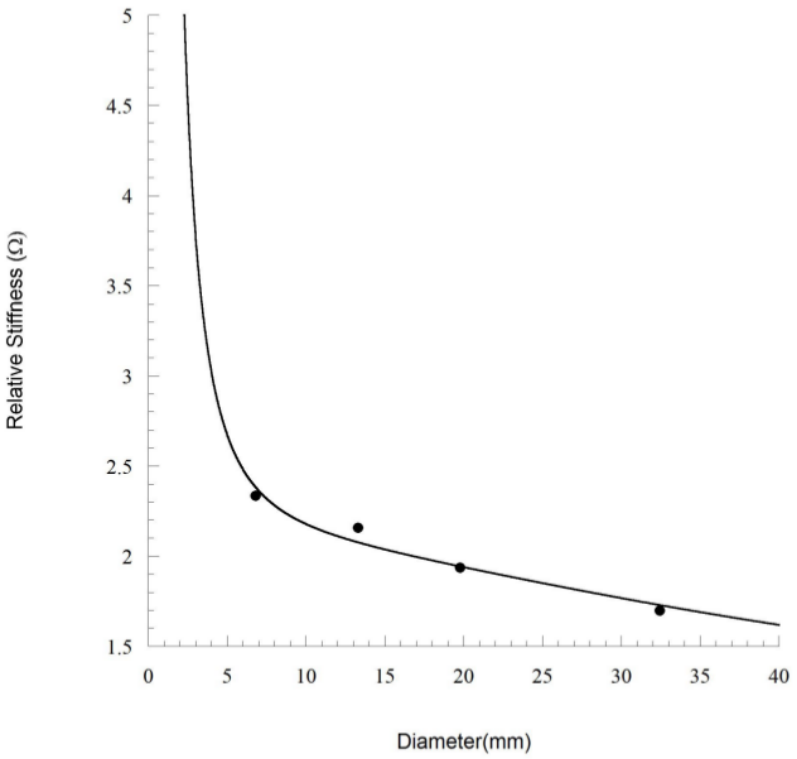

FIGURE 4.4: Size effects for corrugated tubing specimens in bending. Points are experimental. Curve is theoretical for β/γ = 0.995, N = 0.999, E = 14.2 MPa, and ℓ_b = 7.91 mm. Classical elasticity predicts constant $\Omega = 1$ independent of diameter.

Initial fitting of the data using the asymptotic value for E found from compression testing at 1 Hz, 14.2 MPa, and the Poisson's ratio 0.0 ± 0.1 found from compression testing yielded poor results. This is attributed to the single measurement of Poisson's ratio from longitudinal compression testing and the anisotropic structure of the specimens. The isotropic analytical solution links Poisson's ratio to the size effects; this is not expected in anisotropic solids. When subsequent fits were performed using an asymptotic value for E of 14.2 MPa and allowing Poisson's ratio to vary in addition to the other fitting parameters and elastic constants, ν = 0.3, ℓ_b = 7.91 mm, β/γ =

0.995, and N = 0.999. The goodness of fit was R^2 = 0.96. The largest size effect in bending under these conditions was Ω = 2.33. Because the composite specimens were anisotropic the characteristic length of bending was independent from the characteristic length of torsion. Also due to the anisotropy of the specimens, the coupling number, N, from torsion is not necessarily applicable to bending results which is why the N in this fit was allowed to varied. However, the N calculated from torsion experiments is very similar to the N calculated from bending experimentation.

The material has hexagonal structural symmetry, so it is elastically anisotropic. Consequently the properties obtained from the experiments are technical constants, not tensorial constants. This is analogous to materials testing in classical elasticity in which it is not always practical to incorporate a full anisotropic interpretation. The elastic symmetry of such a hexagonal structure is transversely isotropic which means properties in the transverse directions are independent of direction. That provides some simplification in the classical case; nevertheless no analytical solutions for Cosserat elasticity are known for such symmetry. Therefore the isotropic solutions are used and the elastic constants are interpreted as technical constants. Anisotropy cannot be a confounding variable because there are no size effects in classical elasticity even in the anisotropic case [82].

As for comparison with theory, no known analysis is available for the structure of the present material. Cosserat elastic constants have been calculated from theoretical homogenization of several lattices with straight ribs [47] [48] [49]. These are stretch dominated so the effects of rib bending and torsion are much smaller than the effects of rib extension. The characteristic lengths of such lattices are much smaller than the cell size. Two dimensional chiral honeycomb lattice structures analyzed as Cosserat continua disclosed bend dominated behavior in which Young's modulus is governed by rib bending. These honeycombs have large N approaching its upper bound 1, and characteristic length ℓ comparable to the cell size [50]. Sigmoid curvature of the lateral surfaces of bent square cross section bars was analyzed via Cosserat elasticity [55]. Such curvature requires $\beta/\gamma \neq -\nu$ and indeed it was observed in conventional as-received open cell foam. Although no formal measurements were made with the negative Poisson's ratio foam (for which

$\beta/\gamma \approx -\nu$), visual observation of such bending of a square cross section bar suggested any sigmoid curvature must be small.

In summary, large size effects are observed in the torsion of aligned corrugated tubing and silicone rubber matrix composites. The effects are consistent with Cosserat elasticity. Results do not necessarily exclude the presence of additional freedom such as that incorporated in micromorphic / Mindlin microstructure [7] theory or in microstretch elasticity [56].

4.4 Conclusions

Large size effects are observed in the torsion and bending of aligned corrugated tubing and silicone rubber matrix composites. These effects are inconsistent with classical elasticity, but can be modeled with Cosserat elasticity. The torsional characteristic length is much larger than the tube diameter.

4.5 Acknowledgements

We gratefully acknowledge support of this research by the National Science Foundation via Grant CMMI-1361832.

Chapter 5

Observation of Cosserat Elastic Effects in a Tetragonal Negative Poisson's Ratio Lattice

The following chapter has been published:
Z Rueger, D. Li and R.S. Lakes, "Observation of Cosserat Elastic Effects in a Tetragonal Negative Poisson's Ratio Lattice", Phys. Satatus Solidi B, 1521-3951, 1600840 (2017).

Abstract Size effects are explored experimentally in a tetragonal lattice structure. Size dependence of rigidity is nonclassical elastic and is interpreted via Cosserat elasticity. The characteristic lengths are about a third the cell size. The Cosserat characteristic length for torsion is ℓ_t = 5.6 mm. The characteristic length for bending is ℓ_b = 5.4 mm. The size effect in torsion was a factor 4.5 in rigidity. The ratio of characteristic length to cell size is larger than in fully stretch dominated lattices but smaller than in bend dominated honeycombs or foams.

5.1 Introduction

The first negative Poisson's ratio materials, honeycombs in 2D [70] and foams in 3D [61] had a structure size sufficiently large to be apparent to the unaided eye. It had been proposed that a coarse structure was required for negative Poisson's ratio [83]. The size of the structure is not, however, pertinent in that context. Poisson's ratio is a concept in classical elasticity which has no length scale [84]. Indeed, in some negative Poisson's ratio materials, particularly those experimentally associated with phase transformations in gels [85] and in polycrystalline quartz [86], the governing structure is on the atomic scale. Analyses of a 2D array of hard hexamer discs indicated the existence of a phase transition between a tilted and a straight phase [63]; results suggested negative Poisson's ratio associated with the transformation to tilted phase. Numerical results also reveal a decrease in Poisson's ratio during phase transformations; such a change is a good indicator of transformation [87] [88]. Structure size is however associated with phenomena such as size dependence of rigidity in torsion and bending (size effects), non-classical values of stress concentration, and dispersion of waves. Continuum theories are widely used to represent physical structured materials to facilitate practical calculations. Classical elasticity is one such theory but not the only one. One may incorporate less freedom as in the uniconstant elasticity theory of Navier [1]. This theory only allowed one elastic constant, a modulus. The analysis assumed that forces act along the lines joining pairs of atoms and that forces are proportional to changes in distance between atoms. The theory predicts a Poisson's ratio of 1/4 for all isotropic materials. Because experiments disclosed a range of Poisson's ratios, the uniconstant theory was abandoned. Classical isotropic elasticity has two independent elastic constants and allows Poisson's ratio in the range -1 to 1/2. Cosserat elasticity incorporates more freedom than classical elasticity. Cosserat elasticity [3], (with inertia terms called micropolar [9]) allows points to rotate as well as translate. Cosserat elasticity also incorporates a couple stress (a torque per unit area) as well as the force per unit area of classical elasticity. There are six independent elastic constants for the isotropic Cosserat solid and even more if it is anisotropic.

The Cosserat couple stress arises from a superposition of bending and twisting moments that are transmitted by the material's structural elements. The Cosserat micro rotation is associated with the rotation of the structural elements. Bending moments on ribs of honeycomb or foam were analyzed in the classical elastic treatments of foam [2] but no effects of rotation gradients were considered.

The constitutive equations for an anisotropic [9] Cosserat elastic solid are as follows.

$$\sigma_{ij} = C_{ijkl}\epsilon_{kl} + P_{ijkl}\phi_{k,l}, \tag{5.1}$$

$$m_{ij} = Q_{ijkl}\phi_{k,l} + P_{ijkl}\epsilon_{kl}, \tag{5.2}$$

Here ϵ_{kl} is strain, σ_{ij} is stress (symmetric in classical elasticity but asymmetric here), C_{ijkl} is the elastic modulus tensor. The usual Einstein summation convention is assumed in which repeated indices are summed over. m_{ij} is the couple stress tensor, moment per unit area, asymmetric in general. P_{ijkl} and Q_{ijkl} are Cosserat elastic constants that provide sensitivity to local gradient of (micro) rotation vector. The Cosserat microrotation vector ϕ_i is kinematically distinct from the macrorotation vector $r_i = (e_{ijk}u_{k,j})/2$ associated with the motion of neighboring points.

The lattice structure under consideration is anisotropic, however isotropic analysis is more developed and provides physical insight. The constitutive equations for an isotropic micropolar solid [9] are:

$$\sigma_{ij} = 2G\epsilon_{ij} + \lambda\epsilon_{kk}\delta_{ij} + \kappa e_{ijk}(r_k - \phi_k) \tag{5.3}$$

$$m_{ij} = \alpha\phi_{k,k}\delta_{ij} + \beta\phi_{i,j} + \gamma\phi_{j,i} \tag{5.4}$$

There are six independent elastic constants for an isotropic Cosserat solid. They are λ, G, α, β, γ, κ. It is appropriate to define technical constants as follows. They are helpful for physical insight

as is the case comparing tensorial constants and technical constants in classical elasticity.

$$Young's\ modulus \qquad E = \frac{G(3\lambda + 2G)}{\lambda + G} \tag{5.5}$$

$$Shear\ modulus \qquad G \tag{5.6}$$

$$Poisson's\ ratio \qquad \nu = \frac{\lambda}{2(\lambda + G)} \tag{5.7}$$

$$Characteristic\ length,\ torsion \qquad \ell_t = \sqrt{\frac{\beta + \gamma}{2G}} \tag{5.8}$$

$$Characteristic\ length,\ bending \qquad \ell_b = \sqrt{\frac{\gamma}{4G}} \tag{5.9}$$

$$Coupling\ number \qquad N = \sqrt{\frac{\kappa}{2G + \kappa}} \tag{5.10}$$

$$Polar\ ratio \qquad \Psi = \frac{\beta + \gamma}{\alpha + \beta + \gamma}. \tag{5.11}$$

Stress and strain fields in Cosserat solids differ from classical predictions. For example, size effects occur in the analysis of torsion [13] and bending [14] of circular cylinders of Cosserat elastic cylinders. Slender specimens are stiffer than predicted classically. Small holes in a plate exhibit a lower stress concentration than larger ones [15] in contrast to classical elasticity.

A variety of experiments have disclosed Cosserat elastic effects. Size effects consistent with Cosserat elasticity occur in the torsion and bending of closed cell foams [22, 23], open cell foam [73], negative Poisson's ratio foam [80], and compact bone [21]. These effects are consistent with Cosserat elasticity. Apparent modulus increases as specimen size is reduced. In comparison, classical elasticity predicts apparent modulus independent of specimen thickness. For Cosserat effects to be observable, the material micro-structure size must be nontrivial in comparison with length scales in the experiment. This is a necessary but not a sufficient condition. Indeed, a composite containing aluminum beads in an epoxy matrix was tested for Cosserat effects but it was found to behave according to classical elasticity [13].

The Cosserat characteristic length for a polycarbonate honeycomb was determined [33] from

experimental strain and displacement fields. Warp in torsion of a square cross section bar is predicted to be reduced [34] in comparison with classical predictions. Strain distributions were experimentally measured in square cross-section bars of human compact bone [35] and found to follow the Cosserat prediction. Holographic methods disclosed [36] deformation occurred in the corners where it would be classically zero. Holographic methods also revealed reduced warp deformation in square bars of closed cell foam [37], following Cosserat elasticity.

The present research deals with size effects in a designed tetragonal polymer lattice. This lattice was shown, both numerically and experimentally in a companion paper to have a negative Poisson's ratio, tunable via geometric variables [89]. For a lattice of the type studied here, Poisson's ratio is -0.5 for stress applied in the axial direction.

5.2 Methods

5.2.1 Materials and experiment

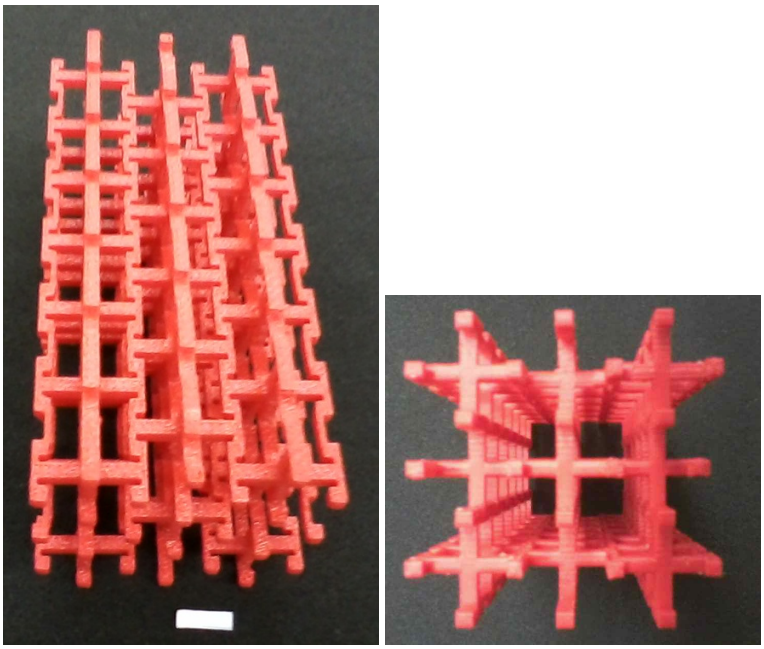

FIGURE 5.1: 2x2 tetragonal lattice structure (left). Scale bar, 1 cm. End view (right).

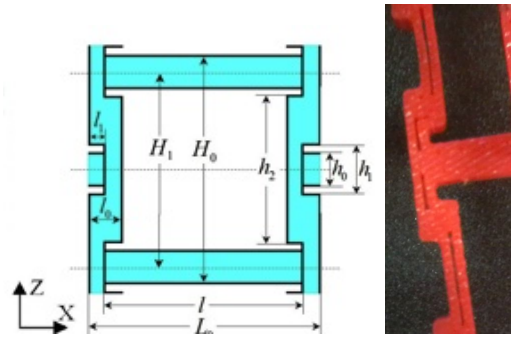

FIGURE 5.2: Diagram (left) showing dimensions adapted from [89]. Slot (right) in present specimens.

Lattices (Figure 5.1) were designed as described in a companion paper [89] and were made using a Stratasys Dimension Elite 3D printer. Four progressively larger lattices were created corresponding to 1,2,2.5, and 3 unit cells. While the unit cells are not repeat units, this convention was consistent across all specimens. The parent material was ABS polymer with a claimed Young's modulus of 2.2 GPa and a Poisson's ratio of 0.39. The print resolution is 0.25 mm. The mid-size sample was 100 mm in height and 47.5 mm for the side length. Lattice specimens were cemented to metal end pieces to provide appropriate boundary conditions. Dimensions (Figure 5.2) of the original lattice were H_0 = 17.5 mm, L = 17.5 mm, l = 15.3 mm, l_0 = 2.5 mm, l_1 = 1.3 mm, h_0 = 2.5 mm, h_1 = 5 mm, h_2 = 10 mm. Dimensions of the present lattice were essentially identical, within the resolution limit of the printer, H_0 = 17.7 mm, H_1 = 14.9 mm, L = 17.5 mm, l = 14.9 mm, l_0 = 2.5 mm, l_1 = 1.3 mm, h_0 = 2.7 mm, h_1 = 5 mm, h_2 = 10 mm.

Tests were done in compression to evaluate the behavior in the absence of macroscopic gradients of strain and rotation. This was done using a test frame at constant strain rate. Poisson's ratio was also determined using compression testing by measuring the transverse deformation via digital photography and via a micrometer. Torsional and bending rigidity of lattice specimens of different size were determined via broadband viscoelastic spectrometry (BVS). The BVS device generates torque using a dual Helmholtz coil acting upon a magnet attached to the specimen's end piece. The magnet was centered in the coil. Deformation is measured by measuring the position of a reflected laser beam using a digital sensor. The sensor was calibrated using a precision micrometer. Specimens were too large to fit in the coil, therefore an alumina stalk with a magnet on one end was fixed to the lower end plate. The laser mirror was attached to the lower end plate to avoid any error from compliance of the stalk. A mirror was also attached to the upper end plate and further measurements conducted to evaluate the effect of instrument compliance.

Magnet calibration in the BVS was done as in prior studies with this instrument. Torque and angular displacement of a rod of 6061 aluminum alloy of known elastic properties were measured. The torsion calibration constant was 3.81×10^{-4} Nm/A and the bending one was 6.50×10^{-4} Nm/A. The specimen top end plate was attached to a 25 mm diameter steel rod to support the

specimen inside the BVS. Viscoelastic deformation was allowed to recover overnight prior to tests to enable stable measurements.

A 1 Hz sinusoidal signal from a SRS Model DS345 function generator was input first to the torsion Helmholtz coil, then to the bending coil. This is well below any resonant frequencies. The same frequency was used for all specimens so viscoelastic effects are decoupled from the size effects to be probed. Torque was inferred from the voltage across a 1Ω resistor in series with the coil. The signals for torque vs. angular displacement were displayed as a Lissajous figure on a digital oscilloscope (Tektronix TDS3014B) using DC coupling. Effective modulus was inferred from torque and angle signals. The maximum strain was less than 2×10^{-5}. This is well within the range of linearity for this material. Linearity was verified from the shape of the load deformation curves.

5.2.2 Analysis and interpretation

Size effect results were interpreted in the context of Cosserat elasticity. Approximate solutions of the bending and torsion problems are available. The bending rigidity ratio for a rectangular cross section bar of width a depends on both the characteristic length and on Poisson's ratio [55]. If $\beta/\gamma = -\nu$, the rigidity ratio $\Omega = \frac{M}{1/R}\frac{1}{EI}$ is, with M as moment and R as radius of curvature,

$$\Omega = [1 + 24(\ell_b/a)^2(1-\nu)]. \tag{5.12}$$

For other values of Poisson's ratio, the ratio is, (to fourth order in ℓ_b/a),

$$\Omega = \left[1 + 24\frac{1 + 2\frac{\beta}{\gamma}\nu + \nu^2}{1+\nu}\left(\frac{\ell_b}{a}\right)^2 - 480\left(\frac{\beta}{\gamma}+\nu\right)^2 \frac{44 - 38\nu + 3N^2(1-\nu)(13-9\nu)}{N^2(1+\nu)(22-19\nu)}\left(\frac{\ell_b}{a}\right)^4\right]. \tag{5.13}$$

Torsion of a square cross section Cosserat elastic bar of width a gives rise to the following relation between torque and angle. When $\kappa \to \infty$, which corresponds to the coupling number

$N = 1$, the total torque M [90] simplifies to

$$M = \frac{4}{21} G (\frac{a}{2})^4 \theta \frac{1796 + 126\left(449 + 2740\bar{\ell}^2 + 3960\bar{\ell}^4\right)\bar{\ell}^2 + 693\left(152 + 2280\bar{\ell}^2 + 6615\bar{\ell}^4\right)\bar{\ell}_b^2}{8\left(19 + 465\bar{\ell}^2 + 990\bar{\ell}^4\right) + 1485\left(6 + 49\bar{\ell}^2\right)\bar{\ell}_b^2}. \quad (5.14)$$

in which $\bar{\ell} = 2\ell_t/a$, $\bar{\ell}_b = 2\ell_b/a$ and θ as the angular displacement per length. This solution is superior in the regime of strong coupling or for $\beta/\gamma < 0$, to that of [34], which overestimates the effects for large N.

Because the solid is not isotropic, no attempt was made to further refine the interpretation. No analytical solutions for interpretation are known for anisotropic solids. Elastic constants determined via such a procedure are technical constants. Similarly, classical elastic constants as technical constants for anisotropic materials are obtained from results of standard tensile or compressive tests in principal directions. Size effects do not occur in classical anisotropic elasticity [82]; rigidity depends on thickness as it does in isotropic elasticity. Size effects are therefore a manifestation of nonclassical elasticity and cannot be explained by anisotropy.

In prior studies on round specimens, size effect results were interpreted using exact analytical solutions involving Bessel functions [13] [14].

If either $N \to 1$ or the specimen is much thicker than the characteristic length, the relations for round specimens are simpler than the exact solutions: $\Omega \approx (1 + 6(\ell_t/r)^2)$ for torsion and $\Omega \approx 1 + 8(\ell_b/r)^2 \frac{(1-(\beta/\gamma)^2)}{(1+\nu)}$ for bending. Size effects in both square and round specimens give rise to higher effective moduli in slender specimens than in thick ones.

For materials with small characteristic length, asymptotic values of G and E are easily determined from sufficiently thick specimens. For materials with large structure size, there is an upper limit to the thickness that can be tested with the present method. Consequently, compression testing was performed to determine the asymptotic value of E in the absence of gradients. The characteristic lengths ℓ_t and ℓ_b were determined by fitting the torsion data to Eq. 5.14 and the bending data to Eq. 5.12 using MATLAB.

5.3 Results and discussion

Specimens 3D printed for size effect studies had a slender pore or slot in some ribs as shown in Figure 5.2. Compression moduli were measured as 19.4 MPa for the 4x4 specimen, 20.4 MPa for the 2x2 specimen (Figure 5.1), and 25.7 MPa for the 1x1 specimen, all with the same orientation of ribs. The specimen studied in the companion paper [89] on Poisson's ratio was slightly different in the 3D printed structure; the ribs had no such slot. The relative density was 0.092. The average density of the present specimens was 0.087 g/cm^3. Assuming the density of solid ABS polymer as 1.04 g/cm^3, the relative density is 0.084. The difference is attributed to variance in the 3D printing process. Results of torsion size effect experiments and interpretation via Eq. 5.14 are shown in Figure 5.3.

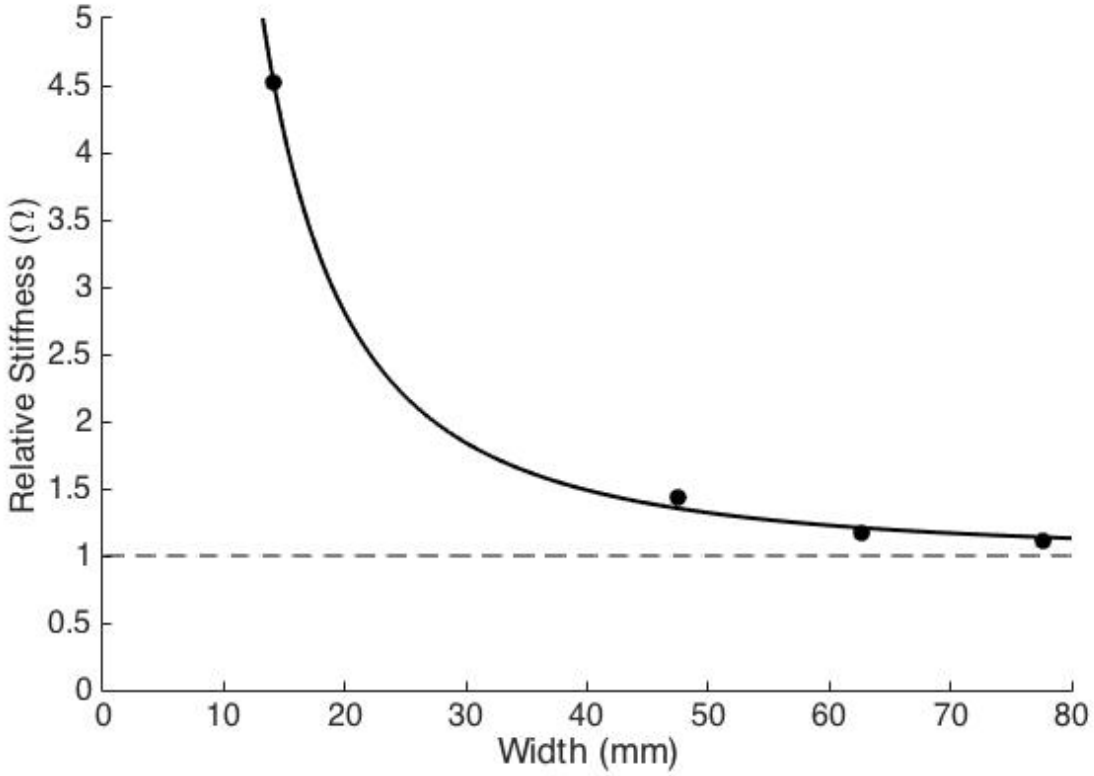

FIGURE 5.3: Size effects for lattice specimens in torsion. Points are experimental. Curve is theoretical for G = 0.67 MPa, ℓ_t = 5.6 mm, ℓ_b = 5.4 mm, N = 1. Classical elasticity (ℓ_t = 0) predicts constant Ω = 1 independent of diameter which is indicated by the horizontal dashed line.

For specimens in torsion, G = 0.67 MPa, ℓ_t = 5.6 mm, ℓ_b = 5.4 mm. The goodness of fit was $R^2 = 0.999$. The maximum size effect in torsion was Ω = 4.5. The rigidity expressed in Eq. 5.14 is strongly dependent on ℓ_t and weakly dependent on ℓ_b. The asymptotic value of G was located via the curve fit. The characteristic length is about a third the cell size.

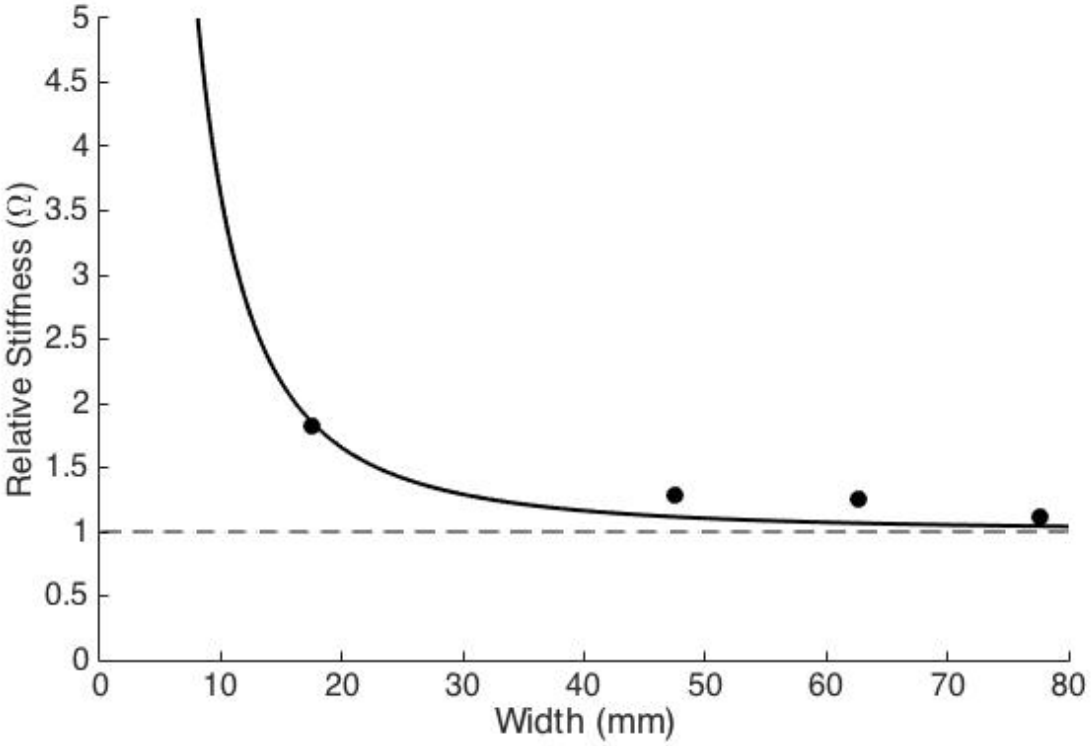

FIGURE 5.4: Size effects for lattice specimens in bending. Points are experimental. Curve is theoretical for ℓ_b = 5.4 mm, $\beta/\gamma + \nu$ = 0.002, N = 0.46, via Eq. 5.13. Classical elasticity predicts constant Ω = 1 independent of diameter which is illustrated by the horizontal dashed line.

Results of the bending size effect studies based on fit to Eq. 5.13 are shown in Figure 5.4, ℓ_b = 5.4 mm, $\beta/\gamma + \nu$ = 0.002, N = 0.46, ν = -0.5. The asymptotic value for E = 27.6 MPa was found as follows. The compression modulus obtained at constant strain rate corresponds to a test at a low frequency - approximately 0.08 Hz . This modulus was converted to a compression modulus at 1 Hz via interrelation among viscoelastic functions using the average loss tangent (0.27) of the largest three specimens. The goodness of fit was R^2 = 0.75. Because the composite specimens were anisotropic the characteristic length of bending is independent of the characteristic length of torsion. Anisotropy implies the coupling number N for torsion need not equal the value for bending.

The material has tetragonal structural symmetry. Elastic behavior is therefore anisotropic. Consequently the properties obtained from the experiments are technical constants, not tensorial constants. This is analogous to materials testing in classical elasticity in which it is not always practical to incorporate a full anisotropic interpretation. No analytical solutions are available for tetragonal Cosserat elasticity. Therefore the elastic constants obtained are interpreted as technical constants. Anisotropy is not a confounding variable because size effects do not occur in classical elasticity even in the anisotropic case [82].

Homogenization analyses have been done for several lattices with straight ribs [47] [48] [49]. These lattices are stretch dominated: the overall lattice modulus is governed by axial deformation (stretching or compressing), of the rib elements. Consequently the effects of rib bending and torsion, which govern the Cosserat constants, are much smaller than the effects of rib extension. The Cosserat characteristic lengths of such stretch dominated lattices are much smaller than the cell size. By contrast, analysis of two dimensional chiral honeycomb lattice revealed bend dominated behavior. The Cosserat characteristic length ℓ is comparable to the cell size [50]. Moreover in such honeycomb, N approaches its upper bound 1. In open cell foams [73] and in negative Poisson's ratio foams [80] derived from them, ℓ is greater than the cell size. Specifically, ℓ_t is a factor 1.8 to 4 greater than the cell size, and ℓ_b is a factor 4.9 to 7.5 greater than the cell size, depending on the kind of foam. Such foams are highly bend dominated. Cosserat effects are therefore considerably stronger in bend dominated lattices and materials studied thus far than in stretch dominated ones. The present lattice is considered bend dominated based upon dependence of the modulus on relative density of the lattice [89]. However the ribs are aligned so that the axial modulus is enhanced. The Cosserat characteristic length of cellular solids depends on the ratio of torsion and bend rigidity of *ribs* to their axial rigidity. Therefore it is to be expected that the Cosserat effects are not as pronounced as in foams. The ratio of characteristic length to cell size is larger than in fully stretch dominated lattices but smaller than in bend dominated honeycombs or foams.

Cosserat elasticity facilitates understanding of size effects due to distributed torques propagated through the structure of a heterogeneous material. Size effects may rise from a variety of

causes. In foams, a layer of surface damage can give rise to a softening effect in which slender specimens appear more compliant than large ones [91]; this effect is opposite that in Cosserat solids. Edge effects in 2D negative Poisson's ratio structures of rotating squares have been predicted [92]. The apparent rigidity for axial tension depends on size as a result of the boundary conditions being different from conditions in the bulk. These effects differ from effects in Cosserat solids in that (i) they are not driven by gradients, and (ii) unlike Cosserat effects they do not obey Saint Venant's principle. Cosserat size effects are driven by gradients that occur in torsion and bending; the bar can be arbitrarily long; there are no size effects in tension.

Cosserat elasticity has also been used in analysis of granular materials [93]; a Cosserat fluid model successfully describes collisional granular flows on a slope [94]. 2D ensembles of hard disks in an enclosure have been studied from a thermodynamic perspective [95]; elastic aspects were considered in a classical context [96]. In such systems, size effects might occur due to exclusion of discs by the boundary in contrast to Cosserat type effects due to moments. If rotational energy is considered, there will be a conceptual link with the Cosserat approach.

Size effects are not the only result of nonzero structure size interpreted via Cosserat elasticity. Stress concentrations associated with holes are reduced in comparison with classical predictions [15]; the effect is more pronounced for small holes. Similarly stress concentration around a notch is reduced in comparison with predictions of classical elasticity. The result is improved toughness in the presence of such defects.

In summary, size effects are observed in torsion and in bending of tetragonal auxetic lattices. The lattices are therefore not classically elastic. The size effects are interpreted via Cosserat elasticity. Continuum theories with more freedom, e.g. micromorphic / Mindlin microstructure [7] elasticity or microstretch elasticity [56] are not excluded; they are not necessary for the present observations. For example, the Mindlin elasticity theory, in which *points* translate, rotate, and deform, allows 18 elastic constants for an isotropic solid, and microstretch elasticity allows 9 constants for an isotropic solid.

5.4 Conclusions

Size effects occur in the torsion and bending of lattice structures. These effects are not consistent with classical elasticity. They are interpreted with Cosserat elasticity. The characteristic lengths are about a third of the cell size. The Cosserat torsional characteristic length is ℓ_t = 5.6 mm. The bending characteristic length is ℓ_b = 5.4 mm. The size effect in torsion is a factor 4.5 in rigidity.

5.5 Acknowledgements

We gratefully acknowledge partial support of this research by the National Science Foundation via Grant CMMI-1361832. We also acknowledge partial support by The National Natural Science Foundation of China (11304033) and the Fundamental Research Funds for the Central Universities (N150504006). D. Li would also like to thank the financial support from the China Scholars Council (File No. 201506085013).

Chapter 6

Strong Cosserat elasticity in a transversely isotropic polymer lattice

The following chapter has been published:
Z Rueger and R.S. Lakes, "Strong Cosserat elasticity in a transversely isotropic polymer lattice", Phys. Rev. Lett., **120**, 065501 (2018).

Abstract Large size effects are experimentally measured in lattices of triangular unit cells: about a factor of 36 in torsion rigidity and 29 in bending rigidity. This nonclassical phenomenon is consistent with Cosserat elasticity which allows for rotation of points and distributed moments in addition to the translation of points and force stress of classical elasticity. The Cosserat characteristic length for torsion is ℓ_t = 9.4 mm; for bending it is ℓ_b = 8.8 mm; these values are comparable to the cell size. Nonclassical effects are much stronger than in stretch dominated lattices with uniform straight ribs. The lattice structure provides a path to attainment of arbitrarily large effects.

Continuum theories of elasticity are widely used for representing materials with microstructure, including composites and lattice “metamaterials”, as continuous media. The currently accepted classical theory permits the Poisson’s ratio in isotropic materials to range from -1 to 1/2 and incorporates two independent elastic constants. Theory with less freedom was tried: the uniconstant theory of elasticity, developed by Navier [1] incorporates only one elastic constant, a

modulus, and was based on an assumption that forces acted along the lines joining pairs of atoms and were proportional to changes in distance between them. Navier's theory predicted a Poisson's ratio of $1/4$ for all isotropic materials and was abandoned when experiments demonstrated a range of Poisson's ratios so the current classical theory was adopted. The Cosserat theory [3] (with inertia terms called micropolar [9]), has more freedom than classical elasticity; it incorporates a local rotation of points and a couple stress (torque per unit area) as well as the translation of points and force stress of classical elasticity. The Cosserat theory of elasticity has six independent isotropic elastic constants and even more constants if the material is anisotropic. In contrast to classical elasticity, Cosserat elasticity incorporates a characteristic length scale in the continuum; the solid becomes sensitive to strain gradients, hence has a nonlocal aspect, and can support an asymmetric stress.

Classical elasticity is entirely adequate for macroscopic specimens in which the structure size is many orders of magnitude smaller than the experimental size scale; macroscopic scale tests for Cosserat effects in aluminum revealed classical behavior [25]. Nonclassical elastic effects are expected if the ratio of structural to experimental length scale is non-negligible. At the atomic scale, non-central forces are associated with moments such as those between dipoles; these moments can be subsumed in a Cosserat analysis. Dispersion of waves of length a small multiple of the lattice spacing was used to infer Cosserat behavior in diamond crystals [26]; the inferred characteristic length was about 0.2 nm. More recently, classical elasticity [27] was predicted to break down in crystalline materials in the length scale range of 1-10 nm. In chiral cholesteric elastomers [97] the characteristic length was predicted to be on the order of 10 nm. These length scales are on the order of the structure size. Cosserat type freedom is not limited to elasticity; it can occur in other physical properties. Piezoelectric materials are known to exhibit nonclassical sensitivity to gradients [98], interpreted via a nonlocal concept [99]. The characteristic length, governed by the spacing of ions in the lattice, is enhanced in ferroelectrics so that effects were observed in layers several μm thick. Such materials in recent studies have been called flexoelectric [100].

A larger characteristic length is to be expected in materials with larger structural length scales.

This is not a sufficient condition; the specific nature of the structure is pertinent as well. The Cosserat couple stress arises from the superposition of bending and twisting moments transmitted by the structural elements in materials. The Cosserat local rotation corresponds to the rotation of the structural elements. Forces and moments are also considered in the classical analyses of foam [70] in which classical elastic moduli were determined; effects of rotation gradients were not considered. Lattices with straight elastic ribs were analyzed via theoretical homogenization [47] [48] [49] as Cosserat solids. Such lattices, despite their structure, are nearly classical; the Cosserat characteristic lengths are much smaller than their cell sizes. The reason is that these structures are stretch dominated: the effects of rib extension greatly exceed the effects of rib bending and torsion. Rib extension in such structures governs the force stress hence the classical elastic moduli; rib bending and torsion transmits moments corresponding to the Cosserat couple stress. The distributed Cosserat moments are minimal in comparison with the forces, so the characteristic length is small compared with the cell size in such lattices.

A composite containing round aluminum beads in an epoxy matrix was tested experimentally for Cosserat effects and was found to be classical [13]. Indeed, composites containing stiff spheres were shown by homogenization analysis to have characteristic lengths of zero [101]. A dense closed cell polymer foam exhibited Cosserat effects; the characteristic length was comparable to the cell size (the largest cells had diameter 0.15 mm) but size effects (see below) were only about a factor of 1.3 as a result of weak coupling [22]. Rotational waves of the sort anticipated in Cosserat elasticity were observed in a non-cohesive granular assembly of metal spheres [102]. A value of κ (defined below) was inferred but characteristic lengths were not obtained; indeed the granular assembly was predicted to have rotation gradient sensitivity terms α, β, γ equal to zero hence zero characteristic length; as with composites with hard spheres, this is a degenerate case.

Lattices of the type presented in this Letter exhibit strong nonclassical effects consistent with Cosserat elasticity; the design provides a path to achieving arbitrarily large Cosserat effects.

In Cosserat elasticity the stress, σ_{jk}, can be asymmetric. The resulting moment is balanced by a couple stress, m_{jk}. The antisymmetric part of the stress is related to local rotations: $\sigma_{jk}^{antisym} =$

$\kappa e_{jkm}(r_m - \phi_m)$ in which κ is an elastic constant, ϕ_m is the rotation of points, called micro-rotation, e_{jkm} is the permutation symbol, and $r_k = \frac{1}{2}e_{klm}u_{m,l}$ is the macro-rotation based on the antisymmetric part of gradient displacement u_i. The constitutive equations for linear isotropic Cosserat elasticity [9] are as follows.

$$\sigma_{ij} = 2G\epsilon_{ij} + \lambda\epsilon_{kk}\delta_{ij} + \kappa e_{ijk}(r_k - \phi_k) \tag{6.1}$$

$$m_{ij} = \alpha\phi_{k,k}\delta_{ij} + \beta\phi_{i,j} + \gamma\phi_{j,i} \tag{6.2}$$

There are six independent elastic constants for an isotropic Cosserat solid. Constants λ, G have the same meaning as in classical elasticity; α, β, γ provide sensitivity to rotation gradients and κ quantifies the coupling between fields. Technical constants, derived from these elastic constants are beneficial for physical insight and are as follows.

Young's modulus $E = \frac{G(3\lambda+2G)}{\lambda+G}$, shear modulus G, Poisson's ratio $\nu = \frac{\lambda}{2(\lambda+G)}$, characteristic length, torsion $\ell_t = \sqrt{\frac{\beta+\gamma}{2G}}$, characteristic length, bending $\ell_b = \sqrt{\frac{\gamma}{4G}}$, coupling number $N = \sqrt{\frac{\kappa}{2G+\kappa}}$, polar ratio $\Psi = \frac{\beta+\gamma}{\alpha+\beta+\gamma}$. This is a generalization of the extraction of technical constants from tensorial ones in classical elasticity.

There are several key consequences of Cosserat elasticity which differ from classical predictions. Circular holes exhibit a lower stress concentration factor than expected classically and small holes exhibit less stress concentration than larger ones [15]. A characteristic of Cosserat elasticity pertinent to the research presented in this letter is the prediction of a size effect in the torsion [22] and bending [23] of circular cylinders of Cosserat elastic materials. These size effects manifest as slender cylinders appearing stiffer than predicted classically.

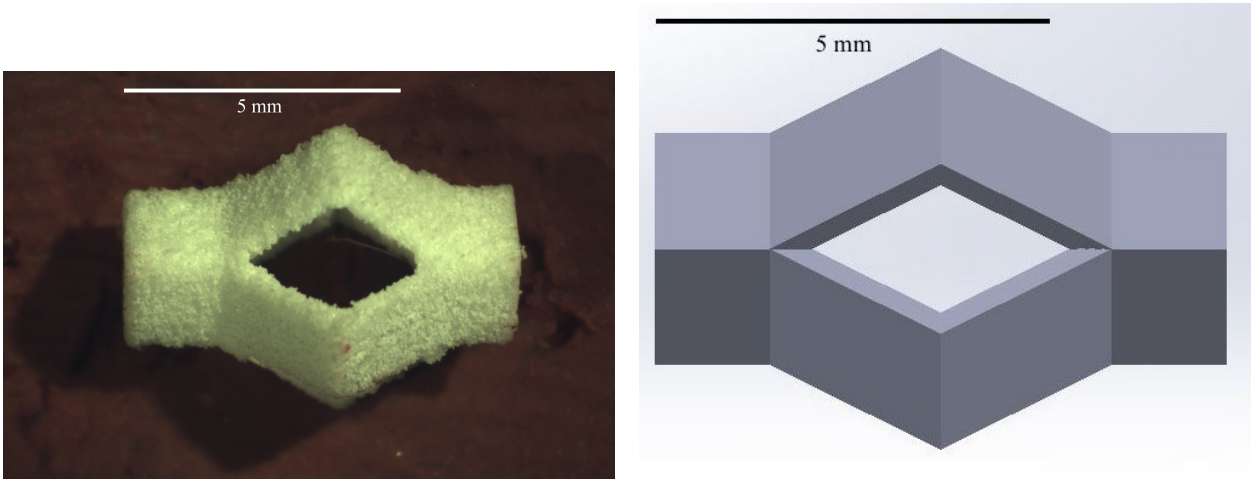

(A) 3D printed rib structure. (B) CAD rib structure.

FIGURE 6.1: 3D printed rib structure vs. idealized drawing. Scale bar, 5 mm.

The lattices considered in this letter were developed to achieve strong Cosserat effects by decoupling the rib rigidity in torsion and bending from its rigidity in extension. This maximizes sensitivity to rotation gradient. These lattices were embodied via selective laser sintering (SLS), an additive manufacturing technique. The lattice was modeled in SolidWorks and was converted to STL format for export to 3D printing. Specimens were printed by a 3D Systems sPro 60 HD-HS printer. The parent material was a polyamide polymer equivalent to Nylon 12. Each rib element (Figure 6.1) consists of square section tubular segments with a portion that approximates a Sarrus linkage. The ideal Sarrus linkage contains hinged elements and offers zero resistance to axial compression but resists torsion. The measured effective Young's modulus in bending of one rib element was 281 MPa; in compression it was 14 MPa; for a solid rod these moduli would be equal. The torsional modulus was 387 MPa. The ribs, though not hinged, therefore resist torsion and bending to a much greater extent than compression. This rib design was created to be sensitive to gradients and thus demonstrate large size effects when used to construct 3-D structures. Each rib connects with its neighbors via hexagonal nodes shown in Figure 6.2. The lattice comprised of these ribs consists of triangular prism unit cells of which the side length of the triangular bases

was 10.5 mm and the height was 9.0 mm. The lattice density was 0.16 $\frac{g}{cm^3}$.

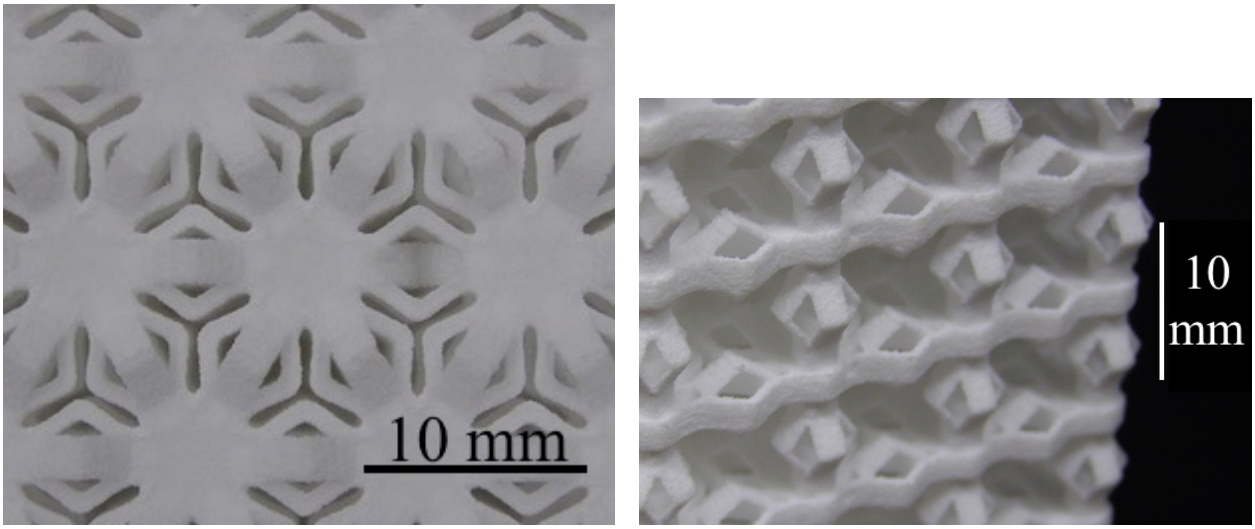

(A) Lattice structure in cross section.

(B) Lattice structure.

FIGURE 6.2: Cross section and side view of 3D printed lattice structure. Scale bar, 10 mm.

Cosserat effects were probed by measuring size dependence of rigidity at constant frequency. This protocol provides sensitivity to spatial gradients; it is insensitive to time derivatives because all experiments were done at the same frequency. By contrast, in wave methods, a change in wavelength is accompanied by a change in frequency. Therefore wave dispersion due to viscoelastic damping cannot be distinguished from dispersion due to sensitivity to spatial gradients. Five structures of increasing size, but the same aspect ratio, were printed. Specimens had complete cells with no partial cells; this was done by making cross section shapes aligned with the symmetry axes. All sections were hexagonal except the smallest which was triangular. Equivalent circles were inscribed for interpretation. The specimens, from smallest to largest, were composed of the following number of unit cells in cross-section by height: 1x3, 6x7, 24x13, 54x19, 96x26.

These specimens were tested for torsional and bending rigidities using a Broadband Viscoelastic Spectrometer (BVS) [41]. This apparatus uses a pair of Helmholtz coils to apply a torque of

controllable direction to the specimen via a magnet attached to the base via a ceramic stalk and cement. The magnet was calibrated in the BVS using a lock-in amplifier. A mirror was glued to the specimen's base edge. To measure displacement, the beam of a semiconductor laser was reflected off this mirror and directed to a silicon light detector. The light detector was calibrated by moving it a known distance, via calibration stage, and measuring output voltage. A calibration curve was generated and the change in output voltage per change in position was used as the beam position calibration constant (V/μm).

A sinusoidal signal with a frequency of 1 Hz, was input to the torsion Helmholtz coil. The same frequency was used for all specimen sizes to decouple viscoelastic effects from the size effects being probed. The resulting torque vs. angular displacement signals were displayed as a Lissajous figure on an oscilloscope; the modulus and viscoelastic damping of the structures were then calculated. To measure bending moduli, the orthogonal bending Helmholtz coil was used and the light detector was switched to measure vertical displacement. The calibration constant for the light detector was determined as before and the magnet's calibration constant for bending was used in calculations.

Compression tests were conducted using a screw-driven test frame to ascertain the Young's modulus of the specimens in the absence of macroscopic gradients of strain or rotation as well as to measure the Poisson's ratio. Anisotropy of modulus was probed via propagation in different directions of acoustic waves of wavelength much larger than the cell size.

Size effects in torsion were interpreted using the following exact solution for a Cosserat elastic circular rod of radius r with Ω as the ratio of structural rigidity to its classical counterpart [13]:

$$\Omega = (1 + 6\{\frac{\ell_t}{r}\}^2)\left[\frac{1 - \frac{4}{3}\Psi\chi}{1 - \Psi\chi}\right] \tag{6.3}$$

in which $\chi = I_1(pr)/prI_0(pr)$, $p^2 = 2\kappa/(\alpha + \beta + \gamma)$ and I_0 and I_1 are modified Bessel functions of the first kind. Classical torsional rigidity is $\frac{M}{\theta} = G[\frac{\pi}{2}r^4]$. G is the true shear modulus in the absence of gradients, M is the applied moment and θ is the angular displacement per length.

The shear modulus G, characteristic length of torsion ℓ_t, and the coupling number N were found by fitting Equation 6.3 to the full set of experimental data using MATLAB. Ψ was determined from the behavior of the data near the origin.

For bending, the classical rigidity is $\frac{M}{\theta} = E[\frac{\pi}{4}r^4]$. The exact expression of the rigidity ratio for bending of a Cosserat elastic circular rod of radius r is:

$$\Omega = 1 + 8(\frac{\ell_b}{r})^2 \frac{(1-(\frac{\beta}{\gamma})^2)}{(1+\nu)} + \frac{8N^2}{(1+\nu)}\left[\frac{(\frac{\beta}{\gamma}+\nu)^2}{\zeta(\delta r)+8N^2(1-\nu)}\right] \tag{6.4}$$

in which $\delta = N/\ell_b$ and $\zeta(\delta r) = (\delta r)^2[((\delta r)I_0((\delta r)) - I_1((\delta r)))/((\delta r)I_0(\delta r) - 2I_1(\delta r))]$. The Young's modulus E and Poisson's ratio ν were determined from compression testing while ℓ_b, β/γ, and N were determined from fitting the full set of experimental data with Equation 6.4.

Results for torsion size effects studies are shown in Figure 6.3. Viscoelastic dispersion of the modulus cannot obtrude in the interpretation because all experiments were conducted at 1 Hz.

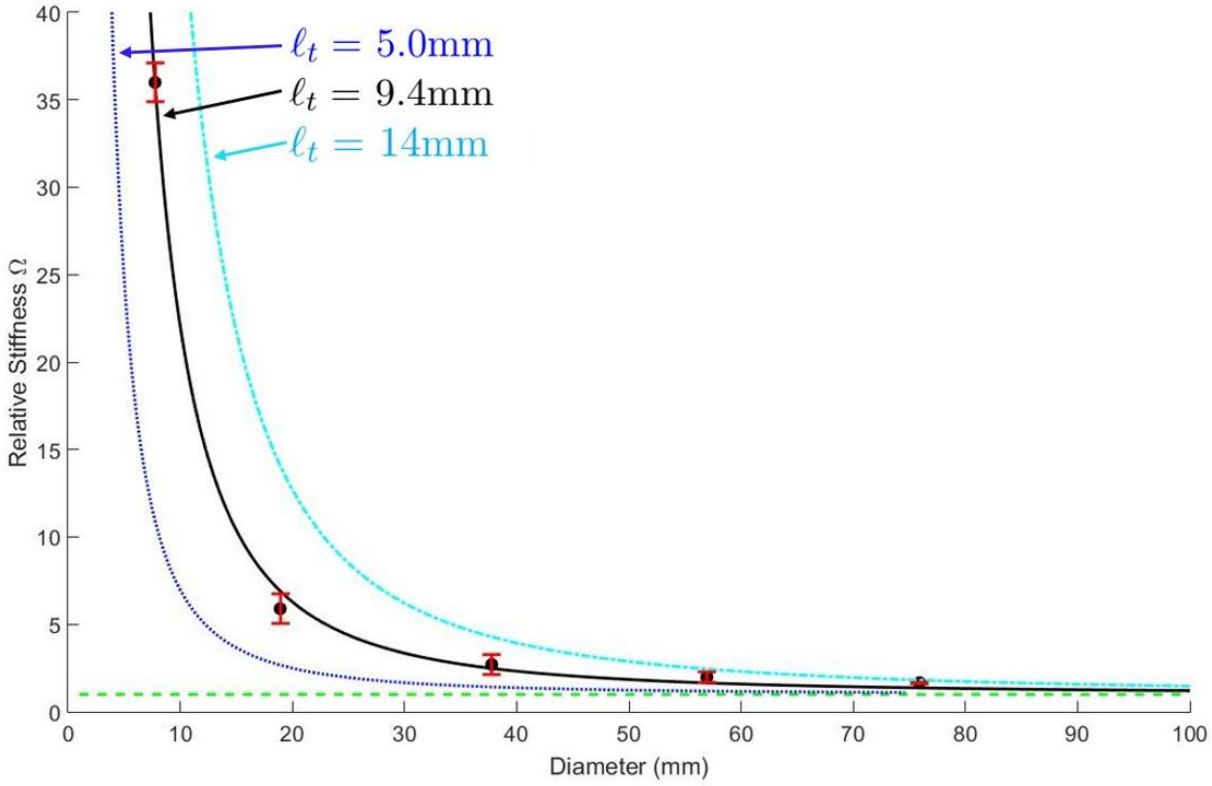

FIGURE 6.3: Size effects for lattice specimens in torsion. Points are experimental. The black curve is theoretical for best fit G = 1.1 MPa, ℓ_t = 9.4 mm, N = 1, Ψ = 1.0. Blue curves illustrate theoretical predictions for ℓ_t = 5.0 and 14 mm, respectively. Classical elasticity (ℓ_t = 0) predicts constant Ω = 1 independent of diameter which is indicated by the green horizontal dashed line.

For torsion, G = 1.1 MPa, ℓ_t = 9.4 mm, and N = 0.999. Error bars shown were calculated from noise in the signal and from uncertainties in specimen dimensions. The mean absolute percent deviation between experimental results and the Cosserat prediction was 12% while the root-mean-square deviation (RMSD) was 0.50. The increase in relative stiffness did not roll off near the origin therefore $\Psi < 1.5$. Results are consistent with $\Psi = 1$ but are not very sensitive to Ψ in this regime. The maximum size effect in torsion was Ω = 36 corresponding to a 3500% deviation from the classical prediction. The asymptotic value of G was located via curve fit. The characteristic length is comparable to the structure cell size.

The results of bending size effect studies are shown in Figure 6.4 in which E = 3.14 MPa, ν = 0.05, ℓ_b = 9.1 mm, β/γ = 0.5, N = 0.99. The mean absolute percent deviation between experimental results and Cosserat prediction was 14% while and the RMSD was 0.58. The asymptotic value for E is based on the average compression modulus corrected for the difference in frequency (0.04 Hz vs. 1 Hz) via dispersion inferred from observed damping tan $\delta \approx 0.05$. In compression there is no strain gradient. Similarly, the Poisson's ratio is the average based on compression. The maximum size effect in bending was Ω = 29.4 corresponding to a 2843% deviation from the classical prediction.

It is concluded that the response follows Cosserat elasticity not classical elasticity and that the Cosserat characteristic length is comparable to the cell size. Size effects are large in magnitude.

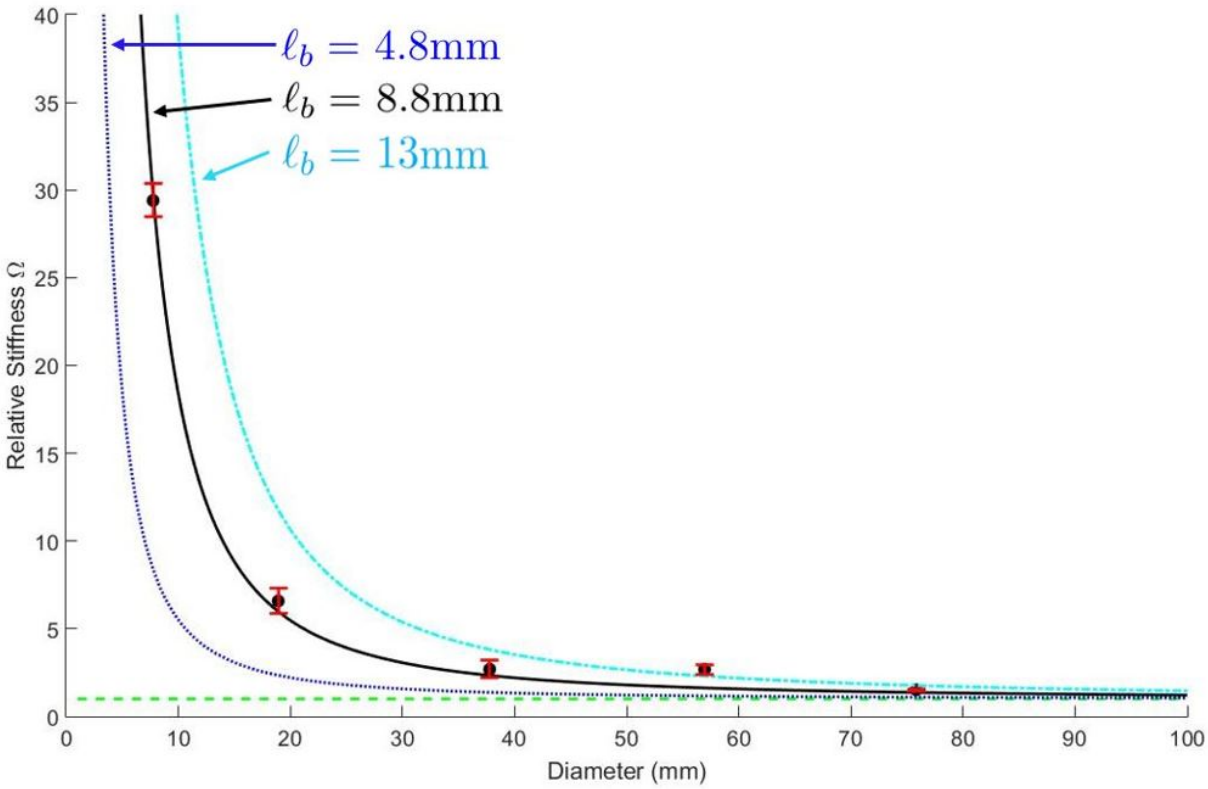

FIGURE 6.4: Size effects for lattice specimens in bending. Points are experimental. The black curve is theoretical for best fit E = 3.14 MPa, ν = 0.05, ℓ_b = 8.8 mm, β/γ = 0.5, N = 0.99. Blue and cyan curves illustrate theoretical predictions for ℓ_b = 4.8 and 13 mm, respectively. Classical elasticity predicts constant Ω = 1 independent of diameter which is indicated by the green horizontal dashed line.

Pulsed acoustic wave measurements at 60° intervals in the transverse plane and in the longitudinal direction revealed the lattice material to exhibit elastic transverse isotropy. The longitudinal modulus was lower than the transverse by a factor 1.3; the lattice does not deviate much from isotropy. No analytical solutions for Cosserat elasticity are available for anisotropic rods. Therefore, the isotropic solutions discussed above were used for interpretation and the elastic constants were interpreted as technical constants. This is analogous to materials testing in classical elasticity in which it is not always practical to incorporate a full anisotropic interpretation. Anisotropy is not a confounding variable because size effects do not occur in classical elasticity even in the

anisotropic case [82]. If need be, one may titrate the geometry of the structure to achieve elastic isotropy as has been done for negative Poisson's ratio metal foams.

A wave cut off frequency effect above 3 kHz was observed but its interpretation is equivocal. Cut off of waves can arise from structural resonance, from viscoelastic damping, or from both. In the present lattice, the wavelength at 3 kHz is about five times the cell size. Because the cells have complex structure, such a wavelength may suffice for resonance. Attenuation based on calculation from viscoelastic damping also suffices to significantly damp the waves above 3 kHz. Also, viscoelasticity contributes to wave dispersion which in non-dissipative solids could be used to infer Cosserat effects. So, for the present polymer lattice materials, the constant frequency size effect approach used here provides unambiguous interpretation, in contrast to wave methods. Periodic crystal lattices of atoms [71] with minimal attenuation, by contrast, are amenable to wave methods.

As for further comparisons, in 2-D chiral honeycomb lattices analyzed as Cosserat continua, the Cosserat characteristic lengths are similar to the cell size [50] and the Cosserat coupling number N approaches its upper limit of 1. Experiments on low density open cell polymer foams disclose substantial size effects Ω up to a factor 6.5 [73] and up to a factor 12 [80] in negative Poisson's ratio foam [61]. The characteristic length exceeded the cell size in both foams, but foams were much more compliant (E = 91 kPa for normal foam and 25 kPa for negative Poisson's ratio foam) than the present lattices (2.9 MPa).

In contrast to foams, the present lattice structure provides a path to attainment of arbitrarily large effects: the Sarrus type rib segments can be made more slender, in view of future improvements in 3D printing. Bend dominated behavior appears to be a necessary but not sufficient condition for strong Cosserat effects in cellular solids such as lattices and foams. Bend dominated behavior refers to rib deformation that occurs primarily in bending rather than compression / axial stretch. By contrast stretch dominated lattice structures with straight uniform ribs are predicted to exhibit very weak Cosserat effects [47] [48] [49]. Other lattice "metamaterials" for high strength [103] made by 3D printing [104] have been treated as classically elastic in the absence of

gradients but can be expected to exhibit Cosserat freedom; similarly lattice "metamaterials" with controllable Hall coefficient [105].

In summary, large size effects are observed in the bending and torsion of designed lattices of triangular prismatic unit cells. The size effects are inconsistent with classical elasticity but are consistent with Cosserat elasticity. Other theories of elasticity with more degrees of freedom, such as those incorporated in micromorphic/Mindlin microstructure theory [7] or microstretch elasticity [106], are not excluded; they are not necessary for the present observations.

We gratefully acknowledge support of this research by the National Science Foundation via Grant CMMI-1361832.

Chapter 7

Cosserat Elastic Lattices

The following chapter is in the submission process.

abstract 3-D printed lattices composed of strengthened diagonal and triangular prismatic unit cells with Sarrus linkage rib elements are analyzed via Cosserat elasticity. Size effects in these lattices are observed experimentally: slender specimens appear more rigid than expected classically. Magnitude of size effects is very sensitive to geometry of the lattices. Size effects observed here are much stronger than in stretch dominated lattices with uniform straight ribs.

7.1 Introduction

Continuum theories of elasticity are commonly used to model materials with microstructure, such as the lattices presented here, as continuous media. Many different continuum theories of elasticity with varying degrees of freedom exist. One of the earliest theories, the uniconstant theory, was developed by Navier [1] and incorporated only one isotropic elastic constant, a modulus. This theory was governed by the assumption that forces acted along the lines joining pairs of atoms and were proportional to changes in the distance between them. This uniconstant theory predicted a Poisson's ratio of 1/4 for all isotropic materials and was proven obsolete when experimentation disclosed a range of Poisson's ratios. The currently accepted classical theory of elasticity is a step

up in complexity and descriptive capability from Navier's uniconstant theory because it incorporates two independent isotropic elastic constants: a modulus and a Lamé constant. The classical theory of elasticity predicts Poisson's ratio to range from -1 to 1/2 for isotropic materials.

Classical elasticity is adequate for macroscopic specimens in which the structure size is many orders of magnitude smaller than the experimental size scale. Experimental tests for Cosserat elasticity at the macroscopic scale in aluminum disclosed classical behavior [25]. However, classical elasticity breaks down when the experimental length scale approaches the structural length scale of the material or structure being tested. Nonclassical effects have been observed in the bending of epoxy microcantilevers [19] and via wave dispersion in diamond crystals [26]. Additionally, neither classical elasticity nor the uniconstant theory incorporate a length scale in their definitions which is important when considering material properties such as toughness which has a length scale in its units, MPa$\sqrt{\mathrm{m}}$. The lack of a length scale prohibits either of these theories from being used to describe materials that are sensitive to strain gradients.

The Cosserat theory of elasticity [3] (with inertia terms called micropolar [9]) has even more freedom than the classical theory; Cosserat elasticity incorporates a local rotation of points and a couple stress (torque per unit area) in addition to the translation of points and force stress (force per unit area) present in classical elasticity. The physical origin of the Cosserat couple stress is the summation of bending and twisting moments transmitted by the structural elements in materials. The Cosserat local rotation corresponds to the rotation of structural elements. Forces and moments were considered in the classic analyses of foam by Gibson and Ashby [70] in which classic elastic moduli were determined; effects of rotation gradients were not considered.

The additional freedom in Cosserat elasticity is represented by its six isotropic elastic constants, $\alpha, \beta, \gamma, \kappa, \lambda$, and G. The constitutive equations for Cosserat elasticity [9] are as follows.

$$\sigma_{ij} = 2G\epsilon_{ij} + \lambda\epsilon_{kk}\delta_{ij} + \kappa e_{ijk}(r_k - \phi_k) \tag{7.1}$$

$$m_{ij} = \alpha\phi_{k,k}\delta_{ij} + \beta\phi_{i,j} + \gamma\phi_{j,i} \tag{7.2}$$

In Cosserat elasticity the stress, σ_{jk}, can be asymmetric. The resulting moment is balanced by a couple stress, m_{jk}. The antisymmetric part of the stress is related to local rotations: $\sigma_{jk}^{antisym} = \kappa e_{jkm}(r_m - \phi_m)$ in which ϕ_m is the rotation of points, called micro-rotation, e_{jkm} is the permutation symbol, and $r_k = \frac{1}{2}e_{klm}u_{m,l}$ is the macro-rotation based on the antisymmetric part of gradient displacement u_i.

On their own, the six elastic constants do not provide useful physical insight. To do so, the following technical constants have been derived from them:

$$Young's\ modulus \qquad E = \frac{G(3\lambda + 2G)}{\lambda + G} \tag{7.3}$$

$$Shear\ modulus \qquad G \tag{7.4}$$

$$Poisson's\ ratio \qquad \nu = \frac{\lambda}{2(\lambda + G)} \tag{7.5}$$

$$Characteristic\ length,\ torsion \qquad \ell_t = \sqrt{\frac{\beta + \gamma}{2G}} \tag{7.6}$$

$$Characteristic\ length,\ bending \qquad \ell_b = \sqrt{\frac{\gamma}{4G}} \tag{7.7}$$

$$Coupling\ number \qquad N = \sqrt{\frac{\kappa}{2G + \kappa}} \tag{7.8}$$

$$Polar\ ratio \qquad \Psi = \frac{\beta + \gamma}{\alpha + \beta + \gamma}. \tag{7.9}$$

There are several key consequences of Cosserat elasticity that differ from classical predictions. Circular and elliptic holes demonstrate lower stress concentration than expected classically, and small holes provide less stress concentration than larger ones [15]. Pertinent to the work presented

here, Cosserat elasticity predicts size effects in the torsion [13] and bending [23] of circular cylinders of Cosserat elastic materials. A size effect in this context is the nonclassical dependence of specimen rigidity on one or more of its dimensions. Size effects are manifested as slender cylinders appearing stiffer than predicted classically. In contrast to classical elasticity, Cosserat elasticity incorporates a length scale, manifested as characteristic lengths of bending and torsion, equations 7.6 and 7.7. Both the characteristic lengths of bending and torsion and size effects in the same modes will be explored in this work.

Cosserat elastic effects have been observed in several materials with macroscale structure. Cosserat elastic size effects in bending and torsion have been observed and measured in closed cell foams [22][23], open cell foams [107][80], and negative Poisson's ratio tetragonal lattices [108]. In each of these studies, the apparent moduli increased as specimen diameter decreased contradicting classical predictions where modulus is independent of diameter.

The Cosserat characteristic length has been determined experimentally in a two-dimensional polymer honeycomb [33] and via theoretical homogenization in straight elastic ribbed lattices [47, 48, 49]. In the latter case, the characteristic lengths were much smaller than the cell size of the lattices and the lattices behaved nearly classically. This is because these structures were stretch dominated, meaning the effects of rib extension dominate the effects of rib bending and torsion. Cosserat elastic effects depend on bending and twisting of the ribs to transmit the moments corresponding to the Cosserat couple stress. The characteristic lengths of the two-dimensional polymer honeycomb were similar to the average cell size of the material. The honeycomb material was determined to be bend dominated, meaning rib deformation occurred primarily in bending rather than compression or axial stretch. Consequently, the size effects measured were much greater than those observed in the lattice with straight elastic ribs.

Recent experimental analysis of cellular structures has demonstrated dramatic Cosserat characteristics [107] [80]. Additionally, truss lattice materials with cubic symmetry have been analytically and numerically modeled as classical media in and beyond the elastic regime via continuum

mechanics [109]. However, there is a void in experimental research for this area. The work detailed here fills the void in experimental analysis and supplements as well as balances out the abundance of analytic research. The primary purpose of this study is to compare the nonclassical phenomena of lattices with similarly designed rib structures but different unit cell shapes within the framework of linear Cosserat elasticity.

7.2 Methods

7.2.1 Materials and Experiment

The lattices detailed in each section were printed using a 3D Systems sPro 60 HS-HD selective laser sintering printer. The parent material was a polyamide simulating nylon 12. Progressively larger lattices of each type were made. Each lattice was cemented to metal end pieces to provide appropriate end conditions.

In an attempt to incorporate unique structural effects into these lattices, the ribs of each unit cell for all structure types were constructed with Sarrus linkages as shown in Figure 7.1. A Sarrus linkage is a mechanical linkage which achieves limited but exact straight line motion from a combination of flexure joints [110]. An individual linkage, or corrugation as it will be called, is characterized by high bending and torsional rigidity as compared to compressive rigidity [111]. The moduli in bending, torsion, and compression are detailed further in section 7.3.1. By incorporating these corrugations into the ribs of each unit cell, a similar effect is expected to occur in the structures which they compose. However, the relationship between rigidity in bending and torsion for the individual corrugation may not be true at the level of the unit cell or end structure. Inspiration for this structural feature was driven by results obtained for unidirectional composites incorporating segments of corrugated tubing [112], which were sensitive to strain gradients in bending and torsion. The corrugated tubing had similar relationships among bending, torsional, and compression moduli to the Sarrus linkage and resulted in structures exhibiting large Cosserat

size effects. Based on these observations, lattices incorporating strain gradient sensitive structural elements in different configurations offer potential for similar nonclassical size effects.

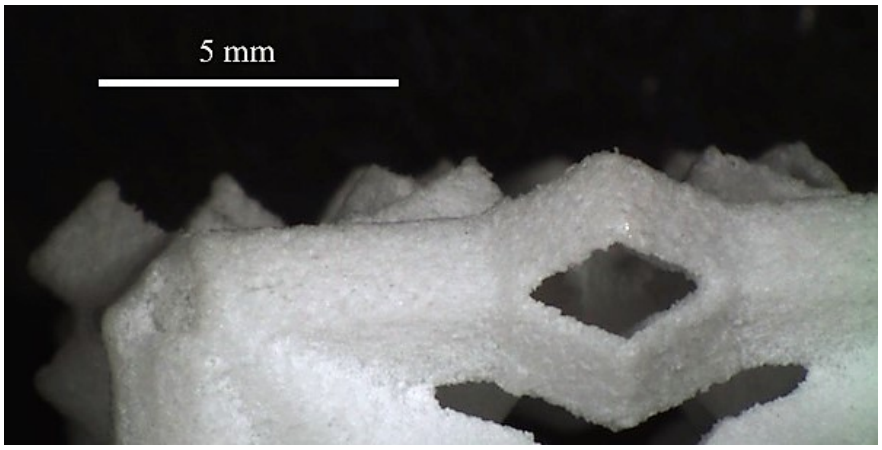

FIGURE 7.1: Four-sided Sarrus linkage created via SLS printing.

Torsional and bending rigidities for each specimen were measured using a broadband viscoelastic spectrometer (BVS). The BVS device uses a pair of orthogonal Helmholtz coils to generate a torque, either in bending or torsion, upon a magnet attached to the specimen's end piece via a ceramic stalk. The ceramic stalk was necessary because the specimens are too large to fit in the Helmholtz coils. The magnet is centered in the Helmholtz coils. Deformation of the lattices was measured by shining a laser off of a mirror cemented to the top surface of the bottom end piece of each specimen onto a four quadrant light detector. Mounting mirrors on the specimens this way was necessary to eliminate possible error from compliance of the ceramic stalk. The four quadrant light detector measures either horizontal or vertical displacement of the laser beam, depending on its setting, as a change in voltage. The light detector was calibrated prior to bending and torsion tests. Calibration was done by measuring the change in output voltage over the linear measurement regime of the detector using a precision micrometer driven calibration stage. The change in output per change in position was used as the beam calibration constant (V/μm).

Each specimen was tested using a sinusoidal signal with a frequency of 1 Hz from an SRS

Model DS345 function generator. 1 Hz was used because it is well below any resonant frequencies. By using the same frequency for all tests across all specimens, viscoelastic effects are decoupled from the size effects being probed. Torque was inferred from the voltage across a 1Ω resistor in series with the coils. The torque signal vs. angular displacement signal was displayed as a Lissajous figure on a Tektronix TDS3014B oscilloscope using DC coupling. Data points from the Lissajous figures along with dimensional measurements of the specimens were used to calculate the moduli of the specimens. Maximum strain during testing was 5×10^{-5}, well within linearity for these structures. Linearity was verified by the shape of the Lissajous figures.

Compression tests were conducted to ascertain the moduli of the specimens in the absence of macroscopic gradients of strain and rotation. This was accomplished using an Instron screw driven load frame at constant strain rate. Poisson's ratio was also calculated using compression testing by measuring transverse deformation via digital photography and micrometer.

7.2.2 Analysis and Interpretation

Size effects were interpreted within the framework of Cosserat elasticity. Specimens with hexagonal cross sections were approximated as circular and corresponding results were interpreted using exact analytical solutions for the torsion and bending of Cosserat elastic solids with circular cross sections. Exact solutions for bending and torsion of Cosserat elastic solids with square cross sections do not exist so approximate solutions were used. The analysis of materials with square cross sections is difficult because of warping - planar section do not remain in plane when the material undergoes deformation. This is in contrast to materials with a circular cross section for which warping does not occur. In both cases, isotropic solutions are used because no anisotropic solutions are available. Therefore, elastic constants obtained are technical constants. This is similar to classical elastic constants obtained from quasistatic tests such as standard tensile or compression tests in principal directions. Size effects do not occur in classical anisotropic elasticity [82], rigidity is independent of specimen size just as isotropic elasticity. Therefore, size effects are a distinct nonclassical behavior and anisotropy is not a confounding factor.

Considering elastic solids with circular cross sections, classical torsional rigidity is $\frac{M}{\theta} = G[\frac{\pi}{2}r^4]$. Cosserat torsional rigidity in the same regime is $\frac{M}{\theta} = G[\frac{\pi}{2}r^4](1 + 6(\ell_t/r)^2)$. G is the true shear modulus in the absence of gradients; M is applied moment and θ is angular displacement. This expression is exact when N = 1. For all other N the exact solution involves Bessel functions and is as follows [13]:

$$\Omega = (1 + 6(\ell_t/r)^2)[\frac{(1 - 4\Psi\chi/3)}{1 - \Psi\chi}], \tag{7.10}$$

Here, $\chi = I_1(pr)/prI_0(pr)$, $p^2 = 2\kappa/(\alpha + \beta + \gamma)$ and I_0 and I_1 are modified Bessel functions of the first kind. The constant Ψ only has an appreciable influence for very small radius specimens and was determined based on behavior of the data near the origin. The shear modulus, G, characteristic length of torsion, ℓ_t, and the coupling number N were found by fitting Eq. 7.10 to the full set of experimental data using MATLAB.

For bending of a Cosserat elastic rod with radius r, the relative rigidity ratio involving Bessel functions is:

$$\Omega = 1 + 8(\ell_b/r)^2\frac{(1 - (\beta/\gamma)^2)}{(1 + \nu)} + \frac{8N^2}{(1 + \nu)}[\frac{(\beta/\gamma + \nu)^2}{\zeta(\delta a) + 8N^2(1 - \nu)}] \tag{7.11}$$

with $\delta = N/\ell_b$ and $\zeta(\delta r) = (\delta r)^2[((\delta r)I_0((\delta r)) - I_1((\delta r)))/((\delta r)I_0(\delta r) - 2I_1(\delta r))]$. Classical bending rigidity follows $\frac{M}{\theta} = E[\frac{\pi}{4}r^4]$. Both Young's modulus, E, and the Poisson's ratio ν were calculated from compression testing. The Coupling number, N, β/γ, and the characteristic length of bending, ℓ_b, were determined by fitting the full set of experimental data with Eq. 7.11.

The procedure for analyzing and interpreting data from specimens with square cross sections is similar; different analytical solutions are used as follows. For bending of a rectangular bar of width $2a$, the rigidity ratio depends on the characteristic length and the Poisson's ratio [55]. If $\beta/\gamma = -\nu$, the rigidity ratio $\Omega = \frac{M}{1/R}\frac{1}{EI}$ is, with M as moment and R as radius of curvature,

$$\Omega = [1 + 24(\ell_b/a)^2(1 - \nu)]. \tag{7.12}$$

For other values of Poisson's ratio, the rigidity ratio is, (to fourth order in ℓ_b/a),

$$\Omega = \left[1+24\frac{1+2\frac{\beta}{\gamma}\nu+\nu^2}{1+\nu}\left(\frac{\ell_b}{a}\right)^2-480\left(\frac{\beta}{\gamma}+\nu\right)^2\frac{44-38\nu+3N^2(1-\nu)(13-9\nu)}{N^2(1+\nu)(22-19\nu)}\left(\frac{\ell_b}{a}\right)^4\right]. \quad (7.13)$$

Torsion of a square cross section Cosserat elastic bar of width $2a$ gives rise to the following relation between torque and angle. When $\kappa \to \infty$, corresponding to $N = 1$, the total torque M [90] simplifies to

$$M = \frac{4}{21}G(\frac{a}{2})^4\theta\frac{1796+126\left(449+2740\bar{\ell}^2+3960\bar{\ell}^4\right)\bar{\ell}^2+693\left(152+2280\bar{\ell}^2+6615\bar{\ell}^4\right)\bar{\ell}_b^2}{8\left(19+465\bar{\ell}^2+990\bar{\ell}^4\right)+1485\left(6+49\bar{\ell}^2\right)\bar{\ell}_b^2}. \quad (7.14)$$

in which $\bar{\ell} = 2\ell_t/a$, $\bar{\ell}_b = 2\ell_b/a$ and θ as the angular displacement per length. This solution is superior in the regime of strong coupling or for $\beta/\gamma < 0$, to that of [34], which overestimates the effects for large N.

7.3 Results and Discussion

7.3.1 3D Strengthened Diagonal Unit Cell Lattice Structures

Analytical and numerical studies have been performed on lattices made of strengthened diagonal unit cell plates as classical media [109] in and beyond the elastic regime. The strengthened diagonal (SD) unit cells were essentially face centered cubic (FCC) unit cells where the bonds between atoms were replaced with straight ribs. The lattices presented in this section use a similar unit cell but incorporate a fourfold Sarrus linkage rib element rather than a straight rib.

The Sarrus linkage rib element incorporated in these lattices were tested individually. The measured effective bending modulus of an individual rib was 281 MPa while the Young's modulus in compression was 14 MPa. The torsional modulus was measured to be 387 MPa. The ribs,

therefore, resist torsion and bending to a much greater extent than compression. These ribs were specifically designed to be sensitive to strain gradients and result in large size effects when incorporated in 3D structures. However, the complexity of the SD unit cells changes loading conditions of the rib elements so that most are not in pure bending or shear. Therefore, determination of the mechanism by which Young's modulus is governed is very difficult.

Lattices with these Sarrus linkage - SD unit cells in two different orientations are explored. A first set of lattices was created that had the SD unit cells oriented with their <111> axes parallel to the longitudinal axes of the specimens, Figure 7.2. A second set of lattices was then made wherein the unit cells were oriented such that their <100> axes were parallel to the longitudinal axes of the specimens, Figure 7.5. Both sets of lattices use identical SD unit cells.

Structures with <111> Cell Axes Parallel to Longitudinal Axis

Three progressively larger specimens were created in this orientation. Images of each specimen are shown below in Figure 7.2. The size of the smallest specimen, Figure 7.2a, was dictated by the minimum resolution of the SLS printer while the maximum specimen size 7.2c was limited by the diameter of the BVS chamber. These specimens were hexagonal in cross section but approximated as circular so the exact solutions for torsion, Eq. 7.10, and bending, Eq. 7.11, of Cosserat elastic solids could be used to analyze experimental data. The average density of this set of lattices was 0.230 g/cc.

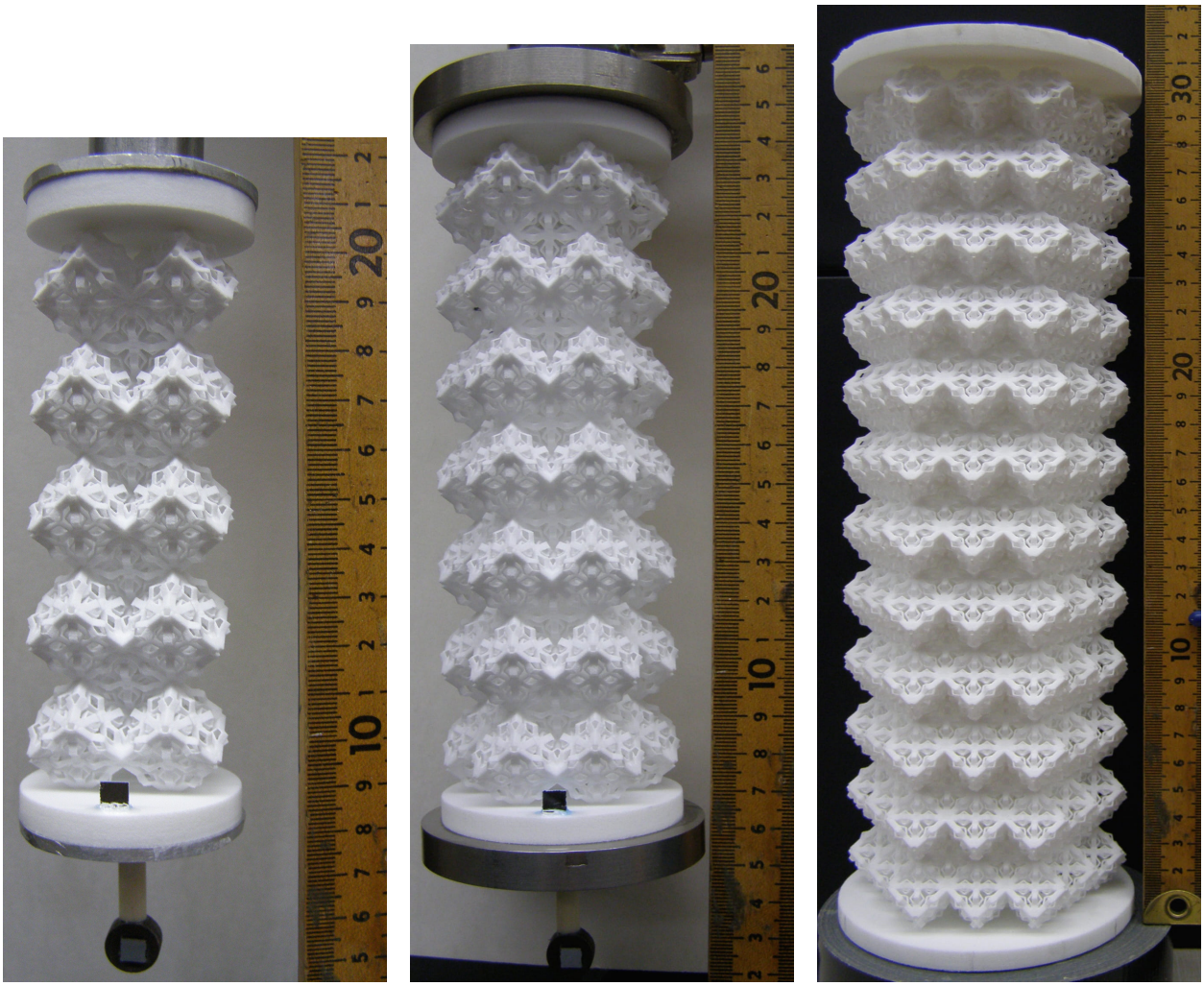

(A) Smallest specimen.

(B) Medium specimen.

(C) Largest specimen.

FIGURE 7.2: SLS printed lattices with SD cubic unit cells oriented with their <111> axes parallel to the longitudinal axes of the specimens. Scales are metric.

The results of torsion testing are shown below in Figure 7.3. For analysis, N was allowed to vary between 0 and 1, ℓ_t was restricted by thermodynamic limitations to be greater than 0 mm, and the asymptotic shear modulus was restricted to values greater than 0 Pa. Since no roll off occurred for small sizes, the fit was insensitive to Ψ, although best fit occurred for Ψ = 1.5. The

best fit yielded the following results: ℓ_t = 6.0 mm, G = 3.9 MPa, N = 1.0, and Ψ = 1.5. The goodness of fit was R^2 = 0.99. The maximum size effect in torsion was Ω = 2.8.

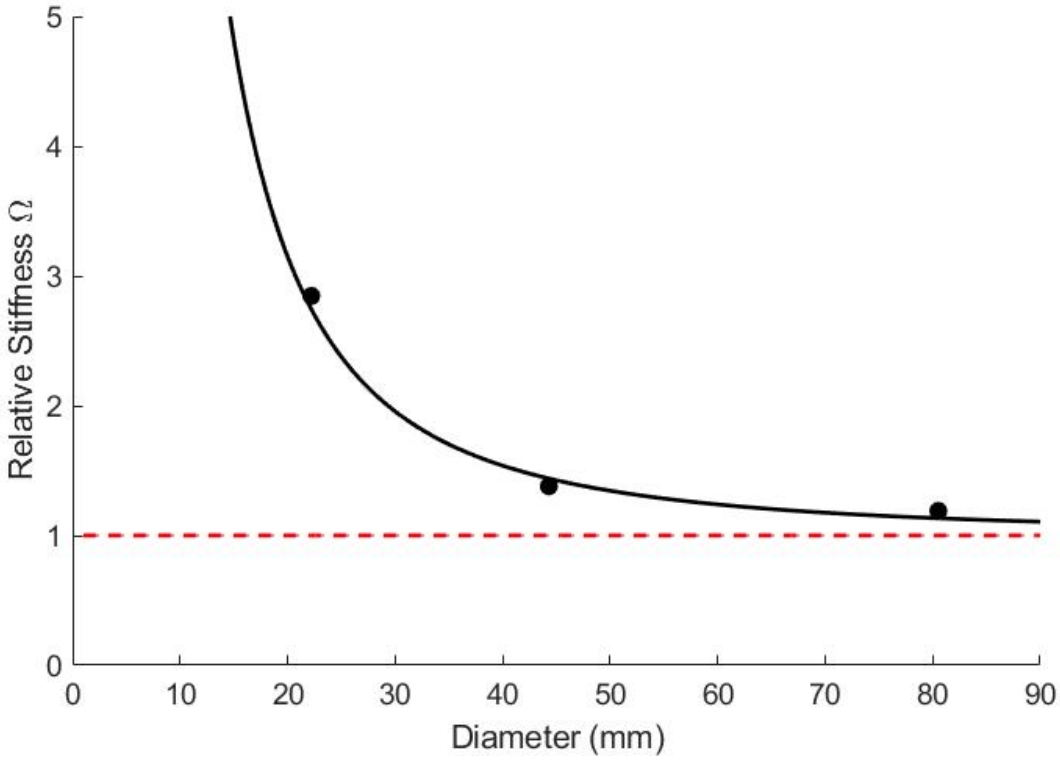

FIGURE 7.3: Size effects in torsion for specimens composed of SD unit cells with their <111> axes parallel to specimen axes. Points are experimental. Curve is theoretical for ℓ_t = 6.0 mm, G = 3.9 MPa, N = 1.0, and Ψ = 1.5. Fit is insensitive to Ψ because no roll off occurs at small sizes. Classical elasticity predicts Ω independent of diameter as illustrated by the red dashed line.

Analysis of bending size effects are shown in Figure 7.4.

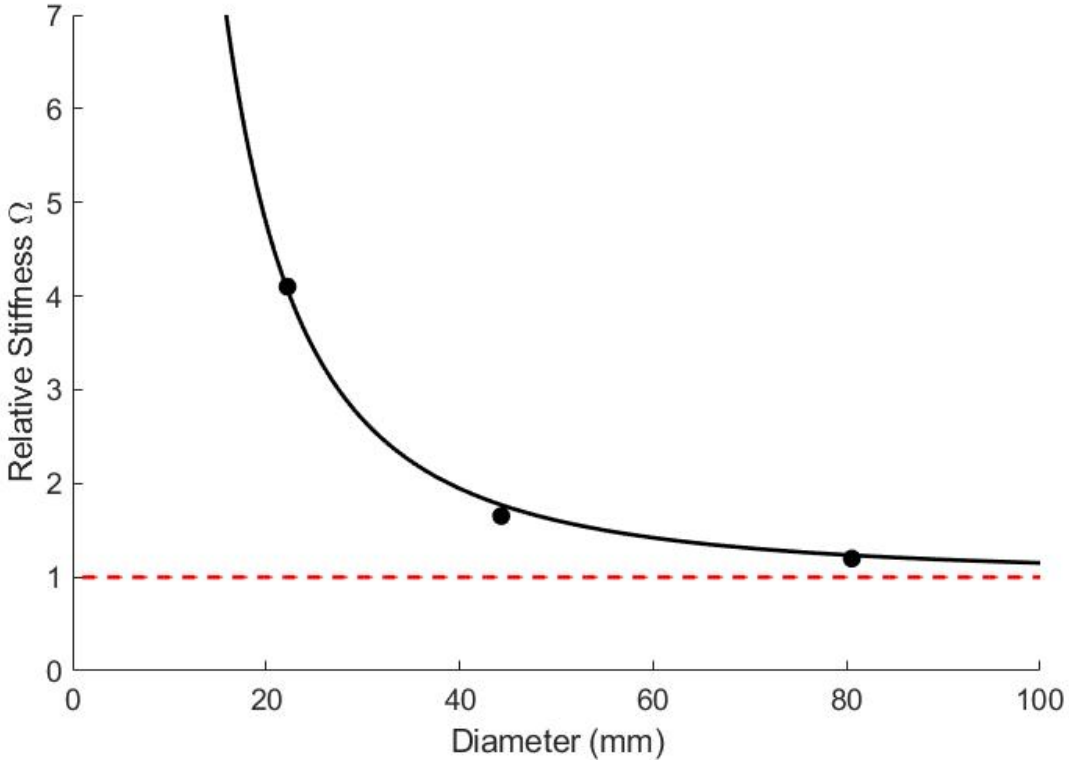

FIGURE 7.4: Size effects in bending for specimens composed of SD unit cells with their <111> axes parallel to specimen axes. Points are experimental. Curve is theoretical for ℓ_b = 8.2 mm, E = 6.0 MPa, N = 1.0, and β/γ = 0. Classical elasticity predicts Ω independent of diameter as illustrated by the red dashed line.

Fitting was accomplished using the asymptotic bending modulus, 6.0 MPa, determined from compression testing and the coupling number, N, from torsion of 1.0. β/γ and ℓ_b were free to vary from -1 to 1 and greater than 0, respectively. Best fit resulted in the following: β/γ = 0 and ℓ_b = 7.82 mm. The correlation coefficient of this fit was R^2 = 0.995. The maximum size effect in bending was Ω = 4.1. Although the structures are approximately hexagonal in cross section, they have cubic symmetry because they are composed of SD unit cells. Due to this configuration, they are elastically anisotropic. Therefore, the characteristic length of torsion in independent from the characteristic length of bending. Also due to anisotropy, the coupling number from torsion is not necessarily applicable to bending results. However, N calculated from torsion led to the best fit

results for bending.

Currently, there is no known analysis available for lattices of this construction. However, as mentioned earlier, several cellular materials have been analyzed as Cosserat continua. Several lattices with straight ribs [47, 48, 49] have been theoretically homogenized and had their Cosserat elastic constants extracted. These lattices were stretch dominated and, consequently, the characteristic lengths were much smaller than the average cell size. Experimental analysis of 2D chiral honeycomb lattices as Cosserat continua revealed bend dominated behavior. Consequently, the characteristic lengths were approximately the same as the average cell size and the coupling number approached the upper bound of 1. Based on these relationships, the present lattices are bend dominated because the ratio of characteristic lengths to average cell size exceeds that of stretch dominated materials and the coupling number approaches the upper bound of 1.

In summary, nonclassical size effects are observed in torsion and bending for lattices of SD unit cells aligned in the <111> direction. The maximum size effect of 2.8 and 4.1 for torsion and bending, respectively, are significant deviations from classical predictions. These size effects are consistent with Cosserat elasticity. The lattices are bend dominated based upon the ratio of characteristic lengths to average cell size and coupling number.

Structures with <100> Cell Axes Parallel to Longitudinal Axis

Four progressively larger specimens were created for this orientation. Because of the orientation of the unit cells, it was possible to create a specimen of only one unit cell in cross section. The largest specimen size was dictated by the dimensions of the BVS chamber. Images of each specimen are shown below in Figure 7.5. The average density of this set of lattices was 0.201 g/cc. Since these specimens have square cross sections, equations 7.13 and 7.14 were used to analyze experimental data gathered from bending and torsion, respectively.

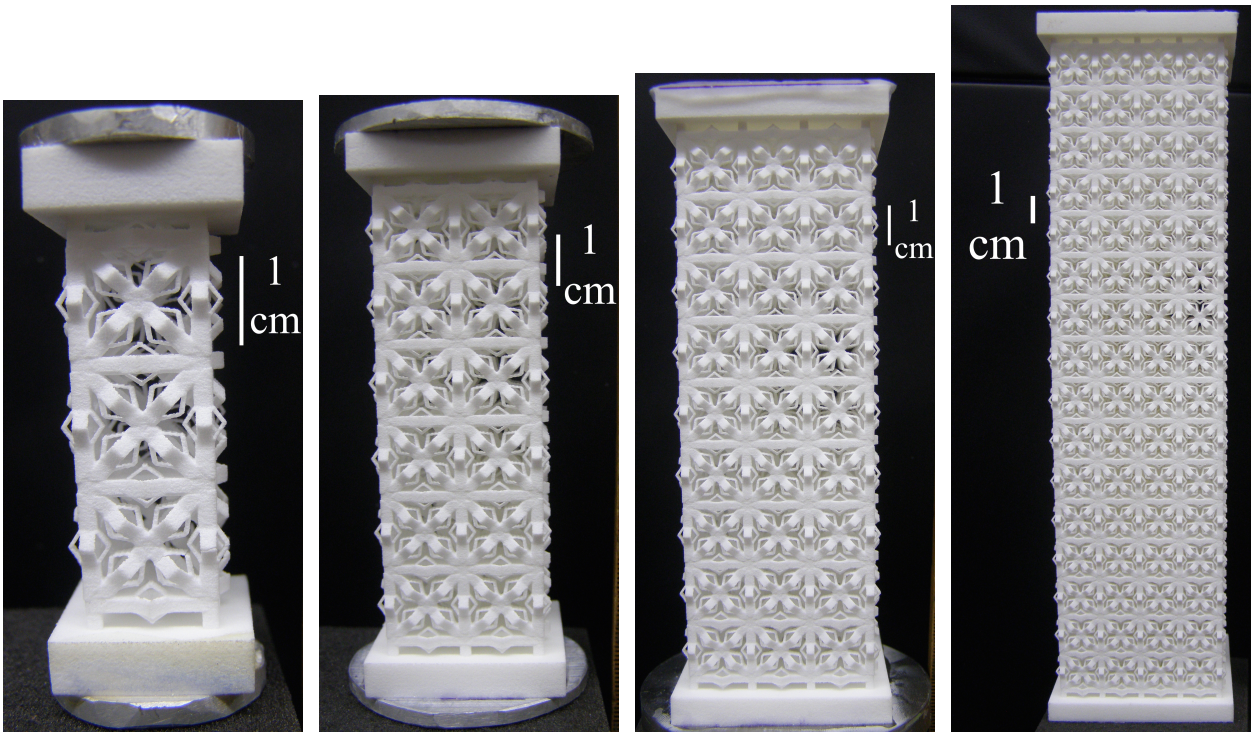

(A) 1x1x3 (B) 2x2x6 (C) 3x3x9 (D) 4x4x12

FIGURE 7.5: SLS printed lattices with SD cubic unit cells oriented with their <100> axes parallel to the longitudinal axes of the specimens. Dimensions in subcaptions are number of unit cells in cross section by number of unit cells in height.

Compression testing disclosed E = 9.64 MPa, largely independent of specimen side length. Bending test results are shown in Figure 7.6, assuming the asymptotic bending modulus to be that found in the compression test of 9.64 MPa. Best fitment yielded: ℓ_b = 7.4 mm, β/γ = 0.028 and N = 0.23. The correlation coefficient was R^2 = 0.88. For comparison with the lattices from the previous section, a second fit was performed using N = 1. The resulting R^2 was 0.32.

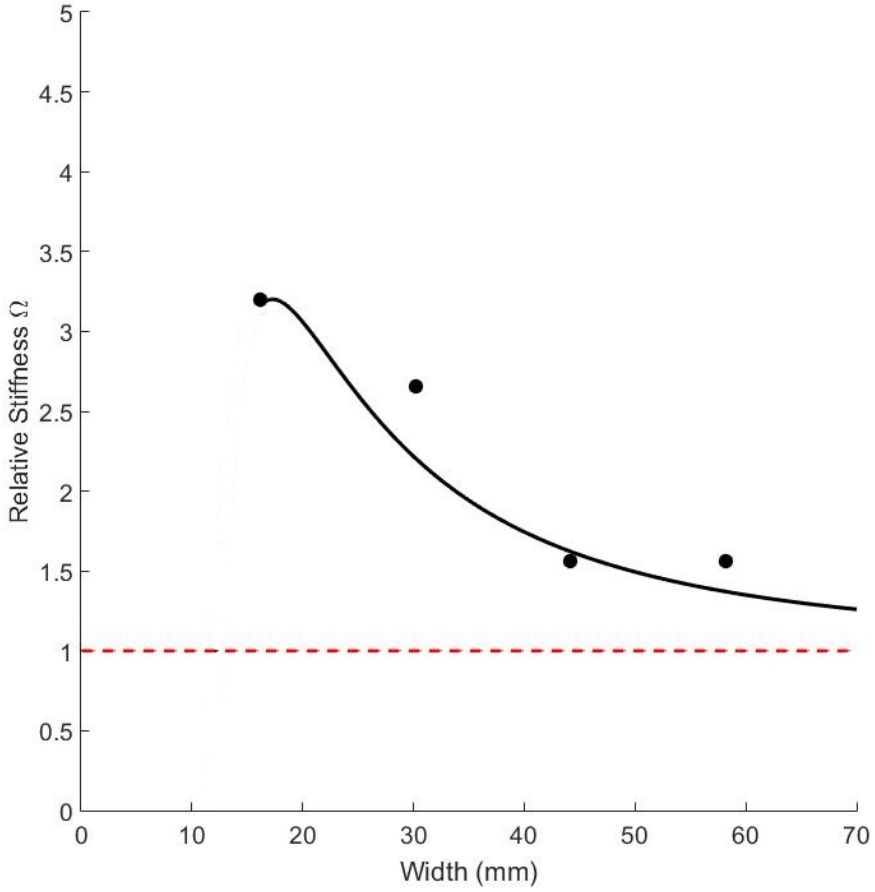

FIGURE 7.6: Size effects in bending for specimens composed of SD unit cells with their <100> axes parallel to specimen axes. Points are experimental. Curve is theoretical for ℓ_b = 7.4 mm, E = 9.64 MPa, N = 0.23, and β/γ = 0.28. The red dashed line illustrates the relationship of rigidity to specimen diameter of classical elasticity; the two are independent.

The roll off near the origin is due to the second term in the approximate solution, Eq. 7.13, dominating at small side length values when $\beta/\gamma \neq -\nu$, especially when N is small as it is in this case. After the roll off at the smallest point, the theoretical model predicts a sharp decrease in rigidity This phenomenon is likely due to the approximate solution being a two-term approximation. If more terms were used, stability near the origin is expected to increase. However,

prediction of rigidity at sizes smaller than the smallest structural element, which in this case is an individual unit cell, is nonsensical and can be ignored. Additionally, the function, 7.11, has a very flat landscape across fitment such that there are a range of values for the coupling number, N, and β/γ, that achieve a very similar goodness of fit.

Results for torsion size effect studies are shown below in Figure 7.7. The only available solution for torsion of a square bar of Cosserat elastic material, Eq. 7.14, used here, is specifically for the case $N = 1$. For analysis, thermodynamic restrictions were placed on the boundaries of the characteristic length of torsion, ℓ_t, and bending, ℓ_b to be greater than 0 mm. The asymptotic shear modulus, G was limited to values greater than 0. Best fit results, assuming $N = 1$ in torsion, are as follows: G = 4.3 MPa, ℓ_t = 3.8 mm, and ℓ_b = 3.3 mm. The goodness of fit was R^2 = 0.856.

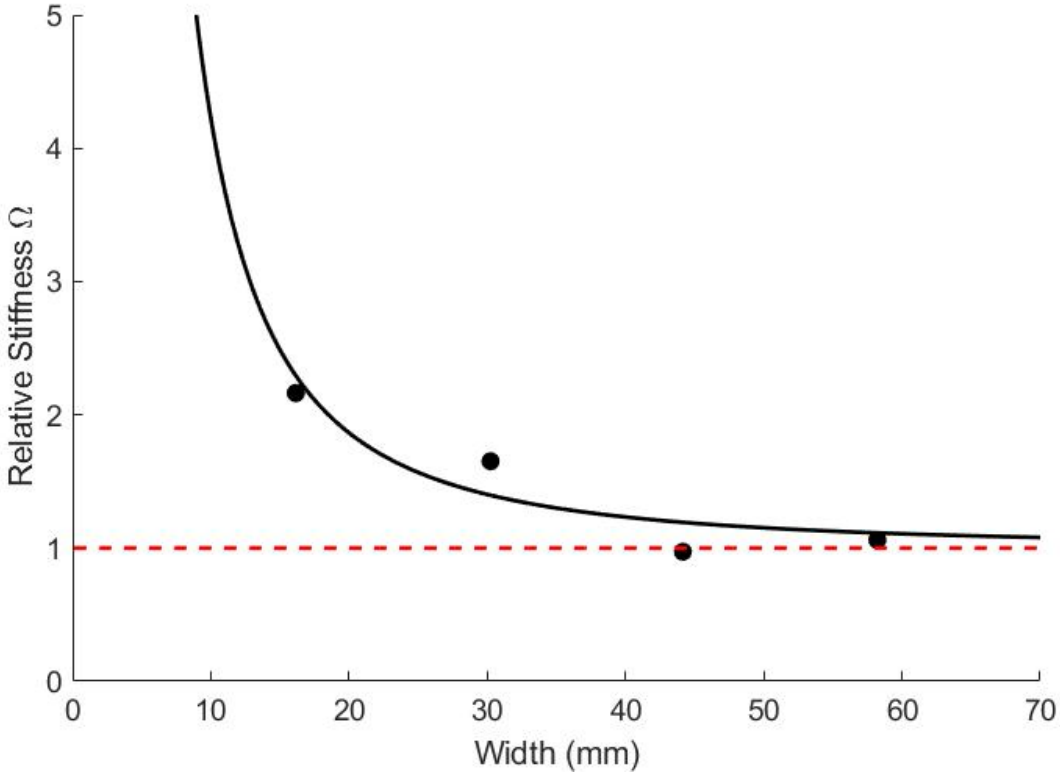

FIGURE 7.7: Size effects in torsion for specimens composed of SD unit cells with their <100> axes parallel to specimen axes. Points are experimental. Curve is theoretical for $N = 1$, $\ell_t = 3.8$mm, $\ell_b = 3.3$ mm, and $G = 4.3$ MPa. Classical elasticity predicts Ω independent of diameter as illustrated by the solid red line.

An interesting point to note is that the characteristic length of bending calculated from torsion is much different than calculated from bending. The apparent discrepancy is due to two primary factors. The first is that specimen anisotropy means that results from the two fitting equations can be independent. Second, the torsion equation is very weakly dependent on ℓ_b and much more strongly dependent on ℓ_t when determining best fit. The difference in R^2 between the best fit shown in Figure 7.7 with $\ell_b = 3.3$ mm and the best fit with $\ell_b = 7.4$ mm from the bending fitment, all other parameters held constant, is only 0.0003. Additionally, Eq. 7.13 was created for the limiting case $N = 1$. A good fit was achieved with this restriction, but better results may be possible for

other values of N. However, only solutions for very small values of N and N = 1 are currently available.

The SD unit cell has cubic symmetry. Therefore, an individual unit cell is isotropic in the principal directions but structurally anisotropic. The modulus in the <111> direction does not need to equal the modulus in the <100> direction. Indeed E from compression, in which there are no gradients, was 9.64 MPa for <100> and 6.0 MPa for <111>. The relationship between the asymptotic shear modulus and asymptotic bending modulus determined for these lattices is nearly classical elastically isotropic, following $E = 2G(1 + \nu)$. However, for a structurally cubic material, there are three independent classical constants and the isotropic relationship does not need to hold. The behavior found here is due to the complexity of the geometry and associated load distribution.

In summary, nonclassical size effects are observed in torsion and bending of lattices composed of SD unit cells oriented with their <100> axes parallel to the specimens longitudinal axes. These size effects are consistent with Cosserat elasticity. The characteristic length of bending was 7.4 mm and the characteristic length of torsion was 3.8 mm. The largest size effects in torsion and bending were Ω = 2.2 and 3.3, respectively.

7.3.2 Triangular Prismatic Unit Cell Structures

The complexity of the SD unit cells, composed of Sarrus linkage rib elements, made identification of deformation mechanisms difficult. Without 45° cross ribs on each face, stronger gradient effects via decoupling were hypothesized. To eliminate structural complexity and ease identification of deformation mechanisms, a second unit cell and subsequent series of structures was created. The unit cell used in these two series of structures is a triangular prismatic unit cell. These unit cells are much simpler in design than the SD unit cells and are expected to exploit the properties of the individual rib element to a greater degree. A magnified image of this configuration is shown in Figure 7.8.

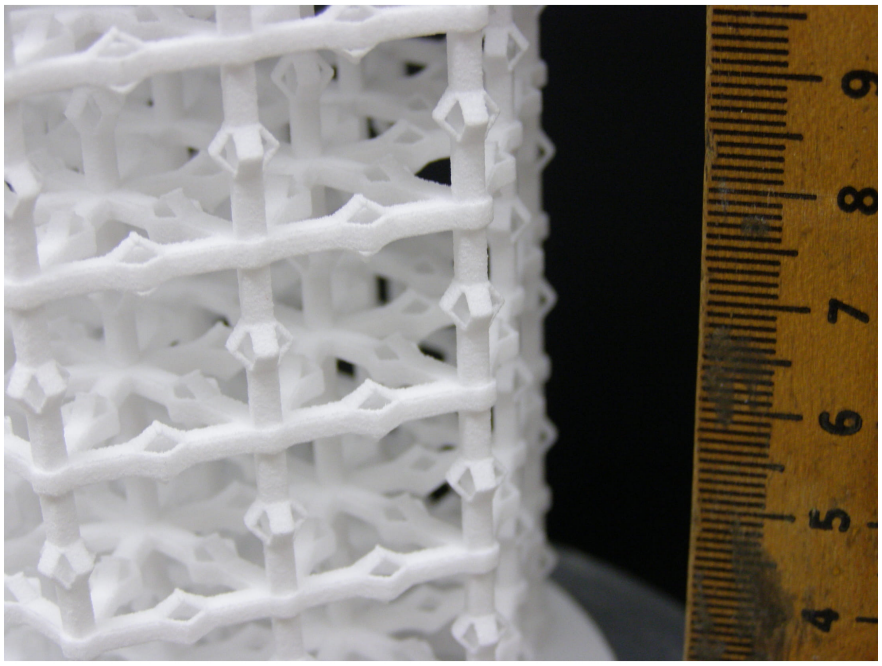

FIGURE 7.8: A close-up view of the 3-D printed triangular prismatic unit cell configuration. This is the long rib (14 mm) configuration. Scale is metric.

Long Rib Triangular Unit Cell Structures

The first set of lattices made using the triangular prismatic unit configuration are presented in this section. These unit cells were made of rib elements the same length as those in the SD unit cells of previous sections. The ribs were 14 mm long and an image of the structure is shown in Figure 7.8. The smallest specimen was limited to one unit cell in cross section while the largest specimen was governed by the height of the BVS chamber. The specimens tested in this series are shown in Figure 7.9. The cross section of the larger specimens were hexagonal while the cross section of the smallest specimen was triangular. All specimens were approximated as circular so that the exact solution for Cosserat torsion and bending of elastic materials with circular cross section, Eq. 7.10 and Eq. 7.11, could be used. The average density for these lattices was 0.093 g/cc.

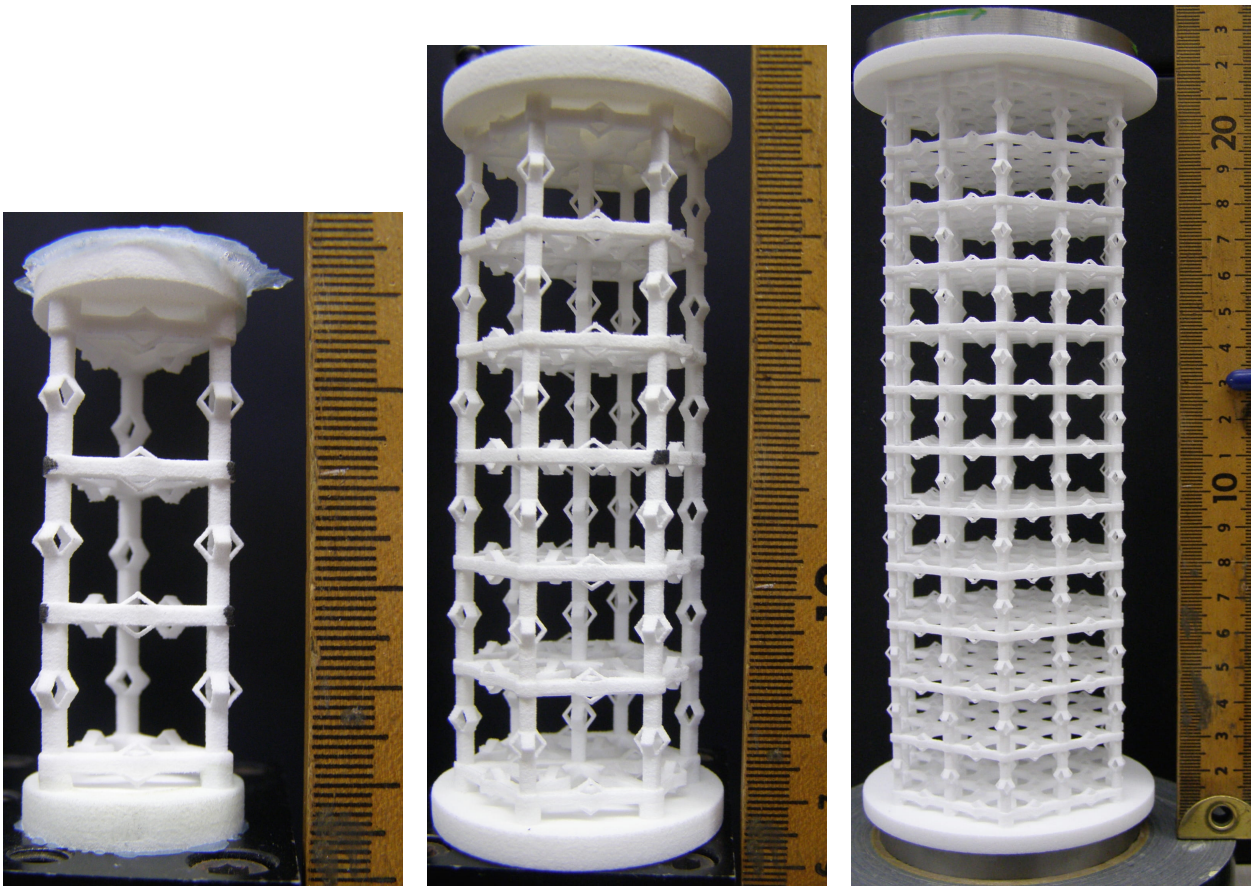

(A) Smallest specimen.

(B) Medium specimen.

(C) Largest specimen.

FIGURE 7.9: Lattices composed of long triangular prismatic unit cells.

The results of torsion testing are shown below in Figure 7.10. For the analysis, asymptotic G was allowed to vary between 0 and 0.53, which was the smallest shear modulus of the structures tested, N varied from 0 to 1, Ψ was set to 1.5, and ℓ_t was allowed to be any value greater than 0. The best fit resulted in G = 0.34 MPa, ℓ_t = 8.9 mm, and N = 1.0. R^2 was 0.9988.

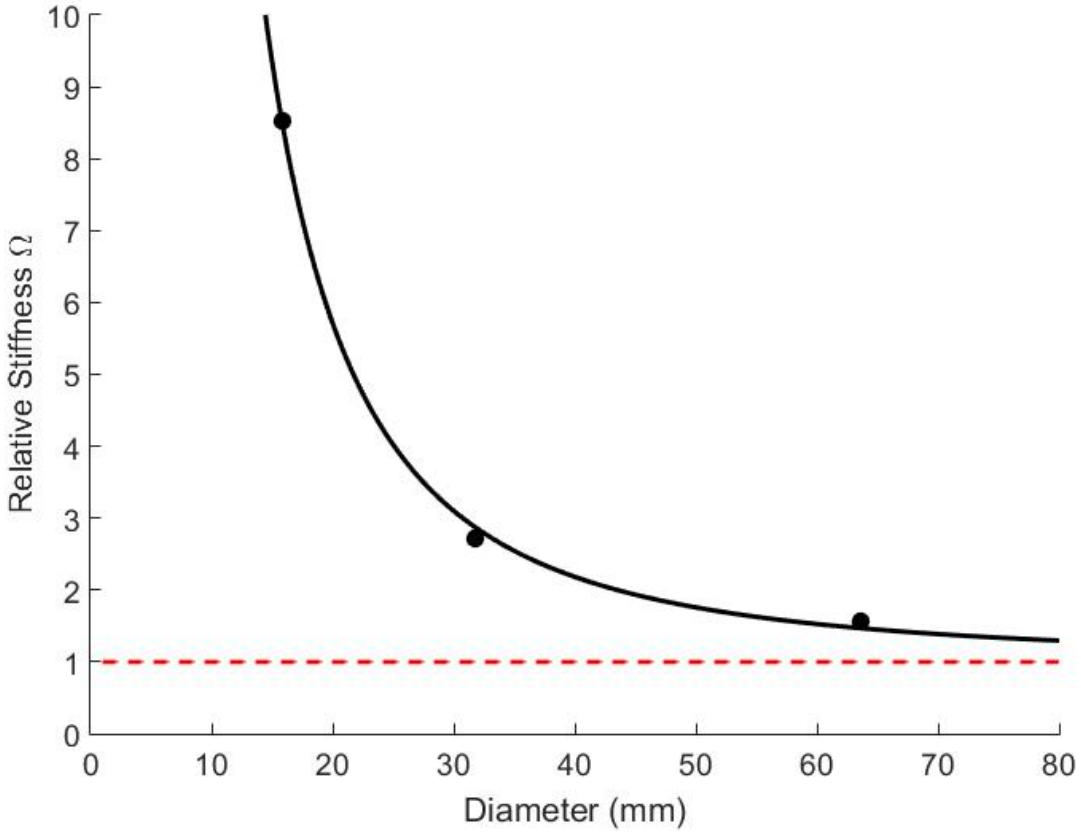

FIGURE 7.10: Torsion size effect for long triangular unit cell structures. Points are experimental and black line is theoretical best fit for G = 0.34 MPa, Ψ = 1.5, ℓ_t = 8.9 mm and N = 1.0. R^2 = 0.9988. The dashed red line illustrates the classical predicted relationship between rigidity and specimen size.

The results of bending size effect studies are shown in Figure 7.11. The modulus determined from compression testing, E = 2.3 MPa, was used as the asymptotic bending modulus. Poisson's ratio, determined by high resolution digital photography during compression testing, was ν = 0.05$\pm$0.06. The Poisson's ratio was calculated at 60 degree intervals about the longitudinal axis and averaged since the specimens had hexagonal symmetry. Limitations on variables for fitting are as follows: N varied between 0 and 1, β/γ was free to vary from -1 to 1, and ℓ_b was limited to values greater than 0. The best fit disclosed N = 0.99, β/γ = 0, and ℓ_b = 13.2 mm, resulting in R^2 =

0.9719.

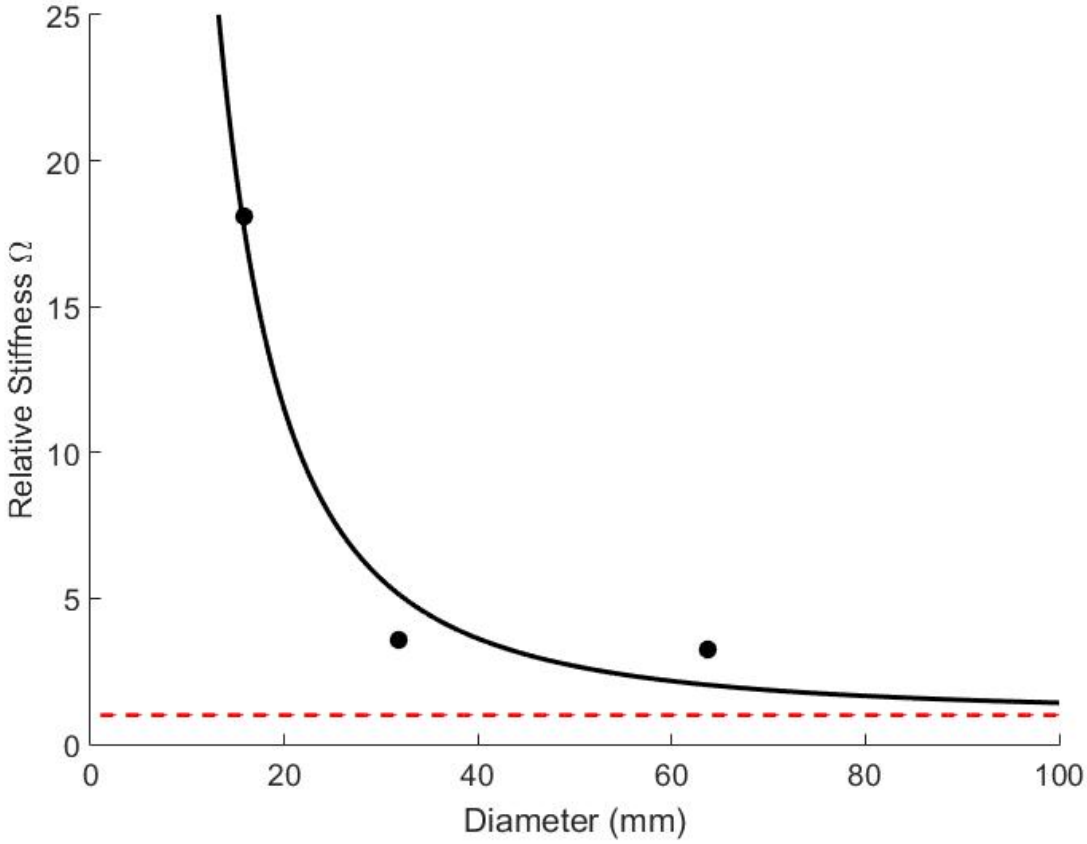

FIGURE 7.11: Bending size effects for long triangular unit cell structures. Points are experimental and black line is theoretical best fit for E = 2.3 MPa, ν = 0.05, ℓ_b = 13.2 mm, β/γ = 0, and N = 0.99. Correlation coefficient, R^2 = 0.9719. The red dashed line illustrates the classical independence of rigidity to specimen diameter.

As for comparisons with previous specimens and results, these lattices share more similarities with bend dominated 2D chiral honeycomb lattices [**Mora**] than stretch dominated straight rib lattices [47, 48, 49]. For torsion and bending, the coupling number hits and approaches the upper bound of 1, respectively. In torsion, the characteristic length was smaller than the average cell size but exceeded the relationship of characteristic length to cell size in stretch dominated straight rib lattices [49]. In bending, the characteristic length was approximately the same as the average

cell size, just as 2D chiral honeycomb lattices demonstrate [**Mora**]. Due to the relationship of characteristic lengths to average cell size and the magnitude of the coupling number, these lattices are bend dominated.

Nonclassical size effects are clear in both torsion and bending of these structures. However, confidence in fitting parameters could be increased with additional specimens. Unfortunately, the height of the BVS chamber coupled with the configuration of these specimens and the length of the ribs limited the number of specimens to three with complete cells.

Visual analysis of the specimens in torsion and bending by hand revealed deformation induced tilt of the rib elements from the nodes connecting ribs together rather than deformation in the corrugation. Recalling the relationship between torsional and bending moduli for an individual rib element were 387 MPa and 281 MPa, respectively, the opposite relationship is found in these lattices: the bending moduli are significantly larger than those in torsion. This phenomenon may be due to the minimized effect of the corrugations due to long rib length and the presence of deformation induced tilt of the ribs.

Both the confidence of best fit parameters and corrugation dominated deformation may be remedied by using short rib elements while keeping the corrugations the same size such that the corrugations become the majority of the overall structural element length. Shorter rib elements would allow for more specimens to be created and fit inside the BVS for testing. Reducing the length of the rib portion of the elements would most likely force deformation to occur in the rib elements rather than the nodes joining elements. This may lead to structures behaving more closely to individual structural elements.

In summary, size effects are observed in the torsion and bending of lattices composed of triangular prismatic unit cells with 14 mm rib elements. The size effects are consistent with Cosserat elastic predictions and cannot be explained via classical elasticity. This lattice revealed characteristic lengths smaller than the cell size; for torsion, considerably smaller. The characteristic lengths were nonetheless considerably larger than would be expected from a fully stretch dominated lattice. To achieve stronger effects, a further lattice was designed with shorter ribs to maximize the

influence of the Sarrus segment. Shorter ribs also permit a wider range of specimen sizes to be made and accommodated within the test instrument. Results for this lattice are presented in the following section.

Short Rib Triangular Prismatic Unit Cell Structures

The construction of these lattices was driven by the observation of deformation induced tilt of the ribs in torsion and bending of the long rib triangular prismatic unit cell structures. By shortening the rib portions of the structural elements and keeping the corrugation region constant, the effects of the corrugations were expected to govern the behavior of the lattices to a stronger degree. The new structural elements here were 8 mm long compared to 14 mm long in the previous set of lattices. Including hexagonal nodes, the cells were approximately 10.5 mm long on each side of the triangular base and 9.0 mm tall. A magnified image of one such lattice is shown in Figure 7.12. The full results and analysis of these structures were published in a companion paper [111].

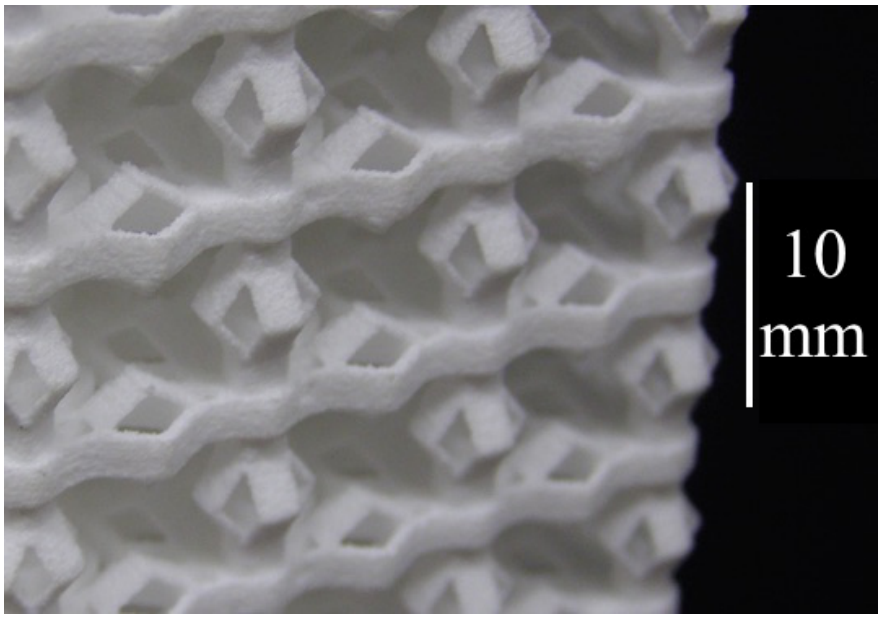

FIGURE 7.12: A close-up view of the short rib 3-D printed triangular prismatic unit cell configuration [111].

By shortening the rib portions of the structural elements, more specimens were able to be created that would fit inside the BVS for testing. The smallest specimen was one unit cell in cross section and four more incrementally larger specimens were created, all with approximately the same aspect ratio of 3:1. The smallest specimen is shown as an inset in Figure 7.13 and the largest specimen is shown as an inset in Figure 7.14. The average density of these lattices was 0.212 g/cc.

Determination of Cosserat technical constants was accomplished by fitting experimental data from torsion and bending experiments using the exact solutions for torsion and bending of Cosserat elastic materials with circular cross section. To use these models, the lattices presented here were approximated as circular in cross section.

Results for torsion size effect studies are shown in Figure 7.13. Points are experimental and the curves are theoretical fits. The black curve is the theoretical best fit while the other two curves illustrate the effects of changing characteristic length of torsion on the resulting fit. Since no roll off occurs for small specimens $\Psi < 1.5$. Best fit occurred when Ψ = 1.0, but the results were not sensitive to Ψ in this regime. The remaining best fit parameters were G = 1.1 MPa, ℓ_t = 9.4 mm, and N = 0.999. The mean absolute percent error (MAPE) between experimental results and Cosserat prediction was 12%. Error bars were calculated from noise in the signal and uncertainty in specimen dimensions. The largest size effect in torsion was Ω = 36.

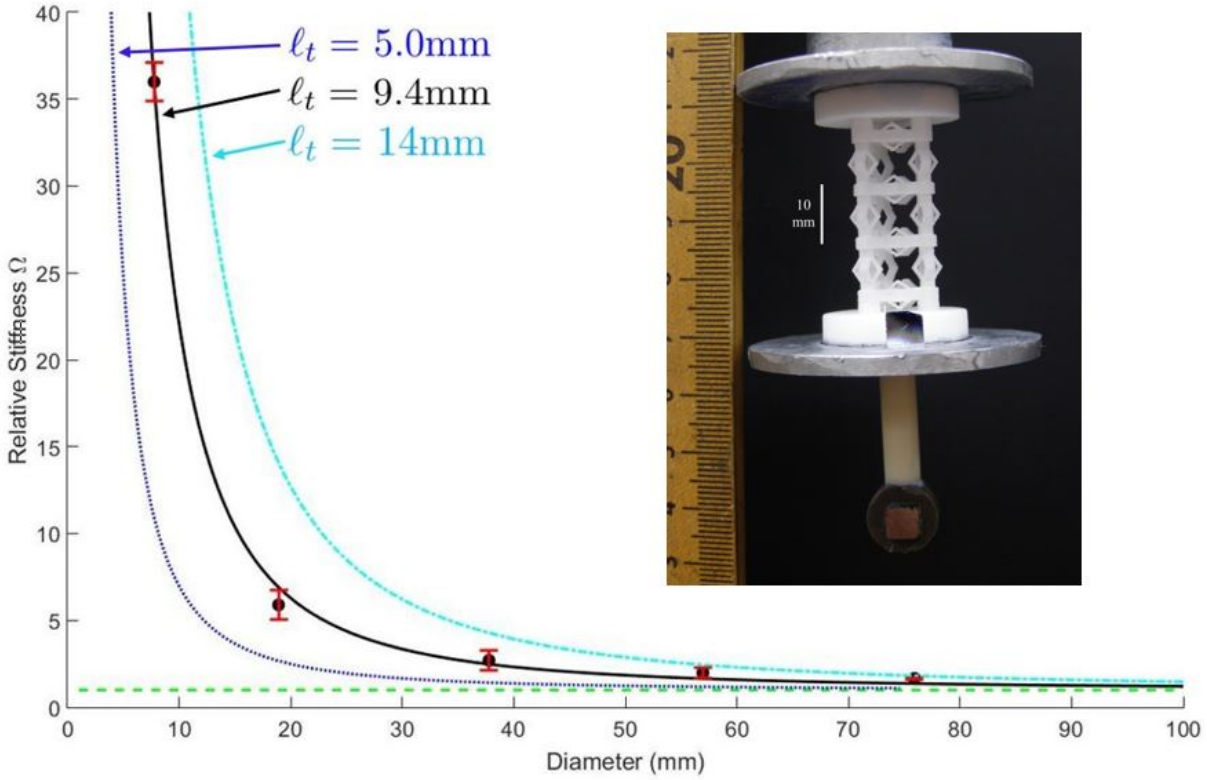

FIGURE 7.13: Size effects for short rib triangular prismatic unit cells in torsion. Black line is theoretical best fit for G = 1.1 MPa, ℓ_t = 9.4 mm, N = 1, and Ψ = 1.0. Blue and cyan curves are the theoretical models for ℓ_t = 5.0 and 14 mm, respectively. The green dashed line is the classically predicted relationship between rigidity and specimen size. The inset figure is the smallest specimen of this series. [111]

Results for bending size effect studies are shown in Figure 7.14. The asymptotic bending modulus and Poisson's ratio were calculated from compression testing and were E = 3.14 MPa and ν = 0.05. Points are experimental and the curves are theoretical fits. The black curve is the theoretical best fit for the experimental data and corresponds to E = 3.14 MPa, ν = 0.05, ℓ_b = 8.8 mm, β/γ = 0.5, and N = 0.99. The MAPE between experimental data and Cosserat prediction was 14%. The largest size effect in bending was Ω = 29.4. Blue and cyan curves illustrate the effects of changing the characteristic length of bending on the resulting fits all other parameters kept constant. The blue curve is for ℓ_b = 4.8 mm and the cyan curve is for ℓ_b = 13 mm. The green dashed line is the

classical relationship between rigidity and specimen size. Error bars were again calculated from signal noise and specimen dimension uncertainty.

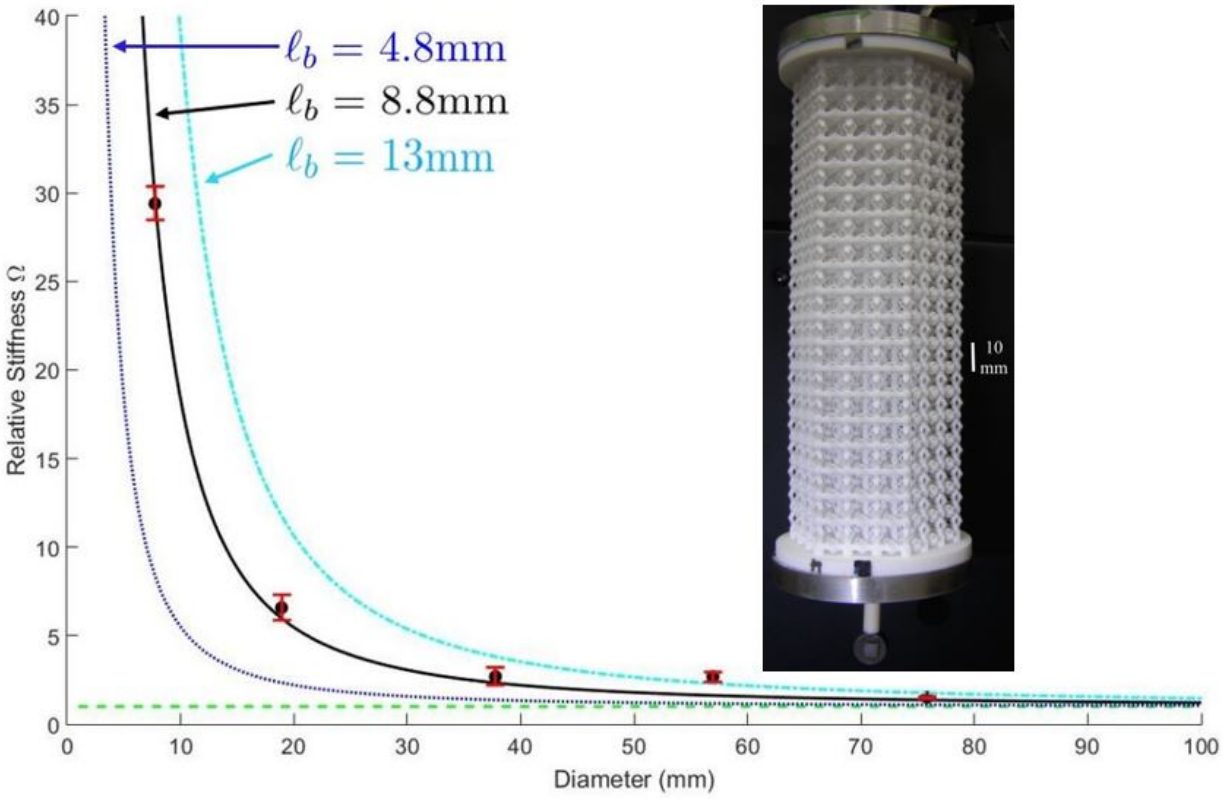

FIGURE 7.14: Size effects for short rib triangular prismatic unit cells in bending. Black line is theoretical best fit for E = 3.14 MPa, ν = 0.05, ℓ_b = 8.8 mm, β/γ = 0.5, and N = 0.99. Blue and cyan curves are the theoretical models for ℓ_b = 4.8 and 13 mm, respectively. The green dashed line is the classically predicted relationship between rigidity and specimen size. The inset figure is the largest specimen of this series. [111]

These specimens exhibit characteristic lengths approximately the same as the average cell size. Also, the coupling number, N, in torsion and bending were 1.0 and 0.99, respectively. This behavior similar to that observed in bend dominated chiral 2D honeycomb lattices. Up to this point, all cellular lattices demonstrating large size effects have been bend dominated. It seems that bend

dominated behavior is a necessary but insufficient characteristic for strong Cosserat elastic behavior in cellular materials.

Shortening the rib segments on the structural elements from the long rib lattices in the previous section has a profound effect on the size effects. Specifically, the magnitude of size-dependent stiffening is much greater - a factor of more than 35 in torsion here compared to a factor of 8.5 for the long rib lattices. Incorporating strain-gradient sensitive structural elements, such as these Sarrus linkage elements, provide a path to the attainment of large Cosserat size effects. As 3D printing technology increases in capability and structural elements such as these can be made more slender to further enhance the difference in torsion, bending, and compression moduli, larger size effects may be possible.

In summary, large size effects were observed in torsion, $\Omega = 36$, and bending, $\Omega = 29.4$, of small triangular prismatic unit cells. These results are inconsistent with classical elasticity but predicted to occur in Cosserat elasticity. Cellular material demonstrating large size effects consistent with Cosserat elasticity seem to require bend dominated behavior, among other factors. Incorporating strain gradient sensitive structural elements into 3D printed cellular lattices provides a path to the attainment of arbitrarily large size effects pending advancements in 3D printing technology.

7.4 Conclusions

Size effects were observed in four series of 3D printed cellular lattices incorporating strain gradient sensitive structural elements. A comparison of important parameters can be seen in Table 7.1. These size effects are inconsistent with classical elasticity but can be modeled via Cosserat elasticity. The largest size effects occurred in the small triangular prismatic unit cell lattices. The magnitude of the size effects depends sensitively on the geometry of the structures. Bend dominated behavior seems to be a necessary but insufficient characteristic for large Cosserat size effect in cellular structures. Additive manufacturing through methods such as those used here provide a path to the attainment of arbitrarily large size effects.

TABLE 7.1: Summary of important parameters from aforementioned lattices.

Lattice Type	Ω_T	Ω_B	Avg. Cell Size (mm)	ρ $(\frac{g}{cc})$	G (MPa)	E (MPa)	N_T	N_B	ℓ_T (mm)	ℓ_B (mm)	$\frac{\beta}{\gamma}$
SD Lattices <111> Direction	2.8	4.1	16	0.230	3.9	6.0	1.0	1.0	6.0	8.2	0
SD Lattices <100> Direction	2.2	3.3	16	0.201	4.3	9.6	1	0.23	3.8	7.4	0.3
Triangular Prismatic Lattices - Long Ribs	8.6	18	14	0.093	0.3	2.3	1	0.99	8.9	13.2	0
Triangular Prismatic Lattices - Short Ribs	36	29	8	0.212	1.1	3.1	1	0.99	9.4	8.8	0.5

Chapter 8

Conclusions and Future Work

8.1 Conclusions

This dissertation consisted of a systematic approach to engineering structures demonstrating significant nonclassical phenomenon and explaining and analyzing those phenomena via Cosserat elasticity. Readily available materials, reticulated polyurethane open cell foams, were first studied to probe nonclassical behavior. Nonclassical size effects were experimentally measured and analyzed via Cosserat elasticity. Cosserat elasticity was capable of explaining and predicting the observed behavior which simultaneously demonstrated the applicability and descriptive capability of the Cosserat theory and the limitations of classical elasticity. Notch displacements tests were conducted on the small cell foam to reinforce this point. These foams were both determined to be bend dominated which offered initial insight into required characteristic for achieving Cosserat behavior.

An extra degree of complexity was incorporated as a negative Poisson's ratio in the negative Poisson's ratio reticulated open cell polymer foam. This material supplied a valuable point of comparison for the effects of changing structure on Cosserat properties since it was derived from the large cell foam of the previous study. Triaxially compressing the foam under heat to achieve the re-entrant cellular structure, which caused the negative Poisson's ratio, resulted in a coupling number, N, twice as large as that for the as-received foam. Additionally, the characteristic length of torsion, ℓ_t remained similar between the negative Poisson's ratio foam and the as-received foam

while the characteristic length of bending, ℓ_b was reduced to nearly a third of the value calculated from the as-received foam. This foam was also determined to be bend dominated. Indeed, changing the structure of the as-received foam to this negative Poisson's ratio foam affected the Cosserat constants and produced large size effects which the Cosserat theory of elasticity could explain.

Next, we hypothesized that creating composites using structural elements with unique properties may give rise to unique Cosserat size effects. Specifically, structural elements sensitive to strain gradients in torsion or bending were hypothesized to result in large size effects in that same mode. Segments of corrugated nylon tubing, which were much more rigid in torsion than bending and compression, were built into unidirectional composites with silicone rubber cement. Indeed, incorporating these tubes as structural elements resulted in extremely large size effects in torsion and much more modest size effect in bending, yet still a significant deviation from classical predictions in bending. Since these composites were not cellular structures, the same comparisons of characteristic lengths to average cell size could not be used to determine the deformation mechanism. However, the coupling number, N, was used to determine bend dominated behavior once again.

Materials discussed up to this point had been circular in cross section or approximated as such. This was important because exact solutions for torsion and bending of Cosserat elastic materials with circular cross sections are available but no exact solutions exist for cross sections of other shapes. However, Dr. Lakes and Dr. Drugan developed approximate solutions for the torsion and bending of Cosserat elastic materials with square cross sections. A visiting scholar to the lab, Dr. Dong Li, developed a negative Poisson's ratio tetragonal lattice while visiting. This lattice had a square cross section. Several sizes of this lattice design were created and analyzed as Cosserat continua using the approximate solutions developed by Dr. Lakes and Dr. Drugan. Size effects in torsion and bending of the lattices, consistent with Cosserat elasticity, were measured and the Cosserat elastic constants extracted. The lattices were determined to be bend dominated based upon dependence of the modulus on relative density of the lattice.

A systematic design and experimentation process incorporating concepts learned in previous

studies, detailed in chapter 7, led to the development of transversely isotropic polymer lattices demonstrating large size effects in torsion and bending. These lattices incorporated Sarrus linkage structural elements which decoupled bending and torsion rigidity from rigidity in extension. This maximized sensitivity to the strain gradient in torsion. Bend dominated behavior was found in these lattices, just as in all other materials tested. Therefore, bend dominated behavior was concluded to be a necessary but insufficient characteristic for producing large size effects in cellular materials. This lattice structure, unlike the foams studied previously, provided a path to the attainment of arbitrarily large size effects - the Sarrus linkage rib element can be made more slender as 3D printing technology advances.

8.2 Future Work

The goal of future work is to explore other unique structures as Cosserat elastic materials and probe their behavior, namely size effects. Currently, 3D structures composed of tilting cubes has been analyzed as Cosserat continua via finite element analysis in a companion paper [113]. Experimental analysis in the same capacity as previous studies is being conducted on these specimens. Results will provide an experimental comparison to the analytical results.

Appendix A

Summary of Additive Manufacturing Techniques Used for Lattice Research and Unit Cell Development History

Abstract The additive manufacturing techniques used in the course of research presented in this thesis are introduced and discussed in this appendix. The practical limitations and specifications of these different methods will be detailed in addition to examples of printed unit cells. A synopsis of the unit cell development for each printing method will be provided. Finally, a short summary of the adaptions necessary to achieve a successful unit cell will be given.

A.1 Fused Deposition Modeling (FDM)

FDM printers use a thermoplastic filament, which is heated to its melting point and then extruded, layer by layer, to create a three dimensional object. The objects are printed from the bottom up and this process automatically introduces supports during construction. The supports can be physically removed or dissolved, depending on their material, post printing.

A.1.1 Student Shop FDM

The earliest unit cell prototypes and my first foray into 3-D printing were done through the University of Wisconsin (UW) - Madison student shop. Some of the pertinent specifications for this FDM printer are supplied:

- Build envelope: 8"x8"x12"
- Print resolution 0.007" for high resolution mode and 0.010" for low resolution (res) mode
- Minimum size of a stand alone feature is 0.007" for high res and 0.010" for low res
- Minimum size of a part is 0.014" for high res and 0.020" for low res
- Material used was Stratasys ABSplus P430
- Support material was dissolvable (P400 SR)

Printing History

April 20, 2016 Three different unit cells were printed using the standard (low) resolution mode. One unit cell was printed with cylindrical corrugated tube structural elements (Figure A.1), a second with triangular corrugated tube elements at random orientation (Figure A.2), and a third with triangular corrugated tube elements created with three planes of symmetry (Figure A.3). The lattice parameter of each unit cell was 8mm - all unit cells were cubic.

The printed unit cell quality from the first round of printing was unacceptable due to the unit cell dimensions causing the structural features to approach the resolution of the FDM printer. Non-corrugated rib segments were intended to be hollow, but all of them printed solid. The triangular tubing unit cells were particularly bad - to the point they were not even characterized. However, the cylindrical corrugated tubing unit cell was characterized via Broadband Viscoelastic Spectroscopy (BVS) since it was higher quality than either of the triangular tubing unit cells. The

final moduli for the cylindrical corrugated tubing unit cell were $G = 81$ MPa, $E_b = 217$ MPa, and $E_c = 24$ MPa.

The turnaround time from the student shop was one day for these parts.

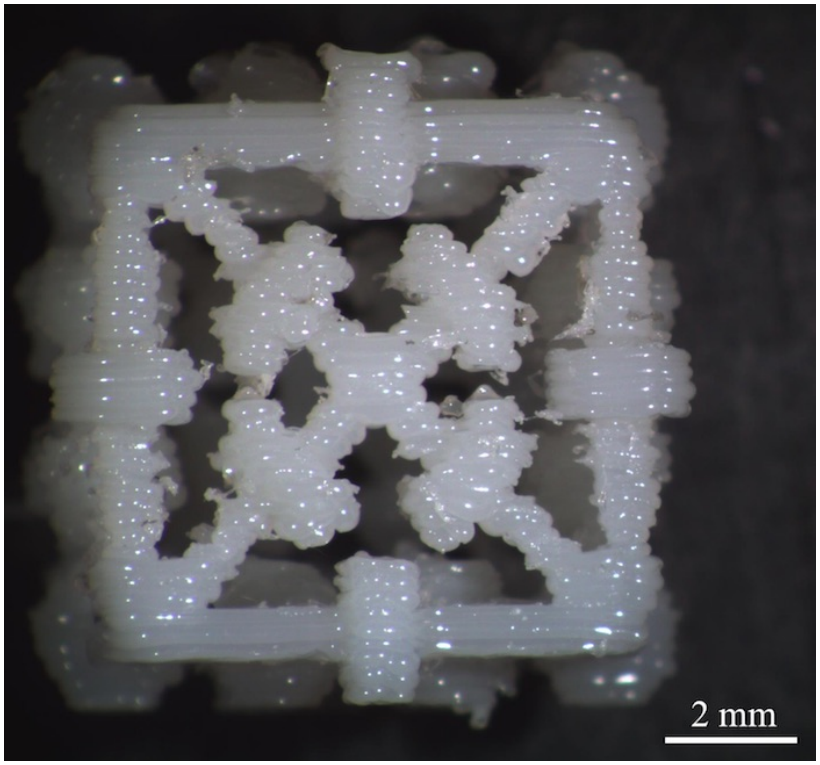

FIGURE A.1: Cylindrical corrugated unit cell created via FDM from April 20, 2016.

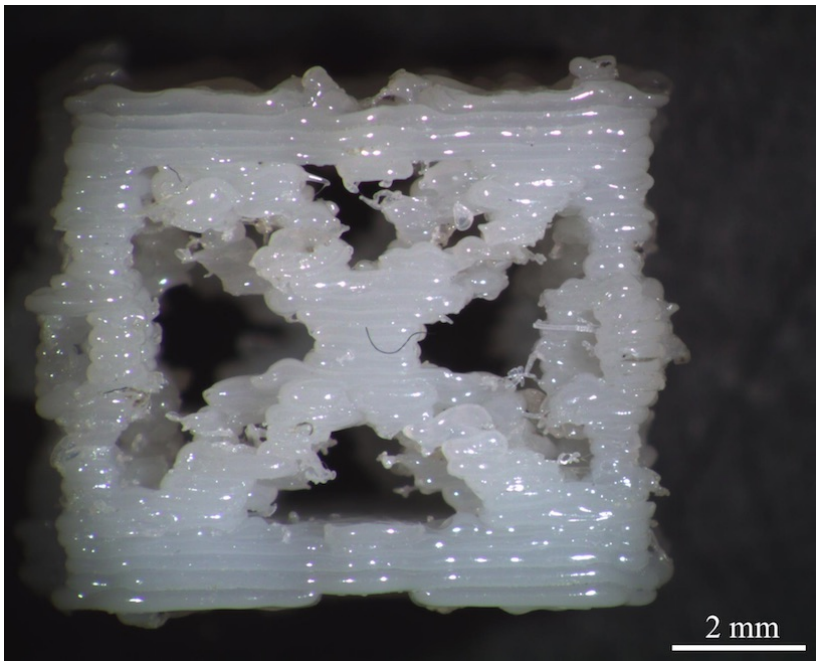

FIGURE A.2: FDM printed unit cell with three fold plate element corrugations and ribs at random rotational positions. April 20, 2016.

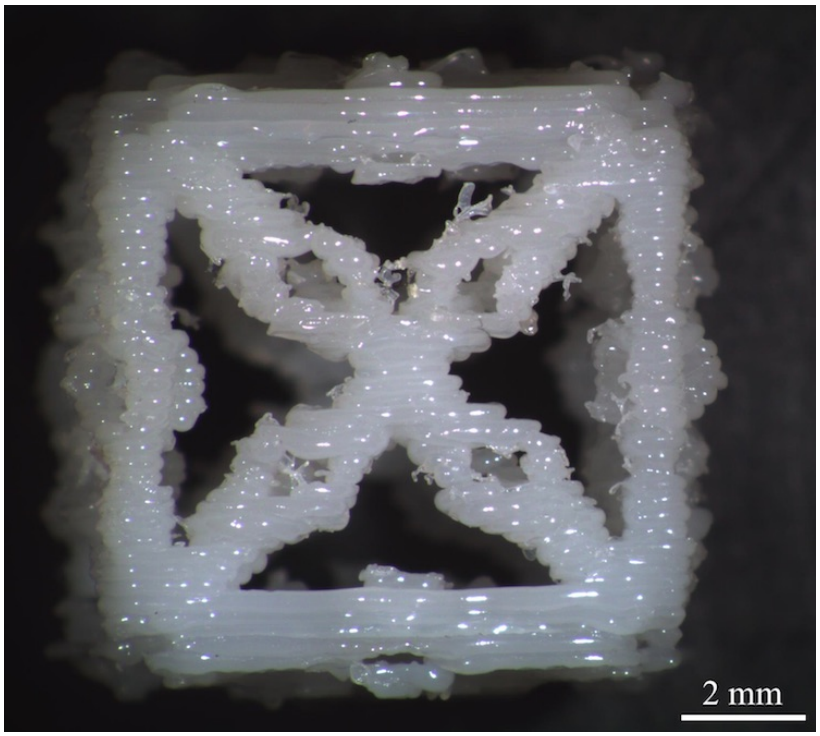

FIGURE A.3: FDM printed unit cell with three fold plate element corrugations. April 20, 2016.

May 10, 2016 The unit cells incorporating cylindrical corrugated tubing and triangular corrugated tubing with three planes of symmetry were reprinted at twice the size, such that they had a new lattice parameter of 16 mm (Figures A.4 and A.5), using the standard resolution. Despite the larger dimensions, the printing method did not achieve the desired rib slenderness for the cylindrical corrugated tubing unit cell - dissection of the ribs disclosed a solid cross section throughout. However, the triangular tubing unit cell showed some promise with obviously open and accessible corrugated segments but solid tubing.

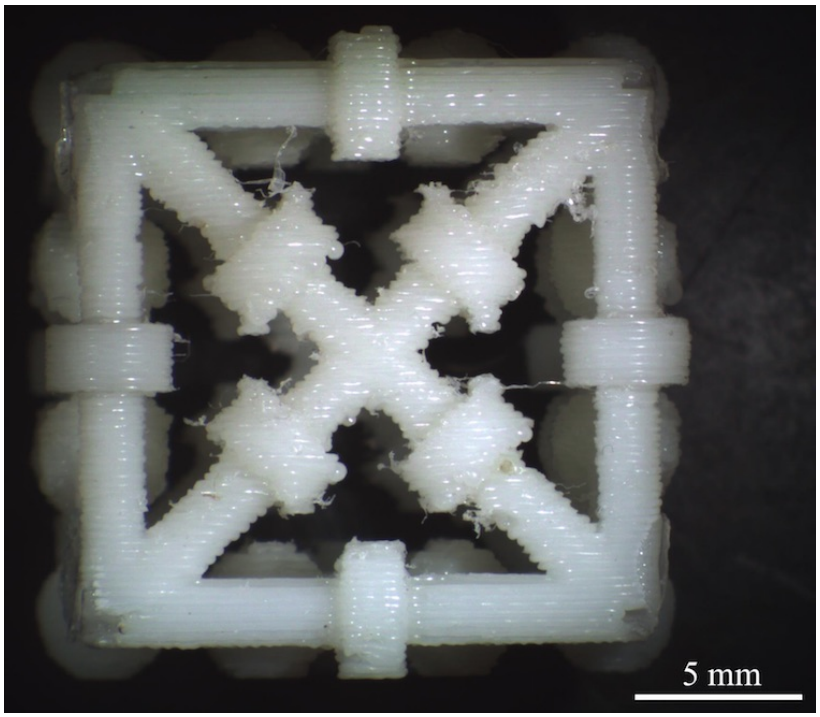

FIGURE A.4: FDM printed unit cell with cylindrical corrugations and ribs. Rib length of 16mm. May 10, 2016.

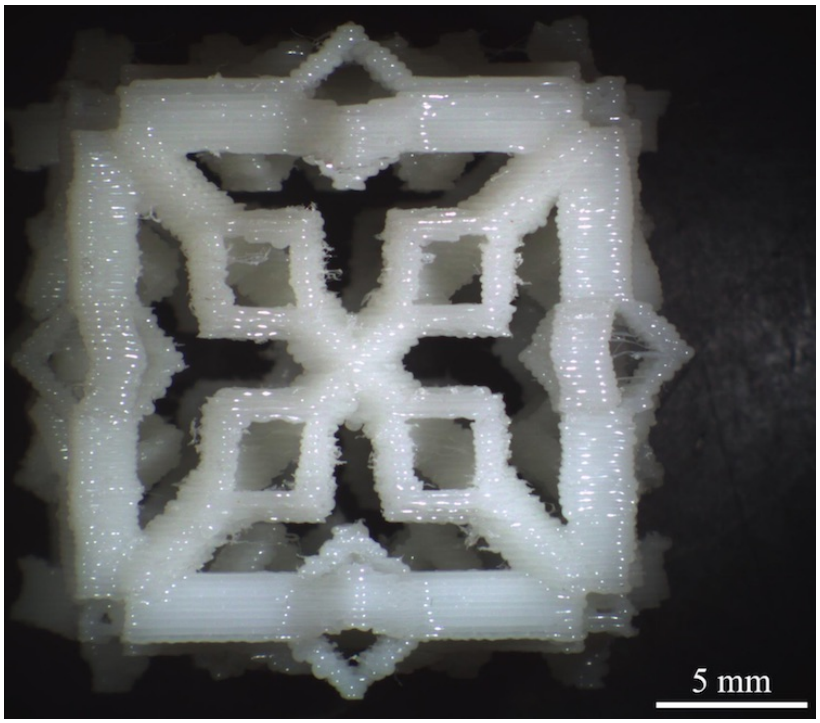

FIGURE A.5: FDM printed unit cell with three fold plate element corrugations. Rib length of 16 mm. May 10, 2016.

The moduli for the cylindrical corrugated unit cell were $G = 123$ MPa and $E_b = 419$ MPa. The moduli for the triangular tubing unit cell were $G = 52$ MPa and $E_b = 229$ MPa. The turnaround time for these parts was same day.

July 13, 2016 The SolidWorks file for the cylindrical corrugated unit cell with the lattice parameter of 16 mm was modified to better accommodate the standard resolution of the printer. All dimensions were kept the same except for wall thickness, adjusted to 0.6 mm, and diameter of the corrugation, which was increased to help achieve desired slenderness. These unit cells were printed using the standard resolution.

Dissection of the finished parts revealed inadequate slenderness. The student shop informed me this could be due to enclosing the space. The support material automatically built into these sections could not be physically removed or dissolved because the construction encapsulates it.

The moduli of these parts were not determined because of their poor slenderness. Turnaround time on these parts was one day.

July 18, 2016 The same file from July 13 was reprinted but this time on high resolution mode. Dissection of the finished parts revealed improved hollowness in the ribs printed in the longitudinal direction but similar hollowness as the previous specimens in the ribs printed in the transverse direction. Regardless of direction, all ribs were insufficiently slender.

Moduli for these parts was not determined due to poor slenderness. Turnaround time for these parts was several days because the lab manager was on vacation.

July 22, 2016 A new unit cell design consisting of ribs with square cross-section tube segments and fourfold plate element corrugation segments was printed. Because slenderness was not achieved using high resolution mode for previous unit cells, this prototype was scaled up significantly such that the rib length for this model was 28 mm. This specimen was printed on high resolution mode. While appreciable slenderness was achieved in this model there were many printing defects. Large square holes centered in the intersection of the ribs composing the top and bottom faces of the unit cell were created during the process. Small triangular shaped holes at each corner on these same faces were also present. These defects are visible in Figure A.6. After discussion with the lab manager, the reason for the existence of these holes lies in the conversion to .STL format which is necessary to print on this FDM printer. The lab manager did not know any way to reconstruct the part to eliminate these holes from the conversion process.

BVS testing of this part was not conducted because of the significant printing defects. Although desired slenderness was achieved, the part quality is unacceptable. Turnaround time on these parts was one day.

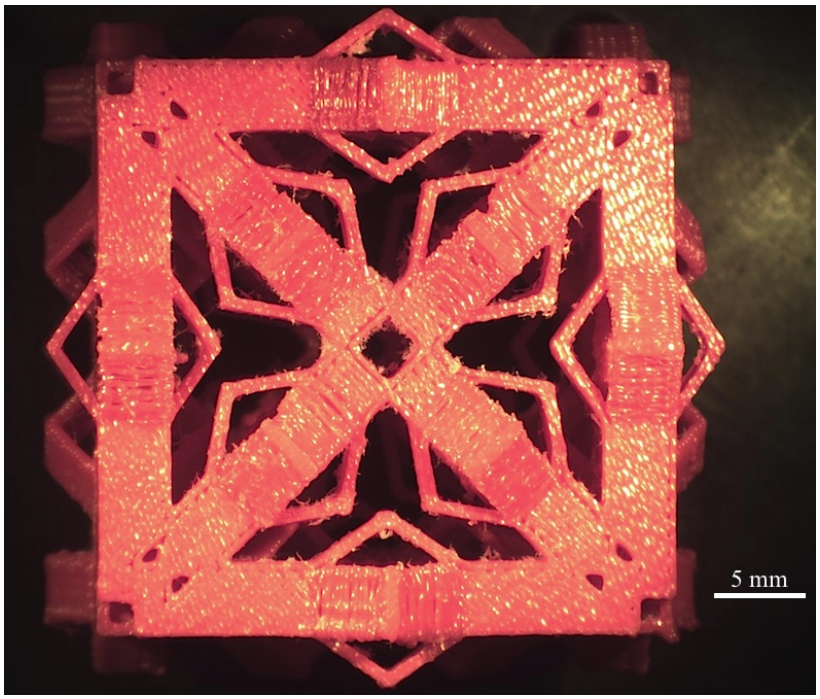

FIGURE A.6: Large FDM printed unit cell with fourfold rib elements and corrugations. July 22, 2016.

A.2 Material Jetting (Polyjet)

Material jetting uses multiple print nozzles jetting one or more liquid photopolymers onto a build tray which are cured with UV light. After curing, another layer may be deposited on top of it. This process is continued until the part is finished. With some of the materials used in this method, the printer automatically builds in supports made from a gel-like material which can be removed by hand or with water.

A.2.1 Midwest Prototyping

The lone specimen printed using this process was completed at Midwest Prototyping (MWP) located in Blue Mounds, WI. The specifications of this printer are:

- Build envelope: 11.57" x 7.55" x 5.85"

- Layer thickness varies between 0.0006" and 0.0011" depending on material
- Resolution for the first inch of printing is 0.002" $+/-$ 0.004" but beyond this the tolerance changes to $+/-$ 0.0015"
- Material used was VeroClear RGD810

Printing History

July 20, 2016 The same triangular symmetric unit cell file used on May 10, 2016 was printed and then finished to finish level one which included removal of supports and light bead blasting. The rib length for this unit cell was 16 mm. The resulting specimen was dimensionally inconsistent as evidenced by Figure A.7. Most of the faces were not square and many of the ribs were warped. This distortion and shrinkage is most likely caused by the curing process according to the printing experts at MWP.

The measured moduli of this specimen were $G = 7$ MPa, $E_b = 7$ MPa and E_c = 4.5 MPa. The turnaround time for this part was six days.

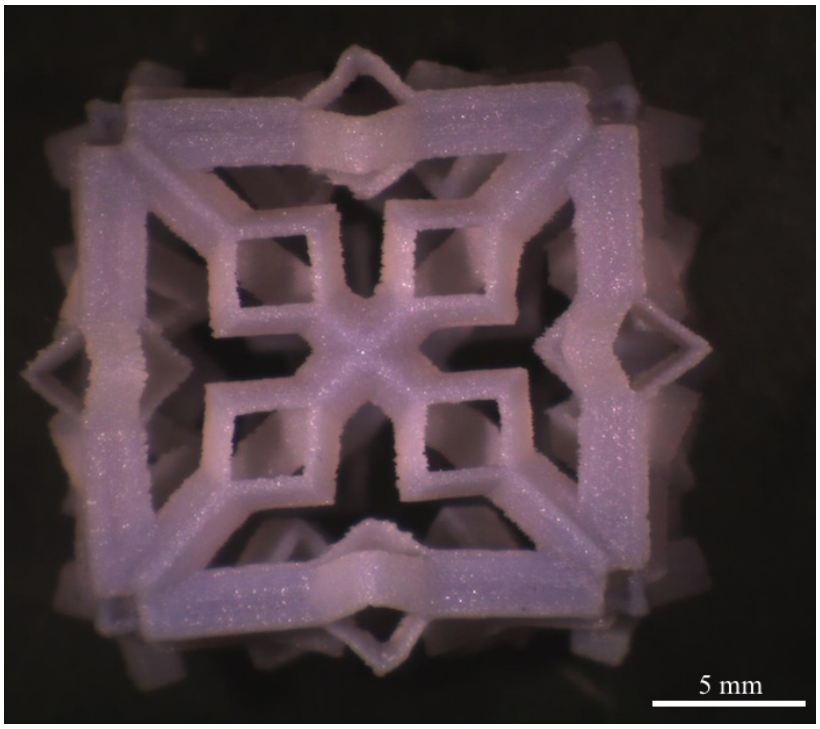

FIGURE A.7: Triangular rib unit celled printed via material jetting. July 20, 2016.

A.3 Selective Laser Sintering (SLS)

This 3 dimensional printing method uses a laser, which automatically aims at points in space according to the part file, to sinter powdered material creating a solid structure. One of the most important characteristics of this method is the absence of supports needed during construction.

A.3.1 Midwest Prototyping

All SLS printing was done at MWP in Blue Mounds, WI. The pertinent specifications of the printer used for all specimens are as follows:

- Build envelope: 28" x 15" x 23"
- Layer thickness = 0.004"

- Laser diameter = 0.01"
- Tolerance for the first inch is $+/-0.005$" and for the second inch is $+/-0.002$"
- Material used was a polyamide simulating nylon 12

Printing History

July 20, 2016 Two files - one for a cylindrical corrugated rib unit cell, (Figure A.8), and one for a plate element triangular rib, (Figure A.9), - were sent to be printed. Both unit cells had 16 mm long ribs. Finish level one was selected which entailed removal of excess powder and light bead blasting. These were by far the highest quality specimens of all printing methods. No dimensional distortion could be observed in either unit cell and desired slenderness was achieved in the plate elements of the triangular ribbed unit cell. The corrugated segments of the cylindrical unit cell held in the raw polyamide material reiterating the difficulties of this design.

Because of the excellent slenderness of the three fold plate elements of the triangular ribbed unit cell, the moduli of the cylindrical corrugated unit cell was not measured. The moduli of the three fold triangular ribbed unit cell were $G = 5$ MPa, $E_b = 16$ MPa and $E_c = 3.1$ MPa. The turnaround time on these parts was six days.

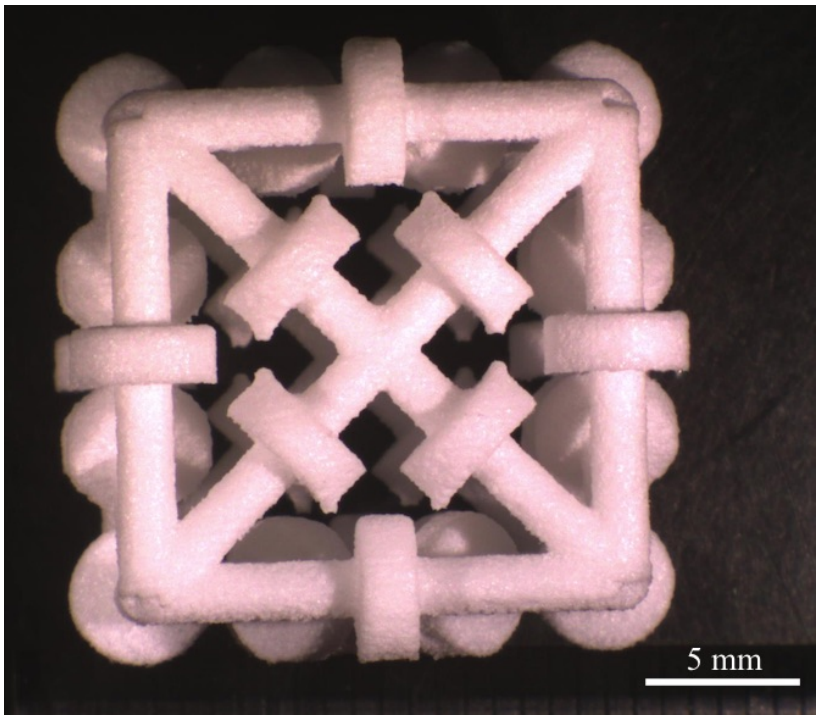

FIGURE A.8: Cylindrical corrugated unit cell printed via SLS on July 20, 2016.

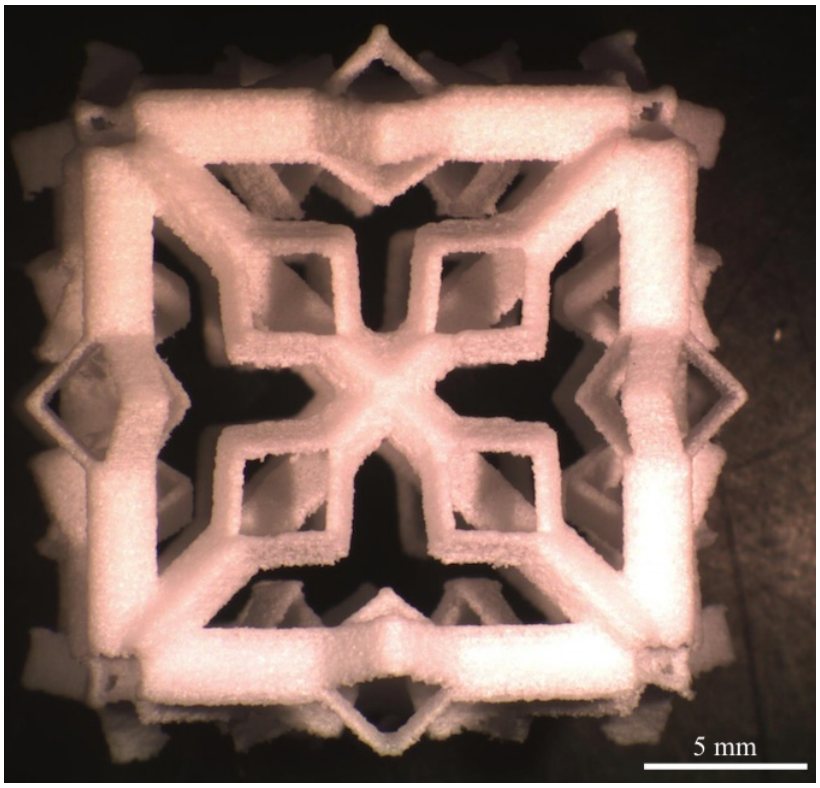

FIGURE A.9: Triangular ribbed unit cell printed via SLS on July 20, 2016.

August 29, 2016 Since the ultimate goal of this project is to build large assemblies of these units cells smaller unit cells had to be developed so that the largest assemblies would fit and could be tested inside of the BVS. Two smaller sizes of unit cells were submitted to MWP for printing, one of which had a rib length of 8 mm, Figure A.10 and the other a rib length of 14 mm Figure A.11. Both of these unit cells were composed of square ribs with fourfold plate element corrugations. Both unit cells were printed from polyamide simulating nylon 12 and finished to finish level 1.

The received specimens had major defects in their structures. The plate elements in the corrugations for both unit cells which were parallel to the bottom and top faces during printing were all incomplete. This was caused by their need to be self supported during the printing process, which they were not because of their orientation. I hypothesized that if the ribs were rotated 45° all the elements would be supported during the printing process and result in a successful part.

Additionally, the unit cell with 8 mm long ribs was not printed with an acceptable resolution. Many of the features, especially the plate elements, were so small they were nearly indistinguishable. This size of unit cell is too small for the practical capabilities of this printer. Other than the aforementioned printing defects the unit cells with 14mm long ribs were of acceptable resolution.

Because of the incomplete corrugation segments these unit cells were not tested for their moduli. The turnaround time on these parts was four days.

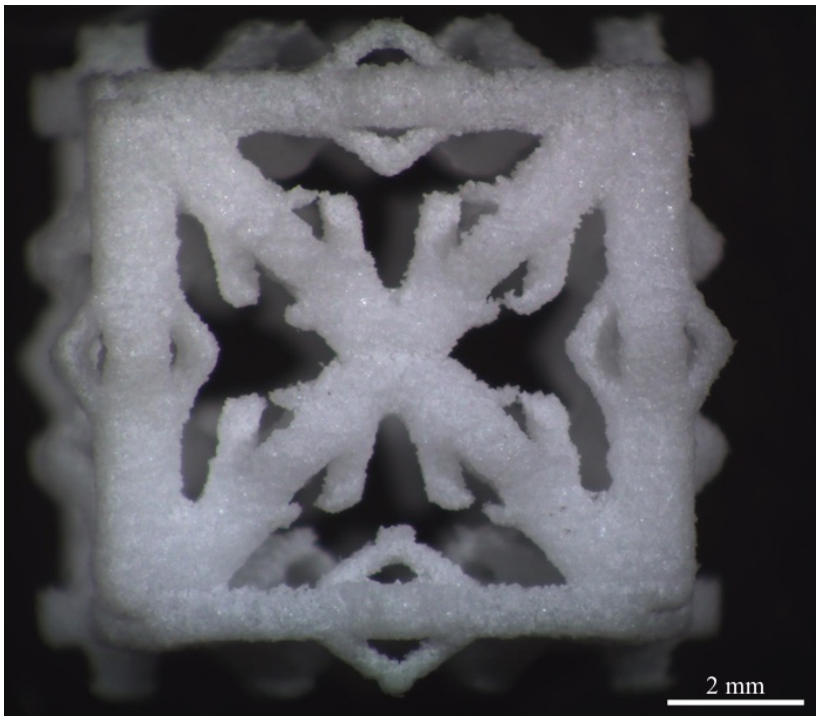

FIGURE A.10: Unit cell with 8mm long ribs characterized by fourfold plate element corrugations. Note incomplete plate elements in the corrugations parallel to top and bottom surfaces. Printed via SLS on August 29, 2016.

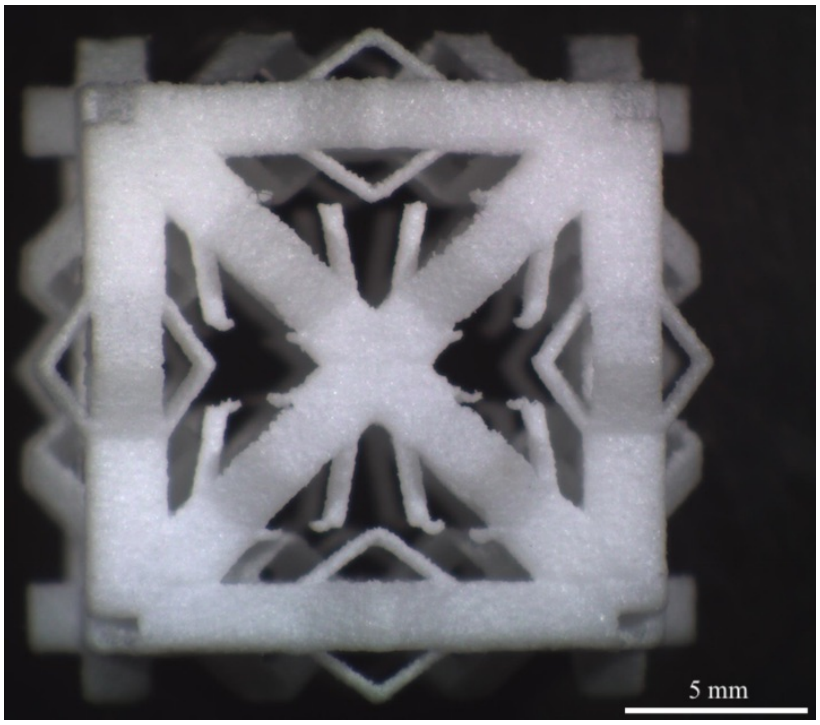

FIGURE A.11: Unit cell with 14mm long ribs characterized by fourfold plate element corrugations. Again, note printing defects on plate elements. Printed via SLS on August 29, 2016.

September 6, 2016 A new unit cell with 14mm long ribs and fourfold plate element corrugations rotated 45° about their longitudinal axes as compared to Figure A.11 was developed and three specimens were printed - one of which is shown in Figure A.12. The specimens were finished to finish level one and were created from polyamide simulating nylon 12. The corrugated segments in these unit cells were all complete. No printing defects could be observed in any of these specimens and adequate slenderness was achieved.

The average moduli of these parts were calculated to be $G = 13$ MPa, $E_b = 39$ MPa and $E_c = 5.6$ MPa. The turnaround time for this order was eight days.

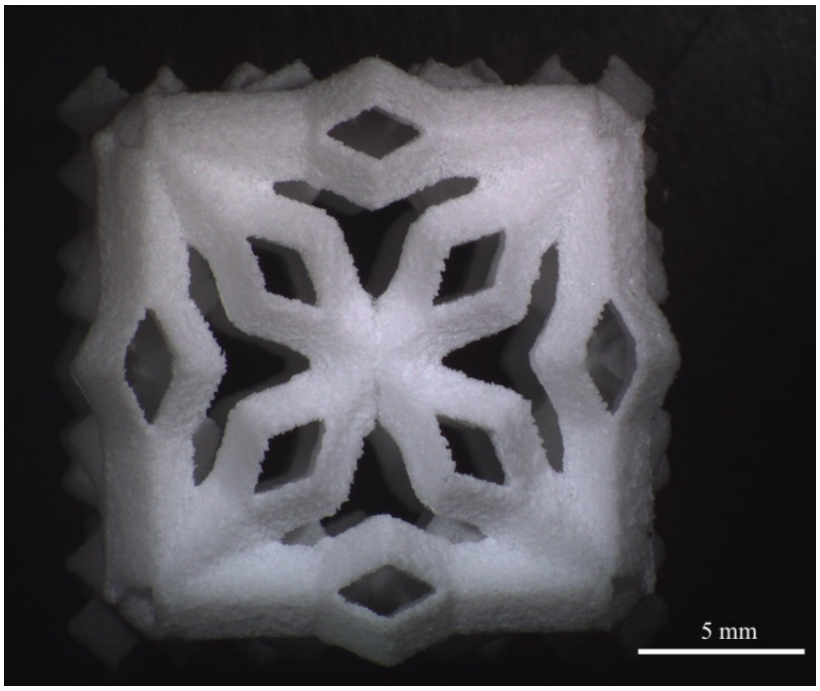

FIGURE A.12: Unit cell with fourfold symmetric ribs rotated 45 degrees from previous specimens. Complete plate elements. Printed via SLS on September 6, 2016.

September 22, 2016 A reiteration of previous unit cells composed of triangular ribs with threefold plate element corrugations, Figure A.9, was created for comparison to results from the previous fourfold square ribbed unit cells Figure A.12. The length of the ribs in this new iteration was 14mm. Again, three specimens were ordered of this unit cell and all were finished to finish level one and made from polyamide simulating nylon 12. The final products were in excellent condition, no printing defects were visible, and desired slenderness was achieved.

The moduli of these three specimens were measured: $G = 16$ MPa, $E_b = 36$ MPa and $E_c = 5.2$ MPa. The turnaround time for this order was six days.

October 14, 2016 A prototype assembly of the unit cells incorporating fourfold symmetric ribs, Figure A.12, was printed by MWP, Figure A.13. This assembly had the unit cells stacked so that their <111> axes were parallel to the longitudinal axis of the specimen. This assembly had many missing plate elements in the corrugations, shown in Figure A.14. After consultation with MWP,

the root cause of these defects was determined to be print orientation of the plate elements. Originally, the ribs were rotated $45°$ so that the plate elements of the corrugations were not parallel to the printing surface. However, when the unit cells were tilted such that their <111> axes were parallel to the longitudinal axis of the specimen, the plate elements again became parallel to the printing surface.

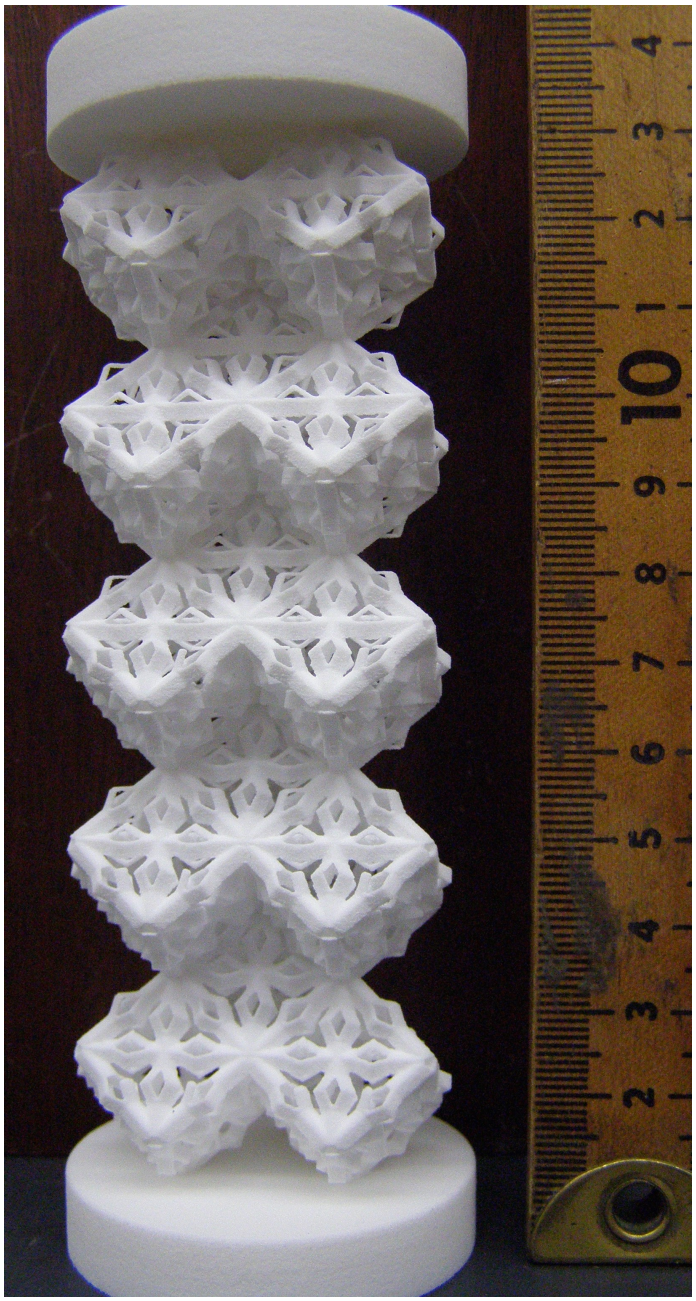

FIGURE A.13: Assembly of the same type of unit cells shown in Figure A.12. Printing defects can be observed in some of the plate elements in the corrugations. Printed October 14, 2016.

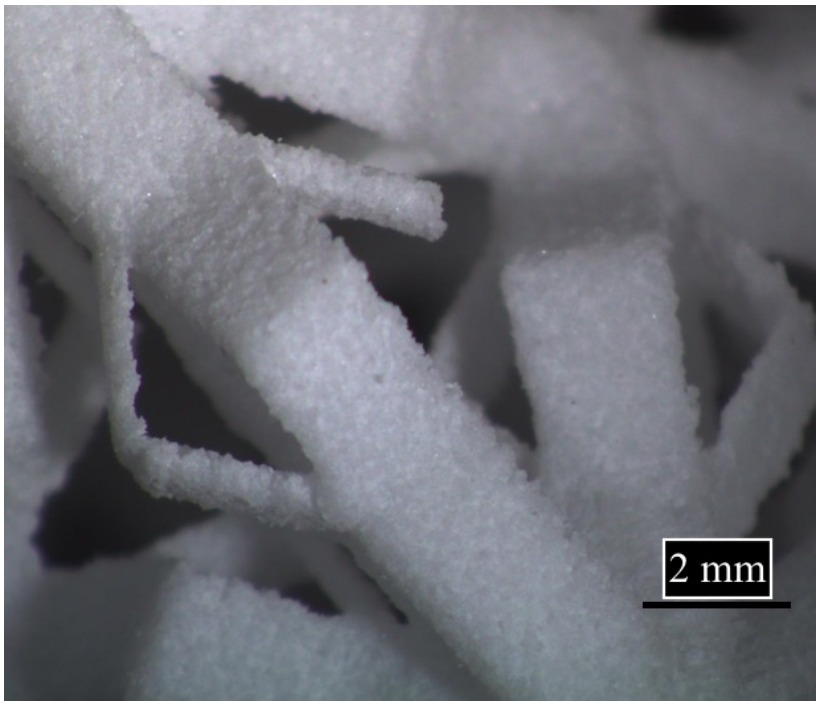

FIGURE A.14: Close up image of printing defects found in the assembly shown in Figure A.13.

The quick solution to this problem was to use the unit cells from Figure A.11 for all assemblies where the unit cells would have their <111> axes parallel to the longitudinal axis of the specimen. For a long term solution, I need to notify MWP prior to printing that the incoming part will have features approaching the minimum resolution of their printers so that the technicians can reorient the part in the software and change the direction it will print.

October 26, 2016 A new assembly of unit cells with their <111> axes parallel to the longitudinal axis of the specimen was created with the unit cells shown in Figure A.11. The resulting assembly is shown below in Figure A.15. This specimen printed error free and the resolution was acceptable. This unit cell will be used for all future assemblies incorporating a face centered cubic unit cell.

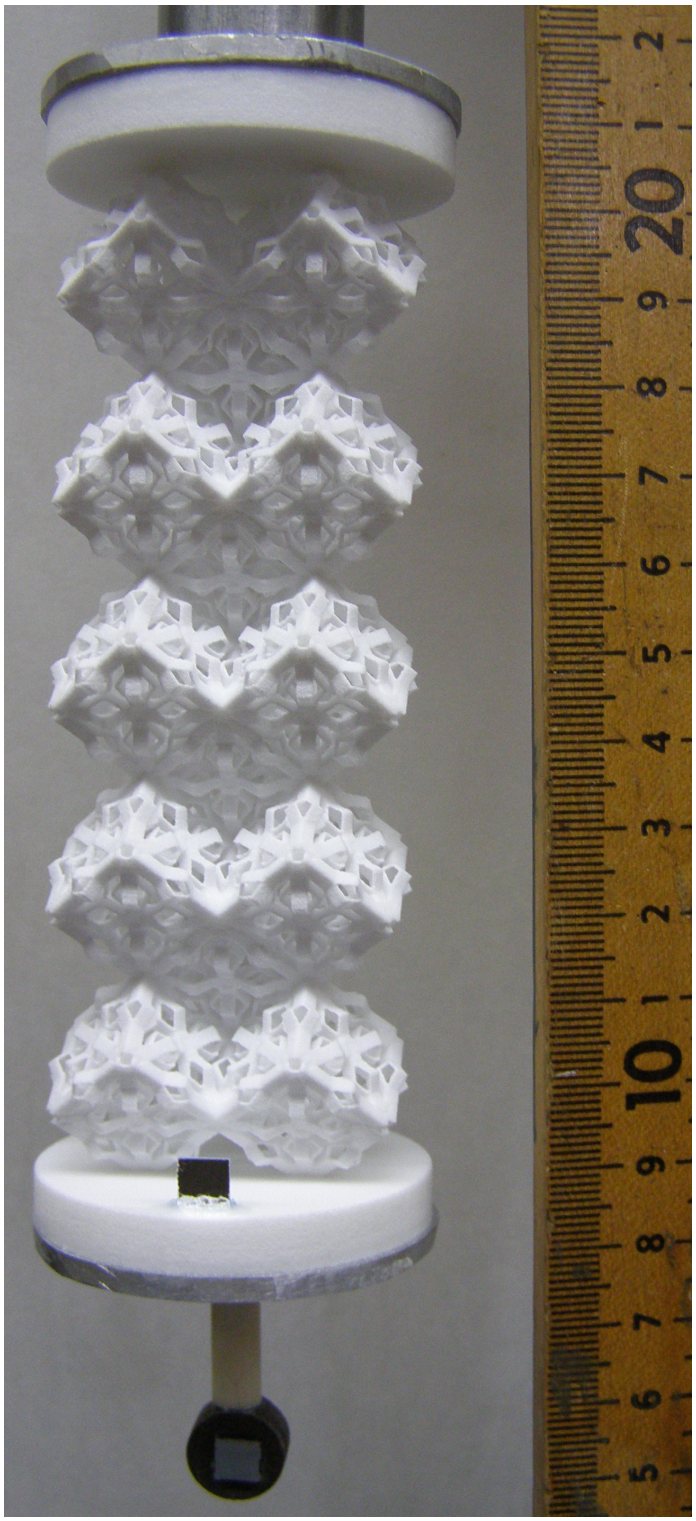

FIGURE A.15: Assembly of unit cells of the same type shown in Figure A.11. No printing defects present. Printed October 26, 2016.

A.4 Summary of Adaptions

The journey to a reliably repeatable and functional unit cell incorporating strain gradient sensitive structural elements began with design and an FDM printer in the student shop on campus. Unit cells incorporating cylindrical corrugations proved too difficult to print. Raw printing mater would get trapped inside the void of the corrugation. A second variation incorporating a three fold open corrugation proved more effective.

Printer resolutions forced crucial dimensional considerations on unit cell design. The student shop FDM printer had poor resolution so unit cells needed to be scaled up considerably, from 8mm long ribs to 16mm. Even still, the slenderness of resulting parts was too poor to achieve desired properties. An additive manufacturing technique with higher resolution was required.

Several different printing methods at MWP were tested including material jetting and SLS. SLS provided the best resolution, repeatedly produced parts with the greatest consistency, and did not require structural supports during the printing process. Cells of different sizes were printed using SLS to determine the smallest unit cell that could be printed while still achieving desired slenderness of corrugations. Unit cells with 14mm ribs achieved desired characteristics of slenderness and structural integrity.

Orientation of the ribs about their longitudinal axes needed to be considered for large 3D lattices. The original three fold corrugated rib did not allow for four fold rotation about its axis, necessary in larger 3D structures. A fourfold corrugated rib was designed for the purpose. Additionally, printing defects occurred at certain print orientations. After consultation with MWP, the best orientation of ribs within the unit cells for consistent printing was such that the sides of each rib were parallel to a face of the unit cells.

Bibliography

[1] S. P. Timoshenko. *History of Strength of Materials, Dover*. NY: Dover, 1983.

[2] L. J. Gibson and M. F. Ashby. *Cellular Solids*. 2nd. Cambridge: Pergamon, 1997.

[3] E. Cosserat and F. Cosserat. *Theorie des Corps Deformables*. Paris: Hermann et Fils, 1909.

[4] W. Voigt. "Theoretische studien über die elasticitätsverhältnisse der krystalle". In: *Königliche Gesellschaft der Wissenschaften zu Göttingen* 34 (1887), pp. 53–100.

[5] R. D. Mindlin and H. F. Tiersten. "Effects of couple-stresses in linear elasticity". In: *Arch. Rat Mech. Anal.* 11.1 (1962), pp. 415–448.

[6] A. C. Eringen and E. S. Suhubi. "Nonlinear theory of simple micro-elastic solids-I". In: *International Journal of Engineering Science* 2 (1964), pp. 189–203.

[7] R. D. Mindlin. "Microstructure in Linear Elasticity". In: *Arch. Rat. Mech. Anal.* 16.1 (1964), pp. 51–78.

[8] A. C. Eringen. "Linear Theory of Micropolar Elasticity". In: *Journal of Mathematics and Mechanics* 15.6 (1966), pp. 909–923.

[9] A. C. Eringen. "Theory of Micropolar Elasticity and Fracture". In: ed. by H. Liebowitz. New York: Academic Press, 1968, pp. 621–729.

[10] S. C. Cowin. "Stress functions for Cosserat elasticity". In: *International Journal of Solids and Structures* 6.4 (1970), pp. 389–398.

[11] S. C. Cowin. "An incorrect inequality in micropolar elasticity theory". In: *Zeitschrift für Angewandte Mathematik und Physik (ZAMP)* 21.3 (1970), pp. 494–497.

[12] W. T. Koiter. “Couple-Stresses in the theory of elasticity Parts I and II”. In: *Proc. Koninklijke NBed. Akad. Wetenshappen* 67 (1964), pp. 17–44.

[13] R. D. Gauthier and W. E. Jahsman. “A Quest for micropolar Elastic Constants”. In: *Journal of Applied Mechanics* 42.2 (1975), pp. 369–374.

[14] G. V. Krishna Reddy and N. K. Venkatasubramanian. “On the flexural rigidity of a micropolar elastic circular cylinder”. In: *Journal of Applied Mechanics* 45 (1978), pp. 429–431.

[15] R. D. Mindlin. “Effect of couple stresses on stress concentrations”. In: *Experimental Mechanics* 3 (1963), pp. 1–7.

[16] B. S. Kim and A. C. Eringen. “Stress distribution around an elliptic hole in an infinite micropolar elastic plate”. In: *Letters in Applied and Engineering Sciences* 1 (1973), pp. 381–390.

[17] R. S. Lakes. “Elastic freedom in cellular solids and composite materials”. In: *Mathematics of Multiscale Materials*. Ed. by K. Golden et al. Springer NY: 99, 1998, pp. 129–153.

[18] E. Kröner. “On the physical reality of torque stresses in continuum mechanics”. In: *Int. J. Engineering. Sci* 1 (1963), pp. 261–278.

[19] J. S. Stolken and A. G. Evnas. “Microbend test method for measuring the plasticity length scale”. In: *J. Acta Mater* 46 (1998), pp. 5109–5115.

[20] M. Zhao et al. “Material-length-scale-controlled nanoindentation size effects due to strain gradient plasticity”. In: *Acta Mater* 51 (2003), pp. 4461–4469.

[21] R. S. Lakes. “On the torsional properties of single osteons”. In: *J. Biomechanics* 28 (1995), pp. 1409–1410.

[22] R. S. Lakes. “Experimental microelasticity of two porous solids”. In: *Int. J. Solids and Structures* 22 (1986), pp. 55–63.

[23] W. B. Anderson and R. S. Lakes. “Size effects due to Cosserat elasticity and surface damage in closed-cell polymethacrylimide foam”. In: *J. Materials Science* 96 (2016), pp. 93–111.

[24] A. C. M. Chong and D. C. C. Lam. “Strain gradient plasticity effect in indentation hardness of polymers”. In: *J. Material. Res* 14 (1999), pp. 4103–4110.

[25] J. Schijve. “Note on couple stresses”. In: *J. Mech. Phys. Solids* 14 (1966), pp. 113–120.

[26] S. Minagawa, K. Arakawa, and M. Yamada. “Diamond crystals as Cosserat continua with constrained rotation”. In: *Physica Status Solidi A* 57 (1980), pp. 713–718.

[27] R. Maranganti and P. Sharma. “Length scales at which classical elasticity breaks down for various materials”. In: *Phys. Rev. Lett* 98 (2007), p. 195504.

[28] M. Rahaeifard et al. “Static pull-in analysis of microcantilevers based on the modified couple stress theory”. In: *Sensors and Actuators* 171 (2011), pp. 370–374.

[29] M. H. Kahrobaiyan, M. Asghari, and M. T. Ahmadian. “Investigation of the size-dependent dynamic characteristics of atomic force microscope microcantilevers based on the modified couple stress theory”. In: *Int. J. of Eng. Sci.* 48 (2010), pp. 1985–1994.

[30] R.D. Mindlin. “Stress functions for a Cosserat continuum”. In: *Int. J. Solids Structures* 1 (1965), pp. 265–271.

[31] L. Ilcewicz, T.C. Kennedy, and C. Shaar. “Experimental application of a generalized continuum model to nondestructive testing”. In: *J. Materials Science Letters* 4 (1985), pp. 434–438.

[32] S.C. Cowin and J.W. Nunziato. “Linear elastic materials with voids”. In: *J. Elasticity* 13 (1983), pp. 125–147.

[33] R. Mora and A.M. Waas. “Measurement of the Cosserat constant of circular cell polycarbonate honeycomb”. In: *Philosophical Magazine A* 80 (2000), pp. 1699–1713.

[34] H.C. Park and R. S. Lakes. “Torsion of a micropolar elastic prism of square cross section”. In: *Int. J. Solids, Structures* 23 (1987), pp. 485–503.

[35] H.C. Park and R.S. Lakes. “Cosserat micromechanics of human bone: strain redistribution by a hydration-sensitive constituent”. In: *J. Biomechanics* 19 (1986), pp. 385–397.

[36] R.S. Lakes, D. Gorman, and W. Bonfield. "Holographic screening method for microelastic solids". In: *J. Materials Science* 20 (1985), pp. 2882–2888.

[37] W.B. Anderson, R.S. Lakes, and M.C. Smith. "Holographic evaluation of warp in the torsion of a bar of cellular solid". In: *Cellular Polymers* 14 (1995), pp. 1–13.

[38] R.D. Nyilas, M. Kobas, and R. Spolenak. "Synchrotron X-ray microdiffraction reveals rotational plastic deformation mechanisms in polycrystalline thin films". In: *Acta Materialia* 57 (2009), pp. 3738–3753.

[39] Foamade Industries. Auburn Hills MI.

[40] M. Brodt, L. S. Cook, and R. S. Lakes. "Apparatus for determining the properties of materials over ten decades of frequency and time: refinements". In: *Rev. Sci. Instrum.* 66 (1995), pp. 5292–5297.

[41] T. Lee, R. S. Lakes, and A. Lal. "Resonant ultrasound spectroscopy for measurement of mechanical damping: comparison with broadband viscoelastic spectroscopy". In: *Rev. Sci. Instrum.* 71 (2000), pp. 2855–2861.

[42] Y. C. Wang, R. S. Lakes, and A. Butenhoff. "Influence of cell size on re-entrant transformation of negative Poisson's ratio reticulated polyurethane foams". In: *Cellular Polymers* 20 (2001), pp. 373–385.

[43] R. Brezny and D.J. Green. "Characterization of edge effects in cellular materials". In: *J. Materials Science* 25.11 (1990), pp. 4571–4578.

[44] C. Tekoglu et al. "Size effects in foams: Experiments and modeling". In: *Progress in Materials Science* 56 (2011), pp. 109–138.

[45] P.M. Buechner and R.S. Lakes. "Size effects in the elasticity and viscoelasticity of bone". In: *Biomechanics and Modeling in Mechanobiology* 1.4 (2003), pp. 295–301.

[46] R.S. Lakes and S. Saha. "Cement line motion in bone". In: *Science* 204 (1979), pp. 501–503.

[47] A. Askar and A. S Cakmak. “A structural model of a micropolar continuum”. In: *Int. J. Engng. Sci* 6 (1968), pp. 583–589.

[48] T. Tauchert. “A lattice theory for representation of thermoelastic composite materials”. In: *Recent Advances in Engineering Science* 5 (1970), pp. 325–345.

[49] G. Adomeit. “Determination of elastic constants of a structured material”. In: *Mechanics of Generalized Continua*. Ed. by E. Kröner. IUTAM Symposium. Freudenstadt, Stuttgart: Springer, Berlin, 1967.

[50] A. Spadoni and M. Ruzzene. “Elasto-static micropolar behavior of a chiral auxetic lattice”. In: *J. Mechs. Physics of Solids* 60 (2012), pp. 156–171.

[51] C.B. Banks and M. Sokolowski. “On certain two-dimensional applications of the couple stress theory”. In: *Int. J. SOlids Struct.* 4.1 (1968), pp. 15–29.

[52] A.J. Wang and D.L. McDowell. “In-plane stiffness and yield strength of periodic metal honeycombs”. In: *J. Eng. Mater. Trans. ASME* 126 (2004), pp. 137–156.

[53] Dos Reis, F. Ganghoffer, and J. F. “Construction of Micropolar Continua from the Homogenization of Repetitive Planar Lattices”. In: *Mechanics of Generalized Continua - Advanced Structured Materials*. Ed. by H. Altenbach, G. Maugin, and V. Erofeev. Vol. 7 Chap. 9. Berlin: Springer, 2011, pp. 193–217.

[54] F. Triawan et al. “The elastic behavior of aluminum alloy foam under uniaxial loading and bending conditions”. In: *J. Acta Materialia* 60 (2012), pp. 3084–3093.

[55] R. S. Lakes and W. J. Drugan. “Bending of a Cosserat elastic bar of square cross section - theory and experiment”. In: *J. Applied Mechanics* 82.9 (2015), p. 091002.

[56] A. C. Eringen. “Theory of thermo-microstretch elastic solids”. In: *Int. J. Eng. Sci.* 28.12 (1990), pp. 1291–1301.

[57] A. Burteau et al. “Impact of material processing and deformation on cell morphology and mechanical behavior of polyurethane and nickel foams”. In: *International Journal of Solids and Structures* 49 (2012), pp. 2714–2732.

[58] T. Dillard, S. Forest, and P. Ienny. “Micromorphic continuum modelling of the deformation and fracture behaviour of nickel foams”. In: *European Journal of Mechanics (A) Solids* 25 (2006), pp. 526–549.

[59] C.P. Chen and R.S. Lakes. “Dynamic wave dispersion and loss properties of conventional and negative Poisson’s ratio polymeric cellular materials”. In: *Cellular Polymers* 8.5 (1989), pp. 343–359.

[60] R. F. Almgren. “An isotropic three dimensional structure with Poisson’s ratio = - 1”. In: *Journal of Elasticity* 15.4 (1985), pp. 427–30.

[61] R. S. Lakes. “Foam structures with a negative Poisson’s ratio”. In: *Science* 235 (1987), pp. 1038–1040.

[62] E. A. Friis, R. S. Lakes, and J. B. Park. “Negative Poisson’s ratio polymeric and metallic materials”. In: *Journal of Materials Science* 23 (1988), pp. 4406–4414.

[63] K. W. Wojciechowski. “Constant thermodynamic tension Monte Carlo studies of elastic properties of a two-dimensional systems of hard cyclic hexamers”. In: *Molecular Physics* 61 (1987), pp. 1247–125.

[64] K. W. Wojciechowski. “Two-dimensional isotropic system with a negative Poisson ratio”. In: *Physics Letters A* 137 (1989), pp. 60–64.

[65] G. Milton. “Composite materials with Poisson’s ratios close to -1”. In: *J. Mech. Phys. Solids* 40 (1992), pp. 1105–1137.

[66] K. E. Evans, M. A. Nkansah, and I. J. Hutchinson. “Auxetic foams - modeling negative Poisson’s ratios”. In: *Acta. Metall. Mater.* 42.4 (1994), pp. 1289–1294.

[67] J. N. Grima, A. Alderson, and K. E. Evans. “Auxetic behaviour from rotating rigid units”. In: *Physica Status Solidi B* 242 (2005), pp. 561–75.

[68] C. P. Chen and R. S. Lakes. “Holographic study of conventional and negative Poisson’s ratio metallic foams: elasticity, yield, and micro-deformation”. In: *J. Materials Science* 26 (1991), pp. 5397–5402.

[69] R. S. Lakes. “Experimental micro mechanics methods for conventional and negative Poisson’s ratio cellular solids as Cosserat continua”. In: *J. Engineering Materials and Technology* 113 (1991), pp. 148–155.

[70] L. J. Gibson et al. “The mechanics of two dimensional cellular solids”. In: *Proc. Royal Society A*. 1982, pp. 25–42.

[71] L. Brillouin. *Wave Propagation in Periodic Structures*. N.Y: Dover, 1953.

[72] R. S. Lakes. “Experimental methods for study of Cosserat elastic solids and other generalized continua”. In: *Continuum models for materials with micro-structure*. Ed. by H. Muhlhaus and J. Wiley. N. Y.: Wiley, 1995, pp. 1–22.

[73] Z. Rueger and R. S. Lakes. “Experimental Cosserat elasticity in open cell polymer foam”. In: *Philosophical Magazine* 96.2 (2016), pp. 93–111.

[74] J. B. Choi and R. S. Lakes. “Nonlinear properties of polymer cellular materials with a negative Poisson’s ratio,” in: *J. Materials Science* 27 (1992), pp. 4678–4684.

[75] D. Li, L. Dong, and R. S. Lakes. “The properties of copper foams with negative Poisson’s ratio via resonant ultrasound spectroscopy”. In: *Physica Status Solidi* 250.10 (2013), pp. 1983–1987.

[76] M. Bianchi, F. L. Scarpa, and C. W. Smith. “Stiffness and energy dissipation in polyurethane auxetic foams”. In: *Journal of Materials Science* 43.17 (2008), pp. 5851–5860.

[77] J. N. Grima et al. “A Novel Process for the Manufacture of Auxetic Foams and for Their re-Conversion to Conventional Form”. In: *Advanced Engineering Materials* 11 (2009), pp. 533–535.

[78] A. A. Pozniak, J. Smardzewski, and K. W. Wojciechowski. “Computer simulations of auxetic foams in two dimensions”. In: *Smart Materials and Structures* 22.8 (2013). 084009, 11pp.

[79] R. S. Lakes. “Physical meaning of elastic constants in Cosserat, void, and microstretch elasticity”. In: *Journal of Mechanics of Materials and Structures* 11 (2016), pp. 217–229.

[80] Z. Rueger and R. S. Lakes. “Cosserat elasticity of negative Poisson’s ratio foam: experiment”. In: *Smart Materials and Structures, accepted* 25.054004 (2016), 8pp.

[81] Waytek Incorporated. In: *Chanhassen MN* ().

[82] S.G. Lekhnitskii. *Theory of elasticity of an anisotropic body*. Mir Moscow, 1981.

[83] S. Burns. “Negative Poisson’s ratio materials, letter”. In: *Science* 238 (1987), p. 551.

[84] R. S. Lakes. “Negative Poisson’s ratio materials, response”. In: *Science* 238 (1987), p. 551.

[85] S. Hirotsu. “Elastic anomaly near the critical point of volume phase transition in polymer gels”. In: *Macromolecules* 23 (1990), pp. 903–905.

[86] R. E. McKnight et al. “Grain size dependence of elastic anomalies accompanying the alpha-beta phase transition in polycrystalline quartz”. In: *J. Phys. Cond. Mat* 20 (2008), p. 075229.

[87] K. V. Tretiakov and K. W. Wojciechowski. “Orientational transition between isotropic crystalline phases in planar systems of hard cyclic pentamers and heptamers”. In: *Journal of Physics: Condensed Matter* 14 (2002), p. 1261.

[88] K. V. Tretiakov and K. W. Wojciechowski. “Monte Carlo simulation of two-dimensional hard body systems with extreme values of the Poisson’s ratio”. In: *Physica Status Solidi B* 242 (2005), pp. 730–741.

[89] D. Li et al. “Three-dimensional stiff cellular structures with negative Poisson’s ratio”. In: *Physica Status Solidi B* (2017).

[90] W. J. Drugan and R. S. Lakes. "Torsion of a Cosserat elastic bar of square cross section: theory and experiment". In: *Z. Angew. Math. Phys.* 69.24 (2018). URL: https://doi.org/10.1007/s00033-018-0913-1.

[91] R. Brezny and D. J. Green. "Characterization of edge effects in cellular materials". In: *J Materials Sci* 25 (1990), pp. 4571–4578.

[92] R. Gatt et al. "On the properties of real finite-sized planar and tubular stent-like auxetic structures". In: *Phys Status Solidi B* 251 (2014), pp. 321–327.

[93] L. La Ragione and J. T. Jenkins. "The influence of particle fluctuations on the average rotation in an idealized granular material". In: *Journal of the Mechanics and Physics of Solids* 57.9 (2009), pp. 1449–1458.

[94] N. Mitarai, H. Hayakawa, and H. Nakanishi. "Collisional Granular Flow as a Micropolar Fluid". In: *Phys. Rev. Lett.* 88 (2002), p. 174301.

[95] K. W. Wojciechowski, P. Pierarlski, and J. Malecki. "A hard-disk system in a narrow box. I. Thermodynamic properties". In: *J. Chem. Phys.* 76 (1982), pp. 6170–6175.

[96] K. W. Wojciechowski et al. "Elastic properties of two-dimensional hard disks in the close-packing limit". In: *J. Chem. Phys.* 119 (2003), pp. 939–946.

[97] M. Warner et al. "Untwisting of a Cholesteric Elastomer by a Mechanical Field". In: *Phys. Rev. Lett.* 102 (2009), p. 217601.

[98] E. V. Bursian and O. I. Zaikovskii. "Changes in the curvature of a ferroelectric film due to polarization". In: *Sov. Physics Solid State* 10.5 (1968), pp. 1121–1124.

[99] E. V. Bursian and N. N. Trunov. "Nonlocal piezoelectric effect". In: *Sov. Physics Solid State* 16.4 (1974), pp. 760–762.

[100] I. Naumov, A. M. Bratkovsky, and V. Ranjan. "Unusual Flexoelectric Effect in Two-Dimensional Noncentrosymmetric sp^2-Bonded Crystals". In: *Phys. Rev. Lett.* 102 (2009), p. 217601.

[101] D. Bigoni and W. J. Drugan. “Analytical derivation of Cosserat moduli via homogenization of heterogeneous elastic materials”. In: *J. Appl. Mech.* 74 (2007), pp. 741–753.

[102] A. Merkel and V. Tournat. “Experimental Evidence of Rotational Elastic Waves in Granular Phononic Crystals”. In: *Phys. Rev. Lett.* 107.22 (2011), p. 225502.

[103] R. S. Lakes. “Materials with structural hierarchy”. In: *Nature* 361 (1993), pp. 511–515.

[104] D. Rayneau-Kirkhope, Y. Mao, and R. Farr. “Ultralight Fractal Structures from Hollow Tubes”. In: *Phys. Rev. Lett.* 109 (2012), p. 204301.

[105] C. Kern, M. Kadic, and M. Wegener. “Experimental Evidence for Sign Reversal of the Hall Coefficient in Three-Dimensional Metamaterials”. In: *Phys. Rev. Lett.* 118 (2012), p. 016601.

[106] A. C. Eringen. *Microcontinuum field theories , I*. New York: Springer, 1998.

[107] Z. Rueger and R. S. Lakes. “Experimental Cosserat elasticity in open-cell polymer foam”. In: *Philosophical Magazine* 96.2 (2016), pp. 93–111.

[108] Z. Rueger and R. S. Lakes. “Observation of Cosserat Elastic Effects in a Tetragonal Negative Poisson’s Ratio Lattice”. In: *physica status solidi (b)* 254.12 (2017), p. 1600840.

[109] T. Park, W.S. Hwang, and J.W. Hu. “Plastic continuum models for truss lattice materials with cubic symmetry”. In: *Journal of Mechanical Science and Technology* 24.3 (2009), pp. 657–669.

[110] R. Fearing. “Sarrus Linkage”. In: *Rapid Prototyping of Millirobots Using Composite Fiber Toolkits* (). DOI: 4/19/2018. URL: https://people.eecs.berkeley.edu/~ronf/DESKTOP/prototyping/linkages.html.

[111] Z. Rueger and R. S. Lakes. “Strong Cosserat elasticity in a transversely isotropic polymer lattice”. In: *Phys. Rev. Lett.* 120 (2018), p. 065501.

[112] Z. Rueger and R. S. Lakes. “Strong Cosserat elastic effects in a unidirectional composite”. In: *Z. Angew. Math. Phys.* 68.54 (2017). URL: https://doi.org/10.1007/s00033-017-0796-6.

[113] C. Andrade, C. Ha, and R.S. Lakes. “Extreme Cosserat elastic cube structure with large magnitude of negative Poisson’s ratio”. In: *J. Mech. of Mater. and Struc.* 13.1 (2018). URL: 10.2140/jomms.2018.13.93.